COMPUTATIONAL HIGH THROUGHPUT SEARCHES FOR EFFICIENT CATALYSTS

by

Karthikeyan Saravanan

Bachelors of Technology in Chemical and Electrochemical Engineering, Central Electro Chemical Research Institute - India, 2013

Submitted to the Graduate Faculty of
the Swanson School of Engineering in partial fulfillment
of the requirements for the degree of

Doctor of Philosophy

University of Pittsburgh

2018

UNIVERSITY OF PITTSBURGH

SWANSON SCHOOL OF ENGINEERING

This dissertation was presented

by

Karthikeyan Saravanan

It was defended on

November 19, 2018

and approved by

Prof. John A. Keith, Ph.D., Assistant Professor,

Department of Chemical and Petroleum Engineering

Prof. James R. McKone, Ph.D., Assistant Professor,

Department of Chemical and Petroleum Engineering

Prof. Guofeng Wang, Ph.D., Associate Professor,

Department of Mechanical Engineering

Prof. Wissam Saidi, Ph.D., Associate Professor,

Department of Mechanical Engineering

Prof. Geoffrey R. Hutchison, Ph.D., Associate Professor,

Department of Chemistry

Dissertation Director: Prof. John A. Keith, Ph.D., Assistant Professor,

Department of Chemical and Petroleum Engineering

COMPUTATIONAL HIGH THROUGHPUT SEARCHES FOR EFFICIENT CATALYSTS

Karthikeyan Saravanan, PhD

University of Pittsburgh, 2018

Several screening studies identifying new catalysts for different reactions have been reported over the past decade. Almost all of them employ Kohn-Sham density functional theory (KS-DFT) and thermodynamic descriptors to screen for new catalysts. Though usually considered reliable for descriptor-based analyses, KS-DFT calculations are computationally expensive and intractable for use when screening across the full chemical space of all possible alloy materials. In order to accelerate screening of catalysts, we employ a perturbation theory model, "Computational Alchemy" to approximate KS-DFT energies at a fraction of the computational cost. In this thesis, we discuss about how computational alchemy and machine learning can be used to reliably screen for efficient catalysts for a wide range of electrochemical processes based on thermodynamic activity descriptors.

As a first step, we assess the promise of computational alchemy in predicting binding energies thousands of times faster than DFT. We identify distinct cases where alchemy performs significantly worse, indicating areas where modeling improvements are needed. We find that alchemical estimates yield binding energies within 0.1 eV of DFT values for a wide range of adsorbates. Largest errors (≈ 0.4 eV) were observed when Alchemy predicted BEs of the adsorbates on alloys that were obtained by changing large number of atoms and to a large change in nuclear charge. Using a Machine learning approach, the errors between Alchemy and DFT were corrected. Our results suggest that computational alchemy with machine learning is a very promising tool that warrants further consideration for high-throughput screening of heterogeneous catalysts.

TABLE OF CONTENTS

LIST OF TABLES

LIST OF FIGURES

PREFACE

First of all, I would like to thank my advisor Dr. John A. Keith, who has been an important part of my life. He trusted my background from my undergraduate and hired me into his research group as one of his first graduate students. He has been really supportive ever since and has given me the freedom to pursue various projects without objection.

I would also like to thank Prof. Anatole von Lilienfeld for collaborating with us on Alchemy. Anatole and his students helped me understand Alchemy and Machine learning when I spent a month at their research group in Basel. I am also very grateful to Dr. John Kitchin and Dr. Zachary Ulissi for their scientific advice, knowledge and many insightful discussions and suggestions.

I would like to thank my committee members Dr. Guofeng Wang, Dr. Wissam Saidi, Dr. James McKone and Dr. Geoff Hutchison for their time and useful suggestions in shaping up my PhD research.

I would like to acknowledge all current and past members in the Keith group, Mitchell Groenenboom, Minh Nguyen Vo, Yasemin Basdogan, Charles D. Greigo for all the fun conversations and group lunches we had over the years. I would like to specially thank Dr. Aude Marjolin for her help and teaching while she was a postdoc in the Keith group. She helped us get started in the group by showing us how to run computational chemistry calculations on Pitt's computers. I am really grateful to Dr. Victor Oyeyemi who was a major influence in my life leading me to career in data science and machine learning. I can't thank Victor enough for all his help with providing resume feedbacks and interview preparation for my first data science internship.

I will forever be thankful to my former undergraduate research advisor, Dr. Palanichamy Murugan without whom I would not have pursued graduate school. My computational chemistry research journey started from his lab where I first started running VASP calculations on cadmium chalcogenides. I still think fondly of my time as an undergraduate student in his lab. The experience that I gained in his lab from using linux, interacting with job submission systems and VASP helped me get a head-start at Pitt.

I would like to acknowledge funding from the graduate research fellowship at Pittsburgh Quantum Institute and ACS PRF for funding my PhD. I thank Center for Research Computing (CRC now, SAM then) and everyone from CRC (Dr. Albert Defusco, Dr. Kim Wong and Dr. Barry Moore) for all the support they provided with running jobs on Pitt's supercomputers.

Finally, I would like to thank my better half Pavithra who has been a tremendous source of support and motivation. Our 4 month old daughter Neha needs a special mention here as she has been really supportive by sleeping well through the nights and letting me finish my thesis. This preface would be incomplete without thanking my family, mom, dad, my brother who have sacrificed a lot to get me here.

1.0 ELECTROCHEMICAL CO_2 REDUCTION

1.1 ABSTRACT

Electrochemical conversion of CO_2 into usable hydrocarbons takes place via multiple proton and electron transfer steps. Experiments from a variety of different research groups have shown a wide range of compounds from organic molecules to metal oxides that are suitable for catalyzing electrochemical reduction of CO_2. We report that many of these results can be rationalized using thermodynamic descriptors from quantum chemical calculations that identify the electrochemical conditions at which catalysts participate in energetically efficient proton and electron transfers. Our studies have shown thermodynamic Pourbaix diagrams to be robust and useful tools to identify relevant intermediates in homogeneous and heterogeneous CO_2 reduction and understand how these catalysts facilitate energetically efficient catalysis.

1.2 INTRODUCTION

Society's continued consumption of fossil fuels results in increasing levels of CO_2 in the atmosphere, and the concentration of CO_2 in Antarctica recently passed 400 ppm, a level that has not been reached for four million years. Since CO_2 is correlated with extreme weather and global climate change, there have been efforts toward developing sources for renewable and sustainable energy that would supplant fossil fuels. In particular, there is great interest in converting CO_2 into value-added chemicals and fuels such as formic acid, CO, or methanol.[1, 2]

Progress has been made in CO_2 reductions to useful products based on chemical,[3] thermal,[4] electrochemical,[5, 6, 7, 8], or photochemical means,[9, 10] or via combinations of different approaches.[11, 12, 13] Electrochemical and photochemical processes operating at room temperature show promise for scalability and favorable energetic efficiency, but it remains challenging to design electro- and photocatalysts with low overpotentials and high faradaic efficiencies for proton and electron transfers.[14, 15] Improved guidelines would be helpful for understanding how to effectively and selectively control proton and electron transfers within generalized proton coupled electron transfer (PCET) reactions.[16, 17, 18]

1.3 CHALLENGES WITH CO_2 REDUCTION

CO_2 reduction to fuels is a multi-step process that takes place by proton coupled electron transfers. The reduction of CO_2 to liquid fuels precursors (CO + H_2, synthesis gas) or directly to liquid fuels (such as methanol or methane) is thermodynamically feasible with these reactions becoming increasingly favorable with an increasing number of proton-coupled electrons transferred. The thermodynamic potentials for relevant reduction products are shown in Figure 1.1. In order to obtain methanol and methane, $6H^+/6e^-$ and $8H^+/8e^-$ is required to transfer to CO_2. The other problem in CO_2 reduction is the selectivity and overpotentials. The energy of adding just an electron to CO_2 in order to reduce it is too high as seen by the more negative potential shown here. But, adding protons and electrons simultaneously lowers the potentials at which CO_2 reduction can be effected. However, the potentials of different reduction reactions lie close to each other, making it harder to obtain any of the products selectively. Also, CO_2 reduction is further made difficult by the hydrogen evolution reaction whose potential lies close to other CO_2 reduction reactions as well.

Since performing these reactions near their thermodynamic potentials is challenging, we are in need for versatile catalysts. By the use of catalysts, the energy barriers of CO_2 activation can be minimized and subsequent proton and electron transfers can be facilitated. An ideal catalyst would be one which selectively forms methanol or other products with C-C bonds, which is both photo and electro active, and which is an efficient proton and electron

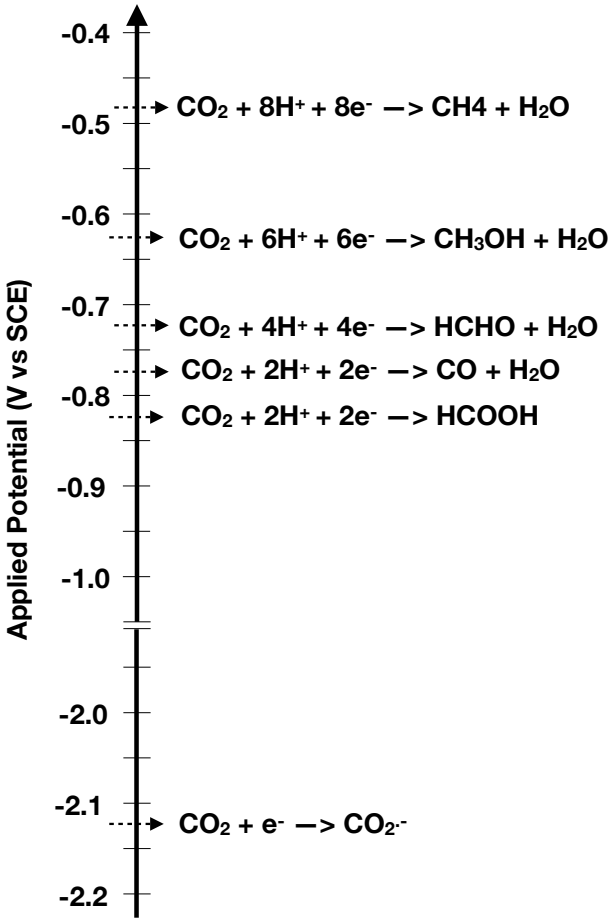

Figure 1.1: Thermodynamic potentials of converting CO_2 into various products (V vs SCE)

transfer agent. Though there have been different catalytic systems that reduce CO_2 into fuels, aromatic nitrogen heterocycles have been shown to be promising candidates for CO_2 reduction. Pyridine, ionic liquids and other nitrogen heterocycles reduce CO_2 at low over potentials with high faradaic efficiency. However, they require a surface for the process and the role of surface in these systems have been widely discussed.

1.4 THERMODYNAMIC DESCRIPTORS FOR MODELING CO_2 REDUCTION

Our approach to identifying energetically efficient catalysts for CO_2 reduction is modeling proton coupled electron transfers using first-principles quantum chemistry. This usually involves calculating different electrochemical reactivities of the catalyst molecules taking part in CO_2 reduction using DFT. The reactivites are based on the fundamental thermodynamic energies of the proton and electron transfer to the catalyst and they serve as thermodynamic descriptors of identifying promising catalysts. Thermodynamically consistent Hesss cycles shown in Figure 1.2 were used to calculate the following descriptors: pK_a, redox potentials and hydricities. A pK_a denotes the thermodynamic free energies of shuttling protons by a catalyst, redox potential describes the thermodynamic potential to add or remove electrons from a catalyst and a hydricity refers to the ability of a catalyst to efficiently shuttle hydrides ($1H^+/2e^-$ product). More details about our calculation methodology are discussed in Chapter 3.

1.4.1 Pourbaix diagrams for homogeneous catalysis

In addition to the thermodynamic descriptors, we use Pourbaix diagrams to identify catalysts that would take part in energetically efficient in electrochemical CO_2 reduction. Pourbaix diagrams are thermodynamic phase diagrams that help predict the species involved in CO_2 reduction by plotting out the thermodynamically relevant intermediates in an aqueous electrochemical redox environment. Using a similar framework to calculating redox potentials and hydricites, we plotted Pourbaix diagrams. Constructing a Pourbaix diagram for any homogenous catalyst is a multi-step process.

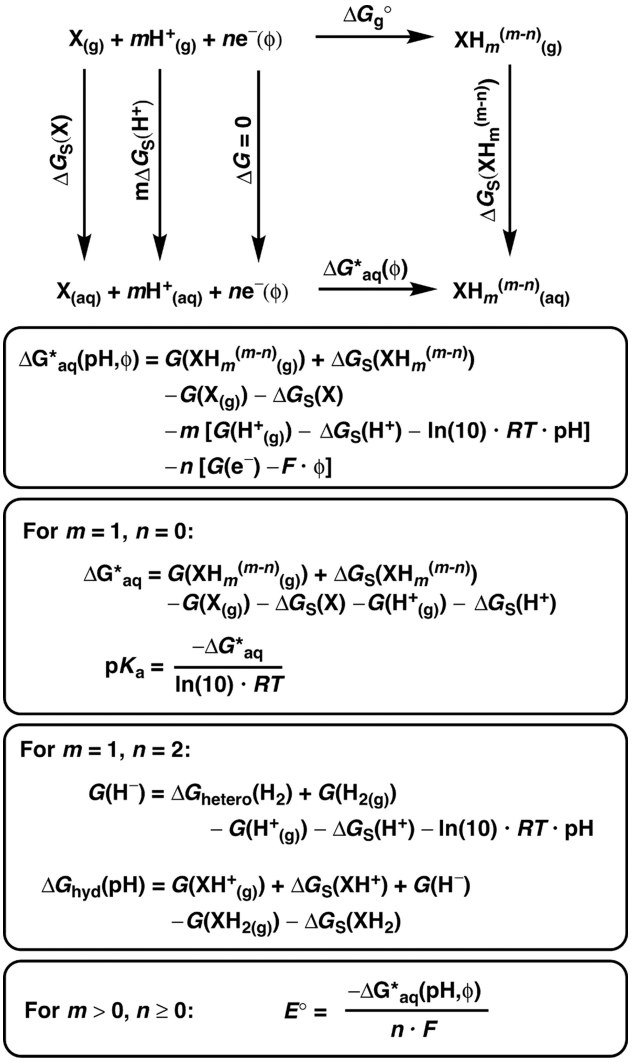

Figure 1.2: Thermochemical cycle and expressions used to calculate electrochemical energies. "Reprinted with permission from [19]. Copyright 2018 American Chemical Society."

Step 1: Map out all possible intermediate states that are obtained by adding upto m number of protons and n number of electrons to the molecule. Figure 1.3 shows the map of all possible proton coupled electron transfers upto $2H^+$ and $2e^-$ to pyridine, which was shown to be a energetically efficient CO_2 reduction catalyst. We consider all possible protonation sites for all degrees of protonation.

Step 2: We calculate electrochemical free energies of all the intermediate states shown in

Figure 1.3. Since pH and applied potential can vary in an real electrochemical experiment, we derive thermodynamically consistent approximation to account for pH and potential effects on the electrochemical free energy.

$$\Delta G_{rxn} = G_{int} - G_{ref} - m \times G_{H^+} - n \times G_{e^-} \tag{1.1}$$

$$G = E_{SCF} + H - TS + G_{solv} \tag{1.2}$$

$$G_{H^+} = -272.3 - k_B \times T \ln 10 \times pH \times 23.061 + 1.89 \tag{1.3}$$

$$G_{e^-} = -(U + 4.480) \times 23.061 \tag{1.4}$$

G_{ref}, G_{H^+} and G_{e^-} are the free energies of reference state (pyridine), H^+ and electron. E_{SCF} is the energy of the system calculated by DFT, H and TS accounts for the enthalpic and entropic contributions which are calculate by rigid rotor approximation. G_{solv} is the solvation energy of the molecule as calculated by continuum solvation models like PCM/SMD/COSMO. pH and applied potential corrections are accounted for in the free energies of H^+ and electron.

Step 3: We then calculate the relative energies of all the intermediates (Figure 1.3) with respect to the reference molecule as a function of pH and a potential of 0 V vs SCE (Figure 1.4 a) We see that pyridinium is stable from a pH of 0 until 6.5 (which is the pKa of pyridine) after which pyridine becomes stable. At an applied potential of -0.58 V vs SCE, the energetics of all the intermediates get shifted downwards by an amount equal to the the number of electrons transferred (Figure 1.4 b). Now, we find that a dihydropyridine ($2H^+/2e^-$) becomes stable at lower pH. When the pH and the applied potential are varied and the species with lowest electrochemical free energy difference is identified at each of the conditions, we obtained a thermodynamic phase diagram known as the Pourbaix diagram (Figure 1.4 c).

A molecular Pourbaix diagram shows distinct regions where different intermediate states are stable. A vertical line in the Pourbaix diagram indicates conditions where there is efficient proton shuttling between the two states. Similarly, a horizontal line indicates conditions where electrons are efficiently shuttled between two states. Sloped lines indicate conditions ideal for proton coupled electron transfer between any two states where the slope of the line

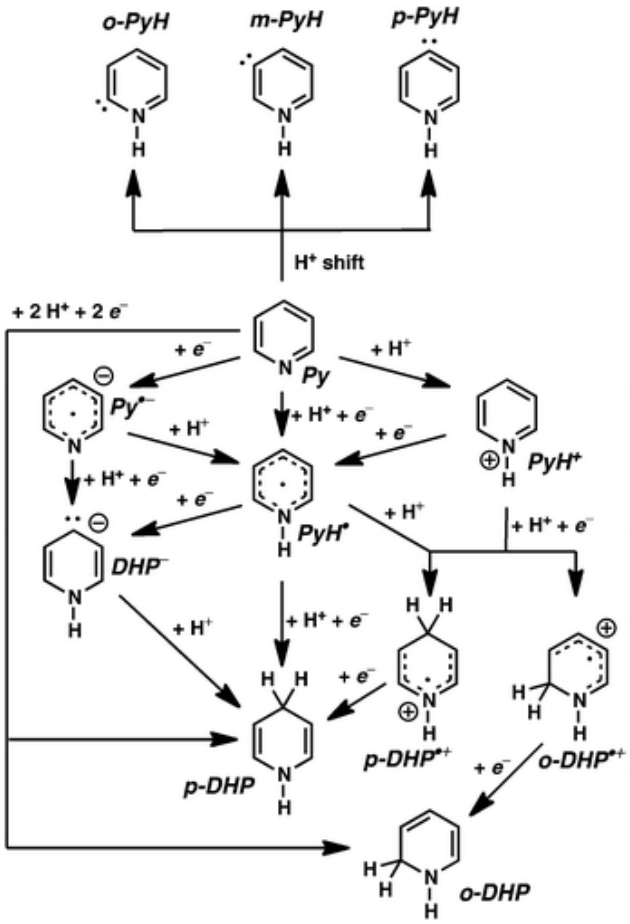

Figure 1.3: Possible intermediates during electroreduction of pyridine. "Reproduced from ref [20] with permission from The Royal Society of Chemistry."

is the number of electrons transferred. The triple point in the Pourbaix diagram indicates conditions where the molecule is an efficient proton, electron and hydride transfer agent. Interestingly, the thermodynamic triple point from the pourbaix diagram helps identify the species that might be involved in the reduction. The triple point also indicates the conditions at which a molecule can be a better hydride transfer agent to CO_2 for reduction.

In most of our work we considered catalysts in solution. Our approach actually considers two Pourbaix diagrams. One for the molecular catalyst (here, a pyridine molecule) as well as the Pourbaix diagram for CO_2 reduction in water, where CO_2 is actually found in water

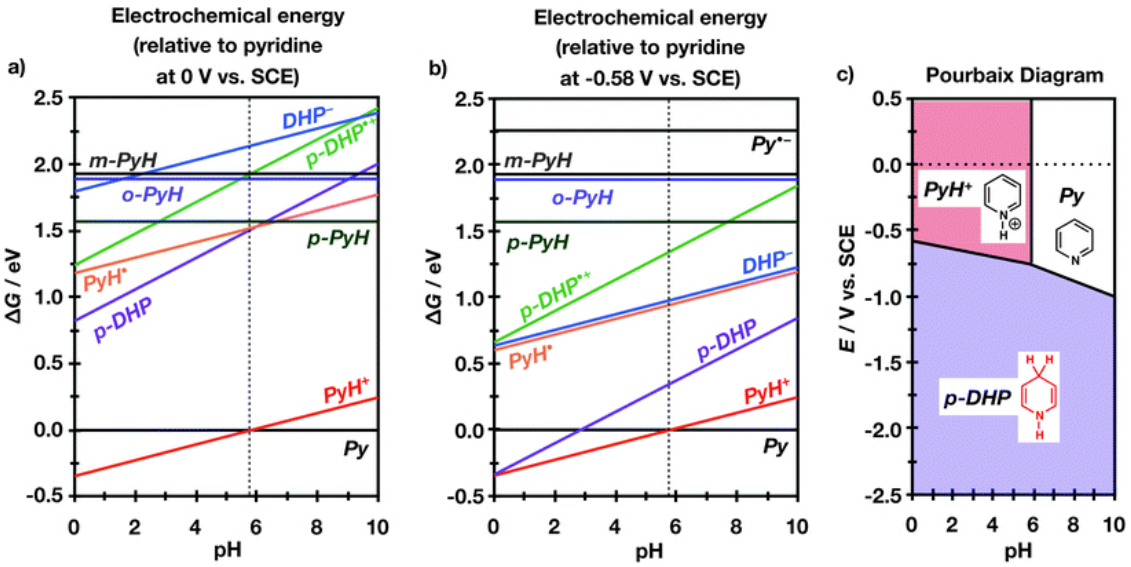

Figure 1.4: Relative electrochemical energies referenced to the energy of Py at an SCE potential of (a) 0 V and (b) -0.58 V vs. the SCE for pyridine species in solution at different pH. (Dotted line denotes the calculated pKa for PyH^+.) (c) Pourbaix diagram depicting the most thermodynamically stable species on low HER overpotential electrodes (e.g. Pt) at a given pH and electrode potential. "Reproduced from ref [20] with permission from The Royal Society of Chemistry."

as carbonic acid. When the two Pourbaix diagrams are overlaid on the other, we find that boundaries of the two Pourbaix diagrams are in close proximity to the other. The electrochemical conditions where boundary lines fall close to each other are where the Sabatier principle would be achieved. Another way to think of this is if the boundary of each Pourbaix diagram represents the top of a volcano curve. Conditions where two Pourbaix diagrams have boundaries close to each other are conditions were hydrogen catching and releasing (i.e. shuttling) is most favored. In general, the location of triple point measures the driving force for the reduced complex to donate a hydride to CO_2. The more negative potential of the triple point implies more driving force for the molecule to get reduced. If the triple point lies close to formic acid curve, then the catalyst is suitable for CO_2 reduction. Hence easier transfer of hydride for CO_2 reduction.

1.4.2 Pourbaix diagrams for heterogeneous catalysis

Pourbaix diagrams for molecular catalysts were plotted by considering intermediate states obtained by varying number of proton and electron transfers to the reference molecule. The free energy of proton and electrons were calculated separately using Equations (1.3) and (1.4) letting us look at states with unequal proton and electrons transfered. We follow similar steps outlined above to develop Pourbaix diagrams for heterogeneous catalysts but using a modified approach to modeling proton coupled electron transfers. In general, we use a slab model with periodic boundary conditions (PBC) to represent solid state catalysts. Adding a proton or a charged species to a catalyst under PBC represents a unphysical system and modeling such a system with DFT will not be meaningful. We overcome this by adding H atoms to the model system rather than adding a proton and an electron. But, using this method restricts us to only states that are obtained by transfering equal number of protons and electrons to the reference state. The electrochemical free energy of the intermediate state is calculated using a similar expression as above but we neglect solvation.

$$\Delta G_{rxn} = G_{int} - G_{ref} - m \times G_H \tag{1.5}$$

$$G = E_{SCF} + H - TS \tag{1.6}$$

Computational hydrogen electrode (CHE) model proposed by Norskov et al. is used [21] to approximate the free energy of a proton and an electron at different applied potentials. The CHE model is one of the most common computational techniques used to account for reaction energies that scale with pH and potential effects in computational electrocatalysis. According to the CHE model, the hydrogen evolution reaction (Equation 1.7) is in equilibrium at an applied potential of 0 V_{SHE} (for all pH values, all temperatures, and P_{H_2} = 1 atm).

$$H^+ + e^- \rightleftharpoons \frac{1}{2}H_2 \tag{1.7}$$

Based on the CHE, at zero potential relative to the Standard Hydrogen Electrode (SHE), the chemical potential of $\frac{1}{2}H_2$ is equivalent to the chemical potential of a proton and an

electron:

$$\frac{1}{2}\mu_{H_2} = \mu_{H^+} + \mu_{e^-} \tag{1.8}$$

The chemical potential of protons and electrons can be then related to pH and applied potential (E) as:

$$\mu_{H^+} + \mu_{e^-} = \frac{1}{2}\mu_{H_2} - 2.303 \cdot k_B T \ln(10) \cdot pH - E \tag{1.9}$$

Detailed thermodynamic derivations for the catalysts that we studied are provided in their respective chapters.

1.5 DISSERTATION OVERVIEW

Our group has specialized in the development of thermodynamic descriptors, specifically Pourbaix diagrams to understand energetically efficient catalysis of CO_2 electroreduction to methanol. We have shown triple points in Pourbaix diagrams to be useful descriptors of optimal thermodynamic activity in pyridine which have shown to be efficient CO_2 reduction catalyst. [20, 20, 19]. We also extended our Pourbaix diagram analysis to an extended library of aromatic nitrogen heterocycles. [22] We hypothesize that inorganic complexes and materials with a pyridine backbone could be potential candidates for CO_2 reduction. We have tested this hypothesis by carrying out a Pourbaix diagram analysis on ruthenium inorganic complexes in Chapter 3 and graphene nanocarbon materials in Chapter 4. We also tried to identify if tin oxide catalysts were suitable for CO_2 reduction using Pourbaix diagrams and proposed dopants to enhance their activity in Chapter 5.

2.0 COMPUTATIONAL HIGH THROUGHPUT SEARCHES FOR EFFICIENT CATALYSTS

Expensive and time consuming trial-and-errors experiments have been the traditional method of finding the best catalyst for a reaction.[23, 24, 25, 26, 27] High-throughput (HT) catalyst design using computational quantum chemistry can reduce the lab work and accelerate the catalyst discovery process. Computational HT studies combine Kohn-Sham Density Functional Theory (KS-DFT) and thermodynamic descriptors to rationally screen through a large number of pure, bimetallic and trimetallic alloys and identify suitable candidates that are efficient and stable under operating conditions of catalysis. Considerable successful using these methods for discovery of new catalyst materials have been reported.[28, 29, 30] One of the early studies in this field was by Greeley *et al* in which the high throughput screening approach was outlined and was used to search for the best hydrogen evolution reaction catalyst.[30] Nearly 700 bimetallic alloy electrocatalysts were screening using binding energy and stability descriptors. An alloy of BiPt was found to be a stable catalyst with predicted activity much better than pure Pt. The alloy was also synthesized experimentally and it showed improved activity confirming theoretical predictions. Several HT studies that followed made useful predictions of new and improved catalysts for experimentalists highlighting the importance of HT approach in rational design of catalysts.

All computational HT screening studies performed so far have been able to screen through only a limited number of bimetallic and ternary alloys. However, the chemical space of possible alloy catalysts is large enough that it is impossible to screen through the entire space using KS-DFT based HT studies. Combinatorially and theoretically speaking, one could obtain *more than 2.6 million hypothetical alloys* using a larger 3×3 surface unit cell with up to 18 transmutations to different *d*-block elements from the same row as the host

metal atoms in two top layers of the slab (see Figure 2.1). Calculating an adsorption energy using DFT would require twice as much calculations as the number of alloys that would need to be screened. A faster approach to obtain the adsorption energy on these alloys is needed to accelerate the screening process.

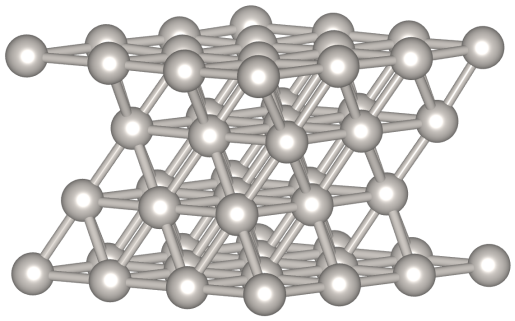

3x3 - (111) surface

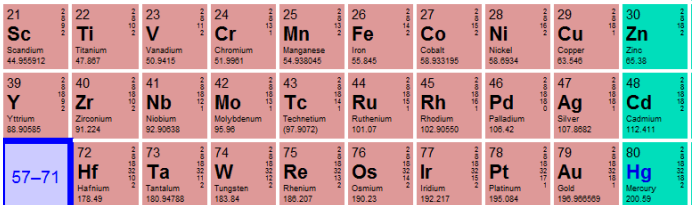

Number of sites per layer: 9

Number of layers: 2

Number of transmutations: 18

Number of possible alloys: 2.6 million

Figure 2.1: Chemical space of alloy catalysts

In our research program, we propose Computational Alchemy, a perturbation theory approach, as a tool to accelerate the traditional HT screening process. Using Alchemy, we want to predict and design catalytically active sites at the fraction of a cost of KS-DFT based screening. In a recently published work, we tested the accuracy of the method. We benchmarked binding energy predictions of oxygen reduction reaction intermediates on thousands of alloys of Pt, Pd, and Ni using alchemy against predictions from DFT. Far faster alchemical estimates yielded binding energies within 0.1 eV of DFT values in many cases. We also identified distinct cases where alchemy performed significantly worse, indicating areas where modeling improvements were needed. Our initial results have suggested that computational alchemy is a very promising tool that warranted further consideration for high-throughput screening of heterogeneous catalysts. In this proposed research, we want to develop Alchemy as a more robust tool for reliably screening through the chemical space and make it useful for accelerated catalyst discovery.

2.1 RATIONAL DESIGN OF ACTIVE SITES IN CATALYSTS

The "holy grail" in heterogenous catalysis is identifying the optimal active site on a catalyst surface for any given chemical reaction. In 1925, Hugh Stott Taylor proposed the idea of active sites on a solid catalyst stating that "there will be all extremes between the case in which all the atoms in the surface are active and that in which relatively few are so active".[31] His formulation of active sites has led to extensive research focusing on identifying, modifying and designing active sites for catalysis over the last century.[32, 33, 34]

Designing active sites of a catalyst requires a molecular level understanding of events taking place on the surface of a heterogeneous catalyst. The events that could happen on a surface include adsorption of the reactant molecules on the surface of the solid catalyst, diffusion on the surface, breaking and forming of bonds to form product molecules, and desorption from the surface. The picture gets much more complicated in an electrochemical interface where there are electrons in the system. However, using simpler models that approximate a real catalyst surface, computational quantum chemistry has been able to provide several useful insights into many surface reactions and guide the rational design of active sites in catalysis.[35, 36, 33]

2.2 BREAKING SCALING RELATIONS

Electronic structure calculations have been instrumental in establishing trends in the predicted activity of transition metal surface catalysts.[37] Scaling relations[38], d-band model[39], activity maps[40] are few of the useful tools that have advanced the understanding of heterogeneous catalysis. Scaling relations are correlations between bond energies of different adsorbed species on a surface. Scaling relations reduce the number of parameters that determine the rate of a catalytic reaction into a very few number of parameters known as descriptors. Based on a large number of calculations of adsorption energy data, it has been shown that scaling relations are much more general and they are able to describe all intermediates for a number of reactions on transition metal surfaces. In addition to explaining

trends and new catalyst design criteria, scaling relations have also defined limitations on the performance of large classes of catalysts. There are several reactions in which scaling relations have been able to identify limitations on the maximum rate possible on a catalyst, N_2 reduction[41], CO_2 reduction[42] and ORR[43].

New design approaches need to be developed to identify catalysts that do not follow scaling relations. In other words, we may need to find ways to stabilize one adsorbed state without stabilizing others. Considerable progress has been made in this direction. Since scaling relations are difficult to be broken when different reaction intermediates adsorb on the same surface site, multisite functionalization or catalysts with several types of active sites or local binding environments for different intermediates has been proposed. Alloying and doping are promising avenues to test multisite functionalization.

Alloy catalysts have been studied as ways to improve rates of electrochemical reactions even before scaling relations were identified and alloying was suggested as a way to enable multisite functionalization.[44, 45, 46, 47, 48] We list a few of the recent studies that have focused on bifunctional catalysts for several electrochemical processes. An experimental study focused on electrocatalysts where monolayers of Pt were deposited on different late transition metals (Au, Pd, Ir, Rh, or Ru) found that Pt supported on Pd ORR activity showed a 20-fold increase in ORR activity. [49] Experiments have also predicted ternary alloy electrocatalysts to have improved activities for ORR.[50, 51] Decomposition of ammonia into hydrogen was predicted to be enhanced when the platinum surface was alloyed with nickel.[52] Catalysts based on Au-Cd bifunctional alloys were explored using DFT and were found to be thermodynamically more favorable for CO_2 reduction to CO and methanol relative to pure Au.[53] All of these experimental and computational studies have considered relatively few material combinations. In order to accelerate the process and identify the best active sites in alloyed catalysts, a rapid screening approach is required.

2.3 HIGH THROUGHPUT SCREENING OF ALLOY CATALYSTS

Moderately large-scale combinatorial screening for alloy catalyst materials using density functional theory (DFT) calculations have been able to identify active sites with two or more elements.[28, 29, 30] They are based on a procedure in which a database of transition-metal surface alloys are efficiently screened using catalytic activity descriptors and detailed stability assessments. Using this procedure, alloy catalysts were evaluated for a fundamental electrochemical reaction, the hydrogen evolution reaction (HER) using δG_H and stability descriptors.[30] The HT search resulted in a surface alloy of bismuth and platinum which was experimentally synthesized and shown to have higher activity than pure Pt. In a similar combinatorial screening for an ORR catalyst, nearly 750 bimetallic surface alloys were screened and many candidates were found to be active for ORR. However, most of the identified candidates were thermodynamically unstable in acidic environments. After filtering based on potential dependent stability tests, Pd or Pt alloyed with early transition metals such as Sc or Y were predicted to be promising candidates.[29] Experiments also confirmed that the activity of Pt3Sc and Pt3Y electrodes were enhanced by a factor of 1.5-1.8 and 6-10 when compared to pure Pt. Better alloy catalysts have also been screened for methanation reaction using the same procedure.[54]

All HT screening studies use a similar screening process that involved multiple stages as shown in Figure 2.2.[55, 56] The first step involves identifying all possible candidate bimetallic surface catalysts combinatorially and calculating DFT data on each of the alloys. Then, all these candidates were passed through a multistage filtering process. The first filter was an activity descriptor, in which candidates were filtered based on DFT binding energy. The second stage of screening was based on set of stability criteria. The final candidates passing through the second stage warranted further experiments to confirm their activity and stability.

In HT studies, the descriptors play a key role in reliably finding a catalyst with desired properties. With robust thermodynamic descriptors, catalysts can be designed rationally by searching through the chemical space for materials with descriptors close to the optimum value that corresponds to the highest activity. A fundamental activity descriptor from

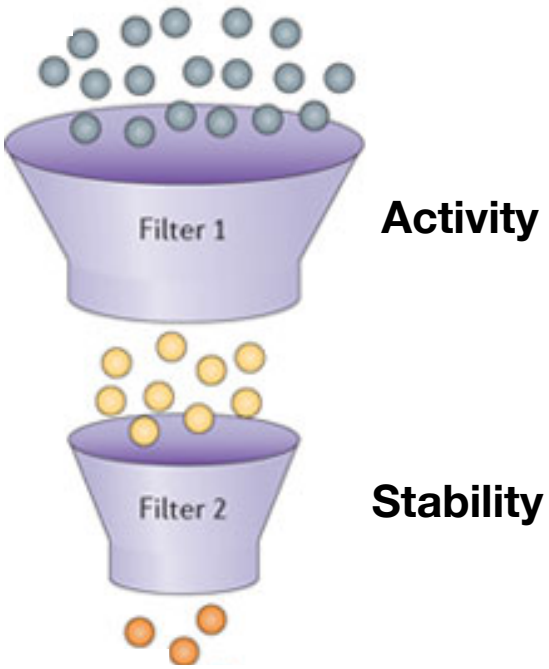

Figure 2.2: Procedure explaining the high-throughput screening process

DFT calculations that has been predictive of catalytic performance is adsorption energy. The usefulness of adsorption energy as a descriptor arises from a fundamental principle in heterogeneous catalysis, Sabatier principle. According to the Sabatier principle, an ideal catalyst should bind the adsorbate with an intermediate strength in order for energetically efficient catalysis to take place. It should bind neither too strong not to be able to desorb the product nor too weak to the adsorbate not to be able to activate the reactant. Sabatier principle can be best understood in the form of a volcano plot shown in Figure 2.3. By plotting the bond strength of an adsorbate to a catalyst surface or adsorption energy against activity, these plots help in the comparison of thermodynamics of a reaction between different catalysts. Volcano plots usually contain two slopes which meet at the top and the slopes indicate conditions in which surface/adsorbate interaction are too strong (left) or too weak(right). Thermodynamically, optimal candidates satisfying Sabatier's principle are found near the peak of the volcano.

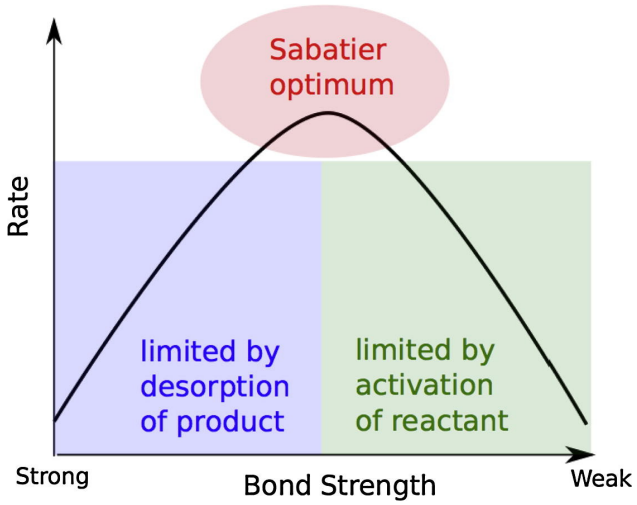

Figure 2.3: Volcano plot with overlaid Sabatier principle, [41]

Besides being active, alloy catalysts need to be stable under experimental conditions. They should not decompose in high-potential and highly corrosive conditions observed in electrochemical environments.[57] The stability of these alloy catalysts can be assessed by identifying processes that would make an alloy catalyst unstable like segregation, islanding and metal dissolution.[55, 56] Segregation is a process in which atoms from the inner layers of an alloy dissociate to the outer surface or vice versa. Islanding is the formation of single-component patches on the alloy surface caused by separation of alloy components within the surface plane. Metal dissolutions refers to the process in which the alloy elements dissolves into the electrolyte solution. All of these processes could be caused by inherent surface thermodynamics of the alloys under consideration, or changes in the surface energies resulting from adsorption. By calculating a free energy difference (stabilization free energy) between the alloy and modified alloy, stability of an alloy catalyst can be evaluated. Alloy catalyst is stable if it is energetically uphill to any process that would destabilize the catalyst.

2.4 COMPUTATIONAL ALCHEMY

High throughput screening studies performed so far screened through a moderate number of alloys (less than 1000). Combinatorially and theoretically, one could derive *more than 2.6 million hypothetical alloys* using a 3×3 surface unit cell with up to 18 transmutations to different d-block elements from the same row as the host metal atoms in two top layers of the slab. Screening through this large chemical space of alloys requires a faster way to generate binding energy data of the alloys. We introduce Computational Alchemy as a tool to accelerate the screening process by calculating the binding energy of alloys at a fraction of the cost of a DFT calculation.

Computational alchemy itself is not a new method. Its early applications have been used in biomolecular simulations to calculate protein ligand binding affinities [58, 59, 60]. An approach similar to alchemy, linear combination of atomic potentials (LCAP) has been used to screen through large libraries of molecules based on properties like molecular electronic polarizability and hyperpolarizability using an inverse design approach.[61] Modified variants of LCAP like tight binding LCAP[62], gradient-directed Monte Carlo[63] and a hybrid discrete-gradient LCAP[64] have also been developed to explore the molecular space. Alternatively, Alchemical Coupling was proposed as a more efficient way to explore the chemical compound space (CCS) by alchemically coupling two isoelectronic molecules in CCS through interpolation of their electron-nucleus potentials.[65, 66, 67, 68, 69] This method has been successfully used to estimate bulk properties like formation energies, lattice constants, and bulk moduli of ionic crystals[70] and 4d transition metals[71]. A variant of Alchemical Coupling (refered to as Computational Alchemy in this thesis) has also been proposed where a linear change in electrostatic potentials (alchemical derivatives) is used to estimate reaction energetics on doped catalysts. Binding energies of oxygen intermediates on alloyed nanoparticle catalysts[72] and water dissociation energetics on B-N doped graphene sheets have been calculated[73] using this approach.

2.5 DISSERTATION OVERVIEW

We hypothesize that if prior computational HT screening studies were able to identify promising alloy catalysts using activity and stability descriptors, Computational Alchemy should also be able to predict new active sites in catalysts but faster. As a first step, we introduce the methodology of Alchemy and show the effectiveness of Alchemy in calculating binding energies of OH_x intermediates in Chapter 6. We then extensively benchmark Alchemy for BE predictions and improving Alchemical BE predictions using Machine learning in Chapter 7.

3.0 ELECTROCHEMICAL CO_2 REDUCTION USING INORGANIC COMPLEXES

The content of this chapter is taken from Karthikeyan Saravanan, and John A. Keith, "Standard redox potentials, pK_as, and hydricities of inorganic complexes under electrochemical conditions and implications for CO_2 reduction". *Dalton Transactions*, 2016, 45(39), 15336-15341.

3.1 ABSTRACT

We use computational chemistry to systematically study the thermodynamic stabilities of protonated and reduced intermediate states for $[Ru(2,2'\text{-bipyridine})_3]^{2+}$, $[Ru(1,10\text{-phen})_3]^{2+}$, and $[Ru(phen)_2(pyrido[3',4':5,6]pyrazino[2,3\text{-f}][1,10]phenanthroline)]^{2+}$, in aqueous solutions. Following our previous studies of aromatic N-heterocycle molecules, we report pKas, standard redox potentials, and hydricities as well as com- putationally derived Pourbaix diagrams that show which states would be thermodynamically stable at different conditions of pH and applied potential. Locations of added electrons within ligands and complexes after reductions are also shown with electron density difference plots. As with other aromatic N-heterocycle molecules implicated in CO_2 reduction, we find that several of the boundary lines from the Pourbaix diagrams are in close proximity to the thermodynamic redox potentials for CO_2 electroreductions, making them thermodynamically appropriate for energetically efficient hydrogen shuttling.

3.2 INTRODUCTION

Ruthenium complexes such as $[Ru(bpy)_3]^{2+}$ bpy = 2,2′-bipyridine (1) and $[Ru(phen)_3]^{2+}$ phen = 1,10-phenanthroline (2) are used in various photo- and electrochemical reactions.[74] MacDonnell and coworkers[75, 76, 77] recently reported photocatalytic reduction of CO_2 into products such as methanol with low overpotentials and high selectivities. One of their studies used 2 in aqueous electrolytes containing a weak acid, pyridinium (PyH^+). It was suggested that **2** provides electrons that enable PyH^+ to participate in electrochemical reductions related to the PyH^+ catalyzed processes reported by Bocarsly and coworkers.[78, 79, 80] Another example by MacDonnells group demonstrated photochemical and electrochemical reduction of $^{13}CO_2$ into methanol using complexes having a modified phenanthroline ligand that contained a pendant pyridyl functionality, $[Ru(phen)_2(ppy)]^{2+}$, ppy = pyrido[3′,4′:5,6]pyrazino[2,3-f][1,10]phenanthroline (3).[76]

Both complexes result in similar products and therefore may make use of a similar mechanism, but the specific experimental conditions and outcomes of the systems using **2** and **3** are different. The system employing **3** had poor stability in water, so a mixed solvent comprised of water and DMF was used that did not involve PyH^+. The system using **3** was found to be slightly superior as a methanol producing photocatalyst compared to the system using **2** in terms of quantum yield. However, the TON for all products in the rst hour for **3** was found to be 27 on an electron basis while the TON for all products for the system using **2** and PyH^+ was 154. While this implies that **3** is a less active catalyst, **3** was also found to be more selective for methanol and generates more product in the rst hour on both an absolute quantum yield and relative basis.

We are not aware of any computational studies on these processes. Before embarking on complex reaction mechanism investigations, we carried out extensive atomistic thermodynamics studies to identify protonated and reduced intermediates as we had previously done for pyridine, imidazole, 1,3-dimethyl imidazolium, and phen, considering up to two proton and two electron transfers.[19] Our earlier work presented Pourbaix diagrams that identified electrochemical conditions where molecular additives (here, aromatic N-heterocycles) might function as multi-proton and multi-electron shuttles. We now do a similar analysis

on a progression of aromatic N-heterocycle ligands (Figure 3.1 a - c) as well as complete inorganic complexes involving these ligands (Figure 3.1 d - f) to better understand their electrochemical reactivities in aqueous solution.

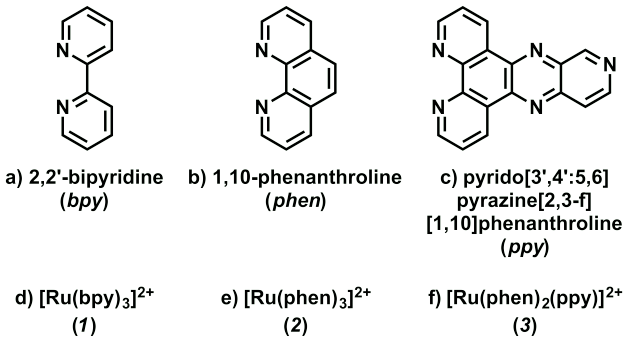

Figure 3.1: Ligands and Ru complexes modeled in Chapter 3

3.3 COMPUTATIONAL METHODS

All calculations employed Kohn-Sham density functional theory (KS-DFT) using the resolution of the identity (RI)-approximation[81, 82, 83] as implemented in the TURBOMOLE[84] code. Nuclear coordinates were optimized at the B3LYP[85, 86]/def2-SV(P)[87] level of theory. Hessian calculations confirmed that all optimized structures had only real vibrational frequencies showing that all structures are minimum energies on the Born-Oppenheimer potential energy surface. Single point electronic energies were then calculated on these structures using much larger def2-TZVPD basis sets.[88] COSMO[89] solvation implemented in Turbomole and def2-SV(P) basis set were used to calculate the solvation energies for these species in water. Note that our data will not be directly relatable to some of MacDonnell and co-workers studies that used mixed solvents, but this is discussed in more detail below.

Descriptions of calculation schemes to calculate pK_as, standard redox potentials (SRPs), and hydricities can be found in our earlier work.[19] A comparison of calculated and available experimental data is reported in Table 3.1. In general, our calculated data from our models are in reasonable agreement with experimental values in the literature.[90, 91, 92] The largest errors in SRPs involve either a radical anion (bpy$^{\bullet-}$ or phen$^{\bullet-}$), a dication with protons at each N site on bpyH$_2^{2+}$ and phenH$_2^{2+}$, or the reduction of **2**. This represents a rough measure of the expected accuracy of SRPs, pKas, and hydricities reported later in the text.

3.4 RESULTS AND DISCUSSION

Figure 3.2 are square-plots that report individual pK_as, SRPs, and hydricities for intermediates starting from species shown in Figure 3.1. Figure 3.3 shows a subset of the thermodynamic data in the form of overlaid Pourbaix diagrams. Section 1.4 provides an explanation for how we generate Pourbaix diagrams using quantum chemistry data. We also attach density difference illustrations that uniquely show the location of the LUMO orbital for the lowest energy structure at a given number of proton and electron transfers in Appendix A . The overlaid Pourbaix diagrams compare the stabilities of different protonated and electrochemically reduced forms of the three ligands and complexes (colored regions with labels in lower case) with the intermediates relevant in aqueous phase CO_2 reduction (dotted lines with labels in upper case). As an example for how to interpret this figure, Figure 3.3a shows the Pourbaix diagram for bpy (colored region) overlaid with the Pourbaix diagram for aqueous phase CO_2 reduction (dotted lines). The borders of the colored regions correspond to loci (paired values of pH and applied potential) where different protonated and reduced states have the same chemical potential. Note that a pK_a defines the pH where protonated and deprotonated states have equal chemical potentials, so the pK_a for bpy is shown by the vertical dividing line at pH 3.9. At this pH and at applied potentials more negative than -0.75 V vs. Ag/AgCl, our calculations show that it would be thermodynamically favorable to form an electrochemically reduced state, bpyH$_2$, as long as kinetic barriers permit it. At pH 3.9 and E = -0.75 V, the calculated chemical potentials for bpy, bpyH$^+$, and bpyH$_2$ states

Table 3.1: Benchmarking calculated thermodynamic descriptors with available experimental data for inorganic complexes

SRPs	Experimental / V vs Ag/AgCl	Calculated / V vs Ag/AgCl (signed error)
$bpy + e^- \rightarrow bpy^{\bullet -}$	-2.32[81]	-1.97 (0.35)
$bpyH^+ + e^- \rightarrow bpyH^{\bullet}$	-1.16[81]	-1.10 (0.06)
$bpyH_2^{2+} + e^- \rightarrow bpyH_2^{\bullet +}$	-0.69 [81]	-0.41 (0.28)
$bpy + 2H^+ + 2e^- \rightarrow bpyH$	-0.83[81]	-0.92 (-0.09)
$phen + e^- \rightarrow phen^{\bullet -}$	-2.18[81]	-1.91 (0.27)
$phenH^+ + e^- \rightarrow phenH^{\bullet}$	-1.04[81]	-1.02 (0.02)
$phenH_2^{2+} + e^- \rightarrow phenH_2^{\bullet +}$	-0.66[81]	-0.37 (0.29)
$Ru(bpy)_3^{2+} + e^- \rightarrow Ru(bpy)_3^{\bullet +}$	-1.21[84]	-1.37 (-0.16)
$Ru(phen)_3^{2+} + e^- \rightarrow Ru(phen)_3^{\bullet +}$	-1.15[82]	-1.53 (-0.38)
pK_as	Experimental /	Calculated / (signed error)
$bpy + H^+ \rightarrow bpyH^+$	4.4[81]	3.9(-0.5)
$phen + H^+ \rightarrow phenH^+$	4.9[81]	3.4(-1.5)
Hydricity	Experimental / eV	Calculated / eV (signed error)
$CO_2 + H^- \rightarrow HCO_2^-$	1.45[83]	1.40(-0.05)

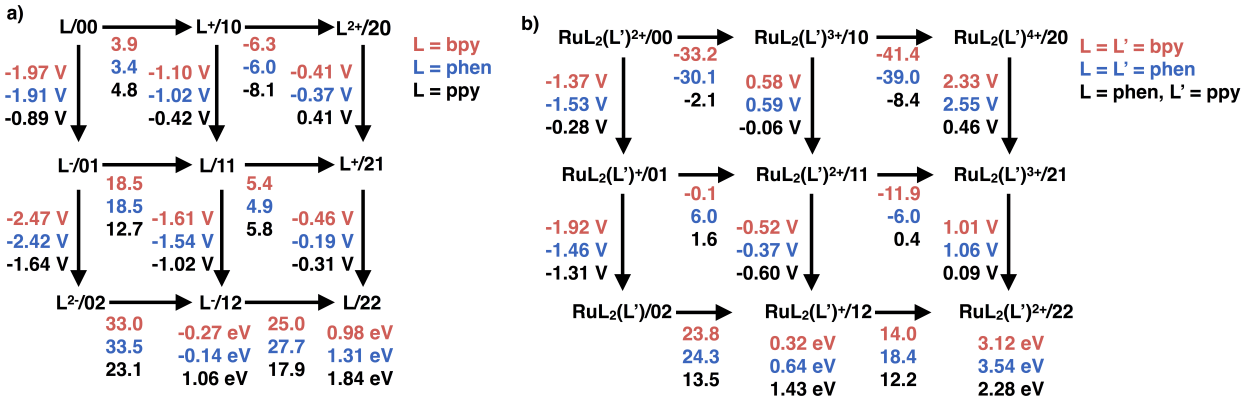

Figure 3.2: Square plots denoting calculated SRPs, pK_as, and hydricities for a) ligands and b) Ru complexes. The first and second digits in the labels following the '/' correspond to the number of protons and electrons added to the initial species from Figure 3.1, respectively.

are all the same, and this represents an idealized electrochemical environment that would support shuttling protons and electrons amongst the three different states. Since these diagrams are only a thermodynamic construct, it is not immediately apparent what proton and electron transfer pathways might occur, or if such pathways would be kinetically allowed. The diagrams nevertheless provide useful information about what species are metastable at which electrochemical reaction conditions. When loci that represent electron transfers between molecular states reside at potentials more negative than the loci representing CO_2 reduction (or its expected form of H_2CO_3 in a buffered aqueous solution), this also signifies an electrochemical environment that might create a reversible proton and electron shuttle that would have sufficient driving force in turn to reduce CO_2. Similar to what was found in our previous study on other aromatic N-heterocycles, Pourbaix diagrams in Figure 3.3 show loci that lie reasonably close to the SRPs for aqueous phase CO_2 reduction. These data signify that these molecules may have a participating role in energetically efficient multi-proton and multi-electron transfers at electrochemical conditions where dotted lines and boundaries of colored regions are close. The degree that such mechanisms would occur in an appreciable amount would be straightforwardly measured by looking for H/D isotopic scrambling.

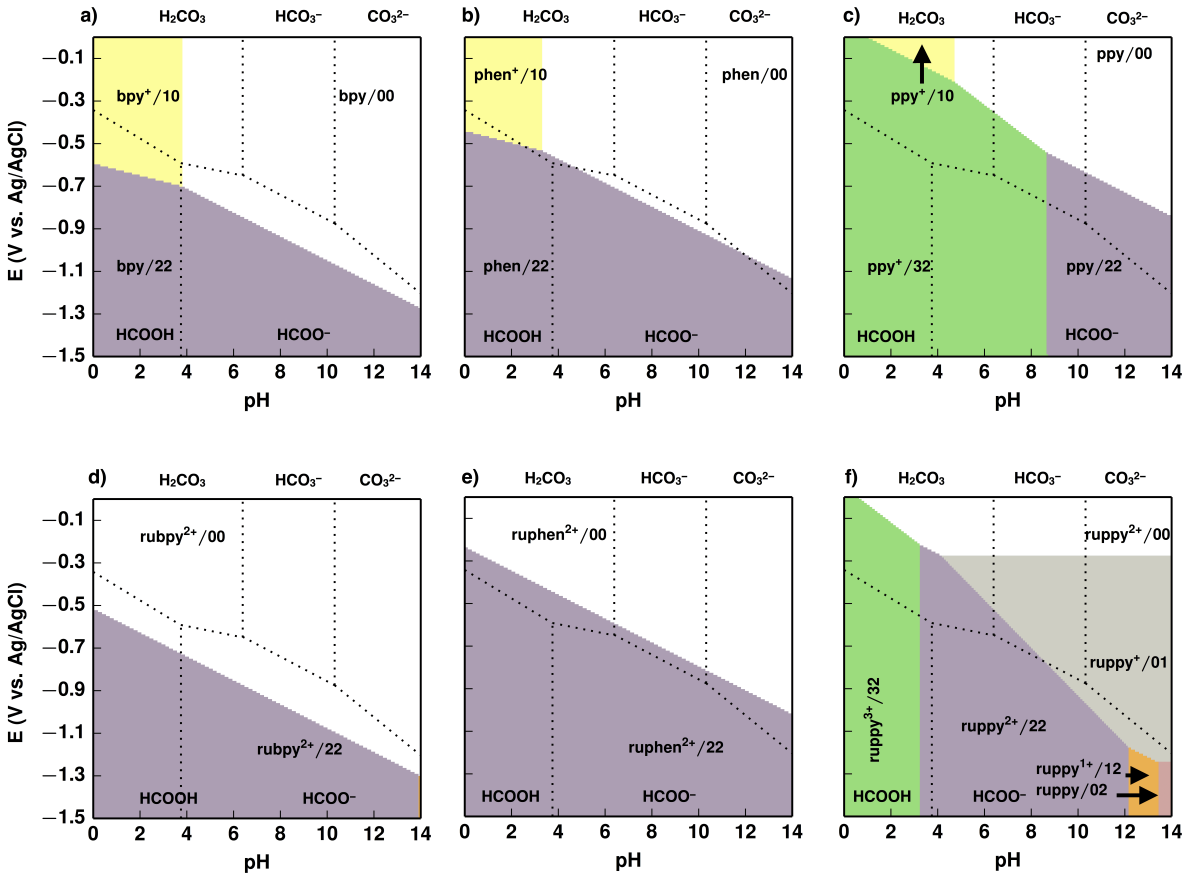

Figure 3.3: Pourbaix diagrams showing thermodynamically stable protonation and electrochemically reduced states for a) bpy, b) phen, c) ppy, d) 1 = $rubpy^{2+}$, e) 2 = $ruphen^{2+}$, e) 3 = $ruppy^{2+}$ overlaid on Pourbaix diagrams for CO_2 reduction intermediates. Pourbaix diagrams for the different ligands and complexes have lowercase labels that correspond to different colored regions. Numbers following each label refer to the numbers of protons and electrons relative to the initial ligand or complex. Pourbaix diagrams for the different states of CO_2 in aqueous solution have uppercase labels that correspond to different regions separated by dotted lines. We posit that pH and applied potentials where dotted lines overlap with boundaries of colored regions denote electrochemical conditions where energetically efficient proton and/or electron shuttling is thermodynamically feasible.

Regarding electrochemical studies using **1** and **2**, calculations show that except at highly basic conditions (pH > 14), it is thermodynamically more favorable to reduce either complex by adding two protons and two electrons to each complexs respective ligand than it is to carry out a single $1e^-$ reduction of either complex. While $2H^+/2e^-$ reductions of **1** and **2** have SRPs that might be accessible under CO_2 reduction conditions, experimental Pourbaix diagrams for **1** and **2** typically show no indication of multi-proton and multi-electron transfers, so it would be uncontroversial to assume that such processes are kinetically hindered under most experimental conditions. Additionally, protonations of **1** and **2** are very energetically unfavorable, as denoted by the very negative pK_as in Figure 3.2. This raises some question over the actual mechanisms for CO_2 reduction involving **2** and PyH^+. Technically, the SRP for **2** is negative enough to reduce PyH^+ into $PyH^\bullet$ (SRP = -1.5 V) but such radicals are highly unstable, and their self-termination rates in partially aqueous solvents are on the order of 108 M^{-1} s^{-1}.[93] Furthermore, while Colussi and coworkers demonstrated $PyH^\bullet$ radicals generated from 254 nm photolysis of Py can reduce CO_2,[94] **2** exhibits MLCT absorptions far lower in energy in the 400-500 nm region. Due to this discrepancy in wavelengths, it seems more probable that **2** would participate in CO_2 reduction in some manner of electron transfer besides the formation of $PyH^\bullet$ radicals. For these reasons we also suggest that future mechanistic studies invoking the presence of $PyH^\bullet$ radicals would ideally be supported with spectroscopic evidence.

As with complexes **1** and **2**, we find intermediates that result from $2H^+/2e^-$ reductions of **3** would be metastable. However, the proton accepting ability as well as the $1e^-$ SRP are substantially less negative than those for **1** and **2**. This is due to the fact that the ppy ligand of **3** has accessible Brnsted base sites for protons and a significantly larger pi system that can accommodate electrons. We believe that the reduction of **3** into a $2H^+/2e^-$ intermediate might well have a lower barrier than that for **1** or **2**. It follows that **3** may then participate in energetically efficient shuttling of hydrogen atoms and protons (likely between $Ru(phen)_2(ppy)^+$ and $Ru(phen)_2(ppy)H_2^{2+}$) at conditions where $4 < pH < 12$ and at potentials slightly more negative than the SRP for CO_2 reduction. According to our calculations, the pH would need to be greater than 9 for there to be enough of a driving force to reduce bicarbonate into formate at potentials more negative than -0.7 V vs. Ag/AgCl.

We also find that within a relatively small pH window of 12 < pH < 13.5, the catalyst may also be shuttling single protons and electrons between $Ru(phen)_2(ppy)^+$ and $Ru(phen)_2(ppy)H^+$. If this pathway were operational, it would be expected that **3** would facilitate the reduction of the state that is conventionally attributed as a carbonate anion into formate but at potentials more negative than -1.1 V vs. Ag/AgCl. Note that the thermodynamics for this hydrogen atom shuttling mechanism is still significantly more favorable than the energetics required to generate $PyH^\bullet$ radicals.

We now relate our calculated data to experiments using **3**. We do not currently know the absolute solvation energies of H^+ or the absolute value of the standard hydrogen electrode potentials in mixed solvents, so our studies modeling aqueous solvents may have only limited connection to experiments carried out in mixed solvents. MacDonnell and co-workers[76] report a reduction occurring at -0.57 V in mixed DMF:H_2O solvents. Those authors assigned this SRP to the $1e^-$ reduction of $Ru(phen)_2(ppy)^{2+}$ into $Ru(phen)_2(ppy)^+$. We calculate this SRP to be -0.27 V in water. If mixed solutions exhibited properties that could be interpolated between DMF and water, then the SRPs in mixed solvents should be more negative than values in aqueous electrolytes, and therefore computational and experimental data would likely be in agreement. However, we note that we found another SRP that is also relatively close to this value, -0.70 V for the $2\ H^+/1\ e^-$ reduction of $Ru(phen)_2(ppy)^+$ into $Ru(phen)_2(ppy)H_2^{2+}$. This signifies that net $2H^+/2\ e^-$ reductions of **3** into $Ru(phen)_2(ppy)H_2^{2+}$ may be thermodynamically accessible under reaction conditions used by MacDonnell and co-workers. If so, **3** may be participating in CO_2 reduction mechanisms involving unexpected biomimetic proton and hydride transfers as speculated by previous computational studies.[20, 20, 95, 96] Quantifying SRPs in mixed solvents will be a focus of future work.

3.5 CONCLUSION

We have carried out an extensive atomistic thermodynamics study of aromatic N-heterocycle ligands and Ru complexes using first principles quantum chemistry. We have determined pK_as, SRPs, and hydricities for these molecules and inorganic complexes considering up to two proton and two electron transfers to determine which states would be thermodynamically stable under electrochemical CO_2 reduction operating conditions. As found previously with our other studies on aromatic N-heterocycles, the molecules and complexes modelled here have several metastable states that include up to multiple proton and electron transfers. These intermediate states in principle may open unexpected pathways for CO_2 hydrogenation such as biomimetic proton and hydride shuttling.

While the pK_as and $1e^-$ SRP for $[Ru(bpy)_3]^{2+}$ and $[Ru(phen)_3]^{2+}$ suggest high energy barriers for protonation and reduction of those complexes, it remains unclear how $[Ru(phen)_3]^{2+}$ would participate in CO_2 reduction in light of the instability of $PyH^{\bullet}$radicals. However, the $Ru(phen)_2(ppy)_2^{2+}$ system used by MacDonnell and coworkers for CO_2 reduction is a much more likely candidate for participating in CO_2 reduction mechanisms involving proton and electron shuttling. In this system, computational predictions indicate that proton and hydride shuttling pathways are thermodynamically feasible and should be considered for energetically efficient CO_2 reduction processes involving $Ru(phen)_2(ppy)_2^{2+}$.

4.0 NITROGEN-DOPED NANOCARBON MATERIALS UNDER ELECTROREDUCTION OPERATING CONDITIONS AND IMPLICATIONS FOR ELECTROCATALYSIS OF CO_2

The content of this chapter is taken from Karthikeyan Saravanan, Eric Gottlieb, and John A. Keith, "Nitrogen-doped nanocarbon materials under electroreduction operating conditions and implications for electrocatalysis of CO_2." *Carbon*, 2017, 111, 859-866.

4.1 ABSTRACT

We have used Kohn-Sham density functional theory with atomistic thermodynamics to identify various forms of N-doped graphene basal planes and nanoribbons that are thermodynamically relevant for CO_2 electroreductions. Using our computational results, we derive phase diagrams for different nanocarbon structures, and we report which structures are suitable for hydrogen transfers to CO2 with low over- potentials. With the incorporation of N atoms, standard reduction potentials resulting in hydrogenated surfaces become less negative, and this effectively opens pathways for hydrogen atom shuttling to CO_2 with reversibly hydrogenating nanocarbon catalysts. Of all morphologies considered, N-doped zigzag nanocarbon edges are most favorable for energetically efficient CO_2 electroreductions.

4.2 INTRODUCTION

Catalysts are a cornerstone of modern society that enable large scale chemical and fuel production. Active catalysts are non-reactive materials that bind to and release chemically reacting intermediates, lowering activation barriers for desired products. Most catalysts today are precious metals because they resist oxidation (i.e. they are noble) while having s and d orbital states that can reversibly bind reaction intermediates.[97] However, precious metals are scarce and alternatives are required for more economical and sustainable catalysis.[98, 99, 100, 101]

Recent research has demonstrated that carbonous materials are a promising avenue for advanced catalysis. Historically, activated carbons have been used as supports for metal catalysts because of their high surface area and electrical conductivity,[102, 103] but more recently they are being considered as catalysts themselves. Producing so-called 'metal-free' catalysts requires a great deal of synthetic control.[104] Synthetic routes include nanostructuring, heteroatom doping, and other defect control.[105, 106, 107, 108, 109] Catalytic properties have been reported to depend on a myriad of factors relating to their synthesis, including confinement effects,[110, 111] material defects,[112, 113] and heteroatom dopants.[104] Additionally, it is difficult to draw meaningful conclusions from experimental works alone due to metal impurities.[114, 115]

Even with rapidly growing synthetic sophistication, the field of carbon as a catalyst is still in relatively nascent stages. Factors that govern their catalytic performance are not well understood, and thus it is challenging to rationally improve their performances. Quantum chemical (QC) modeling can provide useful insights into why carbon catalysts might work and how to improve them, but the majority of QC studies to date have focused on electronic structures and material properties of nanoscale carbon morphologies such as zigzag edges, armchair edges, and basal planes.[116, 117, 118, 119] To a lesser but still sizable degree, QC studies have investigated catalytic reaction mechanisms on nanocarbons (e.g. the hydrogen evolution reaction[120, 121], the oxygen reduction reaction[119, 116, 122]). To an even lesser extent CO_2 reduction has been investigated, where experiment and theory have been used to identify specific active sites, and catalyst stabilities.[123, 124, 125, 126, 127]

Previous mechanistic studies on CO_2 reduction have focused on individual reaction steps involving CO_2 binding at different nanocarbon sites.[128, 129] However, it is also possible that a catalyst might undergo (electro-)chemical reactions itself under *in operando* conditions, thus resulting in a modified catalyst. We[130, 131] and others[132] have proposed that electrochemical $2H^+/2e^-$ reductions of pyridine molecules can form dihydropyridine molecules that facilitate energetically efficient CO_2 reduction processes originally reported by Bocarsly and coworkers.[133, 78] A motivating factor for the current work is to determine if knowledge about the electrochemical behavior of pyridine is also transferable to the design of catalytically active N-doped nanocarbon materials.

The first step toward understanding catalytic reaction pathways is to quantify and understand reaction thermodynamics. The Sabatier Principle effectively states that an ideal catalyst will bind reactants just strongly enough to activate them while also minimizing barrier heights to form and release products. To understand reaction energetics of electrocatalytic reaction mechanisms, the computational hydrogen electrode model[134] is a common starting point.

Another related approach is to use QC modeling to generate Pourbaix diagrams to determine which morphologies might evolve during electrochemical reductions and which structures might participate in energetically efficient hydrogenations. Pourbaix diagrams do not provide kinetic information, but the insight into thermodynamics they provide is nevertheless useful. In particular, boundaries between different phases shown by a Pourbaix diagrams are loci of electrochemical conditions (pH and applied potential, E) where the chemical potentials of the phases are the same. If the different morphologies represent different reaction intermediates, the boundaries correspond to theoretically optimal conditions for energetically efficient catalysis according to the Sabatier Principle. For instance, if the different states were a hydrogenated surface and an unhydrogenated surface, the boundaries would denote theoretically ideal pH and applied potentials where the surface would be an energetically efficient hydrogen shuttling catalyst.

To understand which carbon morphologies are best suited as CO_2 reduction catalysts, we use QC calculations to generate Pourbaix diagrams that identify thermodynamically relevant structures at reducing conditions. Our approach follows a similar spirit to previous work

regarding aromatic N-heterocycles present in homogeneous solution.[20, 19] In these works, we screened a variety of catalyst intermediate states using molecular Pourbaix diagrams that identifed electrochemical conditions for energetically efficient catalytic reactions. In the present work, we systematically explore the thermodynamic energies of different nanocarbon structures with different degrees of nitrogen defects and coverages of H atoms.

4.3 THERMODYNAMIC DERIVATION

We used ab initio atomistic thermodynamics[135] and computational hydrogen electrode model[134] to understand the thermodynamic stabilities of nanocarbon morphologies, graphene basal planes (GBP) and graphene ribbons (GR), having different N and H concentrations. We focused on a GR system with zigzag edges since this most closely resembles pyridine analogs that relate to our previous work [131].

We will first present a derivation for computing approximate Gibbs free energies (G) for graphene basal planes (GBP models) and then a modified derivation for graphene nanoribbons (GR models). To maintain a consistent energy scale for different nanocarbon morphologies, we use the energies of C in a graphene sheet, N as $\frac{1}{2}N_2$, and H as $\frac{1}{2}H_2$ as our reference states. Thus, the chemical formula for a general GBP consisting of a 4 $\times$ 4 unit cell (32 C atoms) with x N-doping atoms and y vacancy defects is then:

$$C_{32} + \frac{x}{2}N_2 -> C_{32-x-y}N_x + C_{x+y} \tag{4.1}$$

G is related to the Helmholtz free energy (A), $G = A + pV$, but for solids, pV is negligible in the free energy expression, leaving $G \approx A$. G is then defined as $G = E + G^{\text{vib}}$, where E is the electronic energy at zero temperature (here calculated using Kohn-Sham Density Functional Theory, DFT) and G^{vib}, comprises of the zero-point energy and vibrational entropy terms of the entire system obtained using the quantum mechanical harmonic oscillator approximation.

$$G^{\text{vib}} = \frac{-h}{2}\sum_i \omega_i + k_B T \sum_i \ln\left[\exp\left(\frac{h\omega_i}{k_B T}\right)\right] \tag{4.2}$$

The chemical potentials of C atoms (μ_{C}) is given by:

$$\mu_{\mathrm{C}} = g_{\mathrm{C}} \tag{4.3}$$

where g_{C} is the Gibbs free energy per atom of graphene (i.e. the cohesive energy). The chemical potential of N atoms in the system (μ_{N}) is given by:

$$\mu_{\mathrm{N}} = \frac{1}{2}\left[E_{\mathrm{N_2}}^{\mathrm{DFT}} + E_{\mathrm{N_2}}^{ZPE} + \mu_{\mathrm{N_2}}^{0}(T, p^0) + k_B T \ln\left(\frac{p_{\mathrm{N_2}}}{p^0}\right)\right] \tag{4.4}$$

The free energy change for the general reaction shown in Eq (6.1) is then:

$$\Delta G = [G_2 - G_1 + (x+y)\cdot\mu_{\mathrm{C}} - x\cdot\mu_{\mathrm{N}}] \tag{4.5}$$

where G_1 and G_2 are the energy of pristine graphene sheet and the modified graphene sheet, respectively. The chemical formula for electrochemically reducing a general GBP in an aqueous environment containing a source of protons and electrons is:

$$\mathrm{C_{32}} + \frac{\mathrm{x}}{2}\mathrm{N_2} + \frac{\mathrm{z}}{2}\mathrm{H_2} \rightarrow \mathrm{C_{32-x-y}N_xH_z} + \mathrm{C_{x+y}} \tag{4.6}$$

with free energy change of:

$$\Delta G = [G_3 - G_1 + (x+y)\cdot\mu_{\mathrm{C}} - x\cdot\mu_{\mathrm{N}} - z\cdot\mu_{\mathrm{H}}] \tag{4.7}$$

where z is the number of H atoms (each having a chemical potential of μ_{H}), and G_3 is the free energy of a reduced graphene with pyridinic vacancies. The standard reduction potential for the above process is then:

$$E^{\mathrm{red}} = \frac{-\Delta G}{nF} \tag{4.8}$$

where F is Faraday's constant and n is the number of electrons transferred. Based on the computational hydrogen electrode model, at zero potential relative to the Standard Hydrogen Electrode (SHE), the chemical potential of $\frac{1}{2}\mathrm{H_2}$ is equivalent to the chemical potential of a proton and an electron:

$$\frac{1}{2}\mu_{\mathrm{H_2}} = \mu_{\mathrm{H^+}} + \mu_{\mathrm{e^-}} \tag{4.9}$$

The chemical potential of protons and electrons can be related to pH and applied potential (E) as:

$$\mu_{\mathrm{H^+}} + \mu_{\mathrm{e^-}} = \frac{1}{2}\mu_{\mathrm{H_2}} - 2.303 \cdot \mathrm{k}_B\mathrm{T}\ln(10) \cdot \mathrm{pH} - \mathrm{E} \tag{4.10}$$

The final expression we derive for the free energy change for the electrochemical reduction of a general GBP is

$$\Delta G = E_3^{\mathrm{DFT}} - E_1^{\mathrm{DFT}} + \Delta G_{\mathrm{vib}} - x\left(\frac{1}{2}E_{\mathrm{N_2}} + \Delta\mu_{\mathrm{N}}\right) + (x+y)\cdot E_{\mathrm{C}} - z\left(\frac{1}{2}\mu_{\mathrm{H_2}} - 2.303 \cdot \mathrm{k}_B\mathrm{T}\ln(10) \cdot \mathrm{pH} - \mathrm{E}\right) \tag{4.11}$$

where $\Delta G_{\mathrm{vib}} = G_3^{\mathrm{vib}} - G_1^{\mathrm{vib}}$. Following a similar approach, the electrochemical free energy for reducing a N-doped graphene nanoribbon (GNR) is given as:

$$\Delta G = E_{\mathrm{GNR}}^{\mathrm{DFT}} - E_{\mathrm{GR}}^{\mathrm{DFT}} + \Delta G_{\mathrm{vib}} - x\left(\frac{1}{2}E_{\mathrm{N_2}} + \Delta\mu_{\mathrm{N}}\right) + x\cdot E_{\mathrm{C}} - z\left(\frac{1}{2}\mu_{\mathrm{H_2}} - 2.303 \cdot \mathrm{k}_B\mathrm{T}\ln(10) \cdot \mathrm{pH} - \mathrm{E}\right) \tag{4.12}$$

where $\Delta G_{\mathrm{vib}} = G_{\mathrm{GNR}}^{\mathrm{vib}} - G_{\mathrm{GR}}^{\mathrm{vib}}$, and $E_{\mathrm{GNR}}^{\mathrm{DFT}}$ and $E_{\mathrm{GR}}^{\mathrm{DFT}}$ are the DFT energies of modified graphene nanoribbon and pristine graphene nanoribbon.

4.4 COMPUTATIONAL METHODOLOGY

The electronic energies of all GBP and GR structures were calculated using spin polarized Kohn-Sham density functional theory (DFT) as implemented in VASP, a plane wave based DFT package.[136, 137] We used the PBE[138, 139] exchange-correlation functional and projector augmented wave pseudopotentials[140, 141] to describe the valence electrons of atoms in the system. We have performed convergence tests by varying the energy cutoff and k points until the formation energy was converged up to 10 meV/Å^2 in the case of GBP and 10 meV/Å in the case of GR. Plane waves with an energy cutoff of 800 eV and 4x4x1 k-points were used for all calculations on the GBP systems while an energy cutoff of 500 eV and 3x1x1 k-points were used for GR systems.

All structures were relaxed using conjugate gradient iterative minimization until the difference in energies between consecutive geometry steps was less than 10^{-6} eV. The convergence of size of the unit cell was tested for the pristine GBP system, and we found the formation energies did not change by more than 1 meV/Å^2 for a 4×4 unit cell. In the case of the GR system, the width of the zigzag ribbon was changed until the formation energies converged to less than 1 meV/Å. We found that a GR system with six zigzag lines across the ribbon width lead to converged energetics. Chemical modifications to the ribbon were made symmetrically to minimize dipoles. Future work focusing on reaction mechanisms will explicitly consider the cumulative role of local solvation environments of these materials at electrochemical interfaces.

4.5 RESULTS AND DISCUSSION

4.5.1 Basal planes

Using the computational hydrogen electrode model, we report the energetics for electrochemical reduction of various nanocarbon structures in terms of the energetics of different hydrogenation steps at different applied potentials. In our GBP models, we consider the reductions of both structures containing different numbers of doping N atoms (Figure 4.1) and of common defect sites (Figure 4.2). We will first report energetics for different hydrogenations and then use those data to report phase diagrams that show relative stabilities of different N-doped carbon morphologies.

For the GBP systems, all structures were optimized without spin polarization, but we determined magnetic moments on the optimized structures using spin polarized calculations, and we found those contributions were negligible except for the GBP+1H system that optimized to 1 μB. Our 4×4 unit cell model can accommodate a large number of configurations involving doped N atoms and H atoms that may arise from electrochemical reductions (see Figure 4.1). The substitutional energy of the first N atom or the binding energy of the first H atom is always the same due to the equivalence of binding sites on the GBP. We place

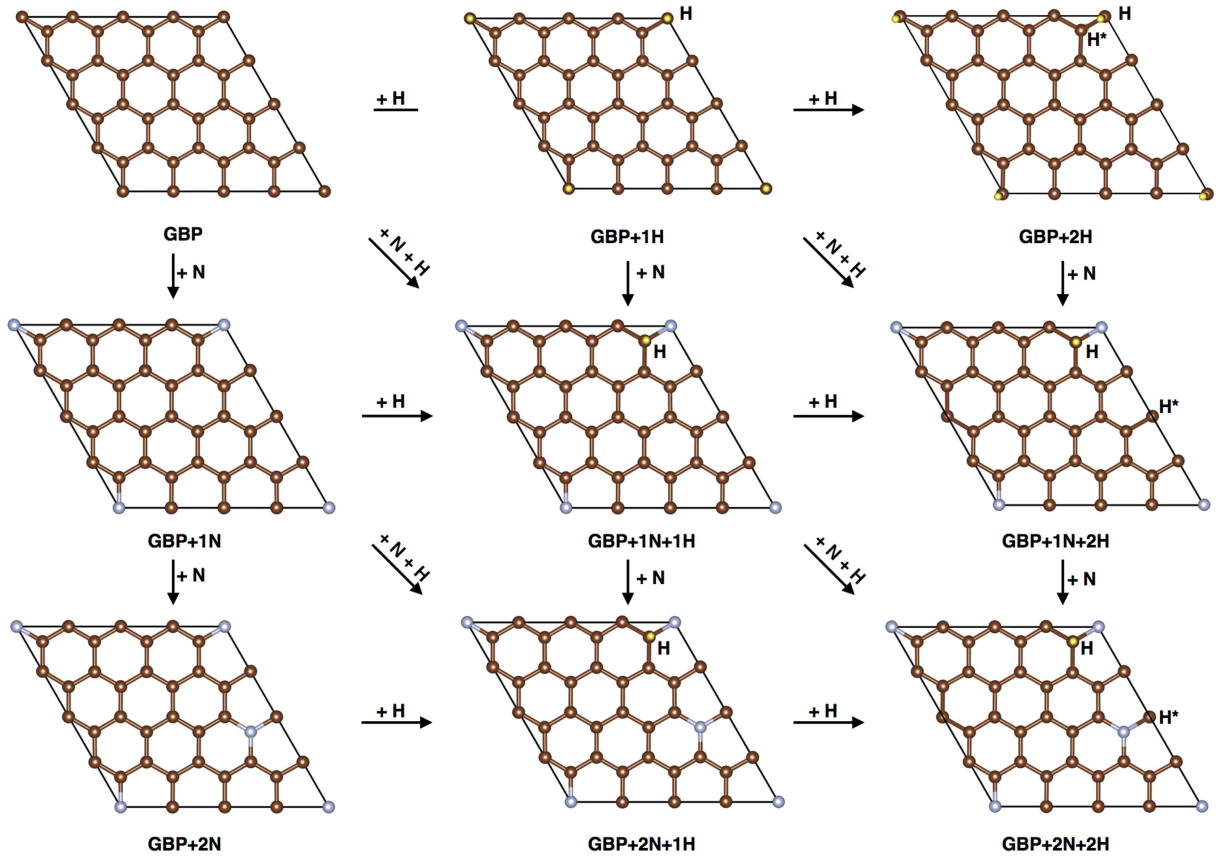

Figure 4.1: Lowest energy basal plane structures found in this work, consisting of different numbers of C (brown spheres), N (blue spheres), and H (yellow spheres) atoms. H and H* labels denote atoms on the top and bottom faces of the basal plane, respectively. The $x \times y$ unit cell is denoted by the black lines. The z direction has a 20 Å vacuum region.

the first N or H atom at the corner of the graphene unit cell. Starting from the GBP with one H atom (the GBP+1H system, which is uphill in energy by 1.44 eV) the second H atom preferentially binds one nearest neighbor away on the opposite side of the GBP at a site analogous to the *ortho* site for a pyridine molecule. These results are the same as previous computational studies by Boukhvalov et al.[142] who found that the energy of chemisorption at this site was uphill 0.54 eV.

The binding energy for the second H is even more uphill when it binds to the same side as the first H atom. Binding the first H atom to the GBP system disrupts aromaticity and results in a lattice distortion and a negative binding energy. One might assume that the second H atom would then bind more strongly since an energy penalty for disrupting aromaticity has already been paid by adding the first H atom. That is the case here, but it is still energetically uphill to add a second H atom to the GBP system. The next most favorable binding site is to a third nearest neighbor site (analogous to the *para* site for a pyridine molecule), which is further uphill by +0.40 eV compared to the *ortho* site. For our study we focus on lowest energy structures that would be relevant for thermodynamic phase diagrams, but all calculated binding energies are reported in Table 4.1.

Table 4.1: Binding energies (BE) of H to basal planes (GBP), planes with N-doped defects (P3N and P4N), and graphene ribbons (GR) with different concentration of N (positive values indicate bound states).

System	**BE / eV**
GBP+1H	–1.44
GBP+2H/ortho	–0.54
GBP+2H/para	–0.93
P3N+1H	2.64
P3N+2H	1.29
P4N+1H	1.80
P4N+2H	1.70
GR+1H	0.54
GR+2H	–0.05
GR+1N+1H	–0.40
GR+1N+2H	0.07
GR+2N+1H	–0.50
GR+2N+2H	–0.03

When the pristine graphene is doped with an N atom at the corner of the unit cell, the second N atom in the unit cell preferentially substitutes away from the first N atom. This indicates that GBPs energetically prefer lower nitrogen doping densities, which agrees with previous studies.[143] Since doping an N atom into graphene results in an increased magnetic moment at the adjacent carbon atoms, one might expect that these adjacent sites would accommodate binding H atoms having an unpaired electron. Indeed, the first adsorbed H atom on the singly and doubly nitrogenated graphene sheets will bind to sites adjacent to an N atom. The second H-adsorption site on the singly nitrogenated graphene sheet is four nearest neighbor atoms away, halfway between the two N atoms. The second H-adsorption site on the doubly nitrogenated graphene sheet is *ortho* to the other N atom. The proximity of adsorbed H atoms next to N atoms is potentially significant for catalysis, since this indicates that frustrated Lewis base pair sites[144, 132] will exist on electrochemically reduced nitrogenated graphene basal planes, similar to molecular dihydropyridine structures reported by computational groups.[130, 131, 132] This structural motif is considered suitable for energetically efficient hydrogenation pathways.

4.5.2 Defects

We also modeled the electrochemical reduction of two of the most common pyridinic defects found for graphene, tri-pyridinic (P3N, with up to three added H atoms) and tetra-pyridinic (P4N, with up to four added H atoms) vacancy defects.[145, 146, 147] A recent study reported pyrrolic defects to be suitable for CO_2 reduction into formic acid with a low overpotential, but we find that the formation energy of this type of defect is significantly more uphill in energy than the energies to form the P3N and P4N defect sites.[129] Since the defective structures already incorporate N atoms, we did not study doping of additional N atoms to these structures. In accordance with previous reports,[148] H atoms preferentially bind to the N atoms within the pyridinic vacancy sites within the plane of the nanocarbon sheet. The first H atom binds to an tetra-pyridinic N atom by 1.8 eV. H atoms will not bind to other C atoms in this system (binding energies range from –1.3 to –0.8 eV). When one H atom is already bound to an N atom, the same trend holds where the second H atom binds

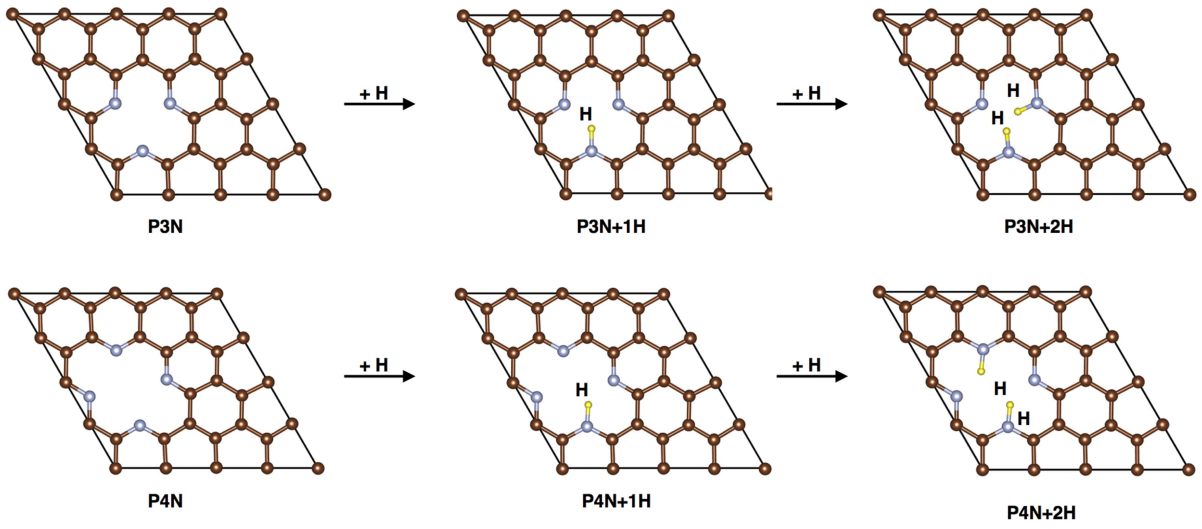

Figure 4.2: Basal plane structures with tri-pyridinic (P3N) and tetra-pyridinic (P4N) defects considered in this work showing different numbers of C (brown spheres), N (blue spheres), and H (yellow spheres) atoms. The $x \times y$ unit cell is denoted by the black lines. The z direction has a 20 Å vacuum region.

much stronger to another N atom (1.7 eV). However, the presence of one H atom will allow a second H atom to bind to other C atoms (binding energies range from 0.3 to 0.8 eV). The positive binding energies for the tri-pyridinic and tetra-pyridinic defects are due to N-doped defects, which possess electron lone pairs that can bind to protons and allow electrons to enter the π-system of the GBP.

4.5.3 Graphene ribbons

All data on GR systems were relaxed with spin polarization, where the starting magnetic moment on the system was 1 μB. The resulting spin moments for these systems always resulted in zero except for the GR saturated with H atoms, which had a magnetic moment of 1.3 μB. The presence of edge states in GR system makes their structural and electronic properties different from GBP systems.[149] These edge states can be expected to cause preferential doping of N and addition of H on the edges of the ribbons. Indeed, we observe

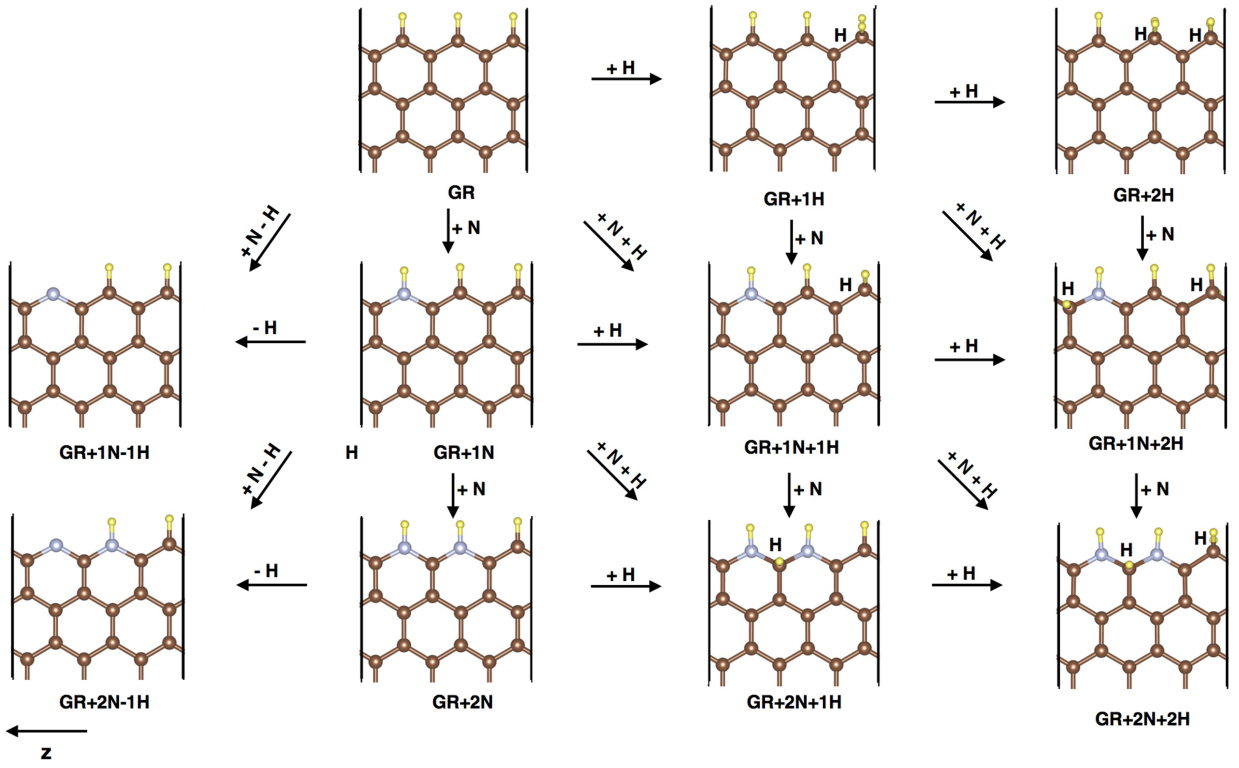

Figure 4.3: Nanoribbon structures considered in this work with different numbers of C (brown spheres), N (blue spheres), and H (yellow spheres) atoms. Only the top half of the symmetric ribbon is shown. The periodicity of the unit cell in the z direction is denoted by the dotted lines. H labels denote atoms on the top face of the nanoribbon. The x and y directions have 15 Å and 20 Å of vacuum separation their periodic images

the first and second H atoms bind to the edges of the ribbons in our symmetric GR model, and our data are in good agreement with previous studies.[150] Furthermore, when the GR model is doped with N atoms, these preferentially substitute with C atoms at the edges of the ribbons.[151] For N doping, the N atom substitution energies (per N atom added) are –0.7 eV, and 0.1 eV for the first and second N atoms respectively. After the first N substitution, removing an H atom is uphill by 1.2 eV. However, after the second N substitution, removing an H atom is energetically downhill -0.5 eV. Interestingly, when H atoms are added into the nitrogenated GR models, frustrated Lewis pairs form at the edges.

4.5.4 N_2 chemical potential vs. electrochemical potential phase diagrams

We now illustrate the electrochemical stability of the GBP systems in an N_2 environment using phase diagrams obtained with atomistic thermodynamics. The phase diagrams for the GBP system include the basal planes shown in Figure 4.1 and the defective sites in Figure 4.2. Data needed to reproduce these figures are given in the Appendix B. The free energies of these states were calculated as a function of the nitrogen concentration ($\Delta\mu_{N_2}$) and applied potential, E. We note that these phase diagrams represent theoretical thermodynamic stabilities of different structures, but in reality some structures may not be observed due to high kinetic barriers. Determination of these barriers in the presence of local solvation environments at electrochemical interfaces will be the subject of future work.

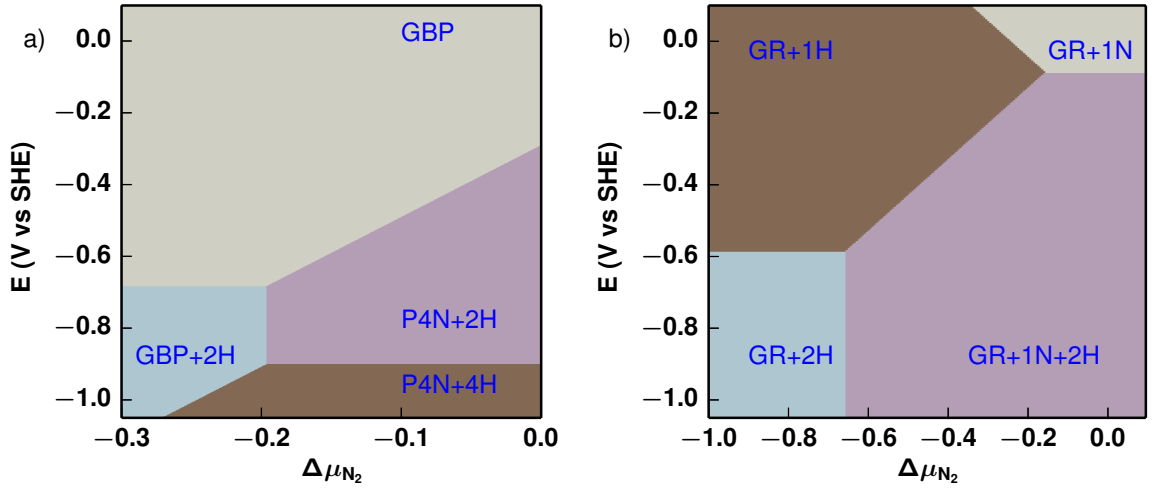

Figure 4.4: *ab initio* atomistic thermodynamics phase diagrams for graphene basal planes (GPB, left) and graphene ribbons (GR, right) under electrochemical environments with nitrogen.

We find that the pristine GBP system is generally stable across large ranges of nitrogen concentration and applied potential. However, when $\Delta\mu_{N_2}$ changes to reflect increased N content in tandem with more negative electrochemical potentials, structures involving the reduced forms of the P4N defective sites are thermodynamically more stable than the pristine

GBP system. More negative than $\Delta\mu_{N_2}$ = –0.18 eV, the most thermodynamically stable structure is either the reduced GBP structure with two H atoms or the P4N structure with four H atoms, depending on the values of $\Delta\mu_{N_2}$ and applied potential.

For the GR systems, N incorporation is energetically favorable when $\Delta\mu_{N_2}$ is more positive than –0.2 eV. At $\Delta\mu_{N_2}$ values more negative than –0.2 eV, a hydrogenated GR system is more stable. At slightly negative applied potentials, the thermodynamically most stable ribbon structure is the electrochemically reduced and nitrogenated GR system denoted as GR+1N+2H. Note that in this system, the two H atoms bind to sites at the ribbon edges that could be classified as frustrated Lewis pairs. At $\Delta\mu_{N_2}$ values more negative than –0.67 eV and at E values more negative than –0.6 V vs. SHE, the reduced GR+1H system incorporates another H atom to form the GR+2H system. These results show that while it is energetically easier to dope a GR with a N atom than doping a GBP, the GBP with P4N defective sites can accommodate more N atoms and presumably even more with the formation of graphene nitride compounds. We also observed that it is easier to reduce the ribbons at all ranges of $\Delta\mu_{N_2}$ when compared to basal planes. In summary, a potential of at least –0.3 V vs SHE is required to reduce a GBP system (into the P4N+2H system) while a less negative potential of –0.1 V is the lowest potential required to reduce the N doped GR systems.

4.5.5 Pourbaix diagrams

We have shown Pourbaix diagrams to be useful descriptors for identifying participating catalyst morphologies in CO_2 reduction.[131] When one Pourbaix diagram for a reactant (say, for CO_2) is superimposed on a Pourbaix diagram for a molecular or an extended structure catalyst, electrochemical conditions for low overpotentials are identified as the regions where boundaries from different Pourbaix diagrams are proximal to one another. We calculated Pourbaix diagrams for both graphene basal planes and graphene ribbons as a function of N concentration, and they are shown in Figure 4.5. The left and right panels show Pourbaix diagrams with increasing concentration of N in the GBP and GR models respectively. In the case of the GBP model with no nitrogen present (Figure 4.5 a), the GBP system is the

more stable structure until –0.7 V vs. SHE, at which point the thermodynamic driving force favors a $2H^+/2e^-$ reduction process. In contrast, basal planes containing pyridinic defects are much more susceptible to electroreduction. Here, the P3N defect and the P4N defect would readily undergo $1H^+/1e^-$ and a $2H^+/2e^-$ reductions, respectively, at 0 V vs SHE. The boundary lines in the Pourbaix diagrams of the GBP and P4N models are several volts more negative than the standard redox potential needed to form formate from carbonic acid (a stable form of CO_2 in aqueous solution), indicating that reductions of the catalyst here would bring significantly higher overpotentials if they were needed to drive CO_2 reduction. However, the boundary lines denoting the reduction of the P3N+1H state into the P3N+2H state is relatively close to the boundary line for carbonic acid or bicarbonate reduction into formic acid or formate, suggesting that these processes on these morphologies would have lower overpotentials if coupled to CO_2 reduction.

The Pourbaix diagrams for zigzag edges of GR systems are somewhat different from those for the GBP systems. In the case of the undoped GR system, we see boundary lines that are not well-suited for energetically efficient CO_2 reduction. However, the $2H^+/2e^-$ reductions involving the GR+1N state (the nanoribbon with 1/3 coverage of N) and GR+2N (the nanoribbon with 2/3 coverage of N) into the GR+1N+2H and GR+2N+2H states are quite closely aligned to be coupled to energetically efficient CO_2 reduction. This indicates that zigzag edges of N-doped nanocarbons are good candidates for efficient CO_2 reduction via H-shuttling mechanisms. Future work will focus on detailed reaction pathways for these processes. In principle, similar analyses as what has been reported here can be used to identify nanocarbon morphologies for energetically efficient catalysis.

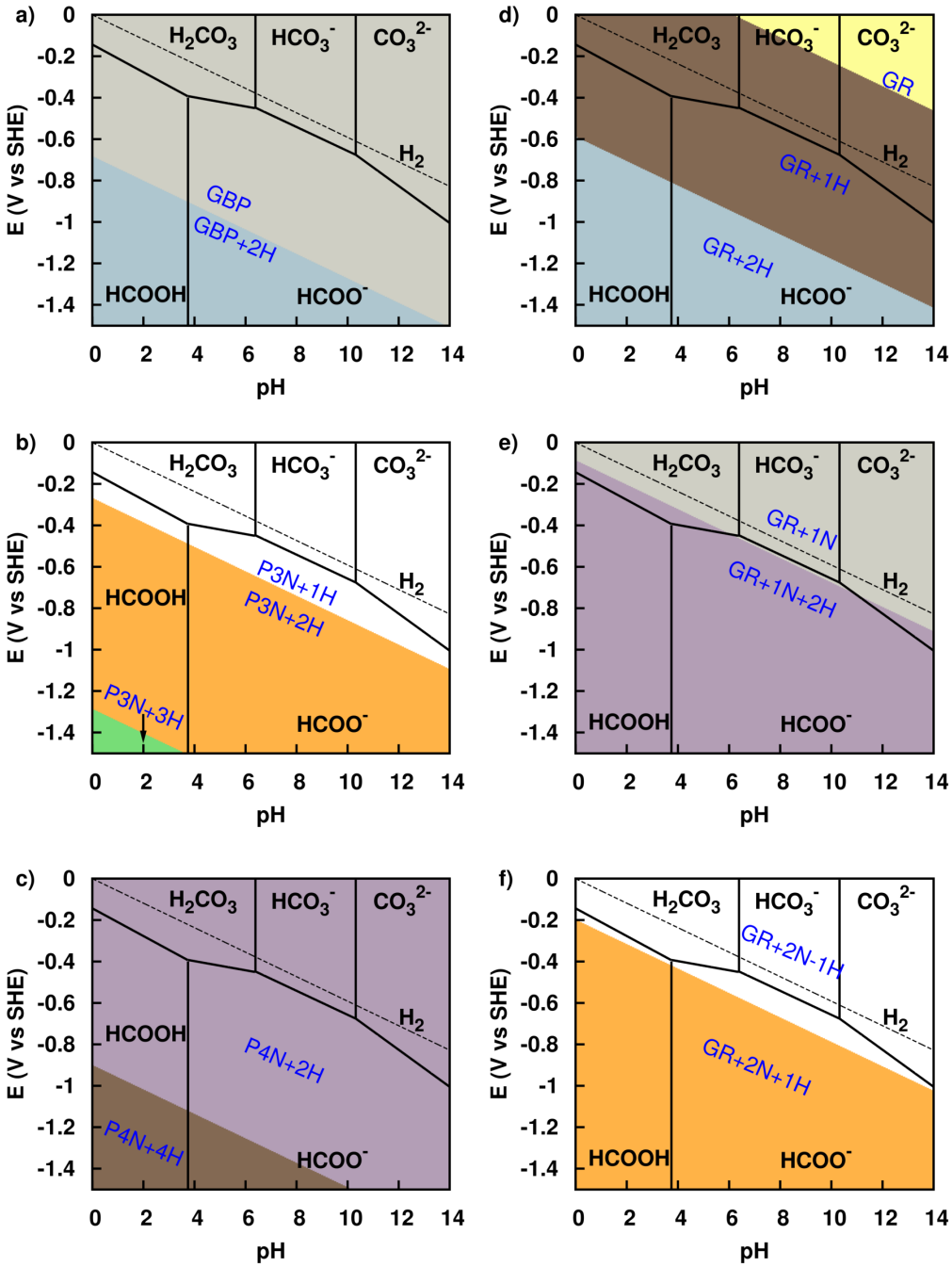

Figure 4.5: Pourbaix diagrams for basal plane structures (GBP (a)), tri-pyridinic defect (P3N (b)), tetra-pyridinic defect (P4N (c)) and graphene ribbon structures (GR (d), GR+1N (e), GR+2N (f)).

4.6 CONCLUSIONS

We have used density functional theory with atomistic thermodynamics to determine the energies of atomic scale N-doped nanocarbon morphologies under *in operando* electrochemical conditions. We find that zigzag edges are in general more susceptible to electrochemical reductions than graphene basal planes. However, tri-pyridinic defects have suitable thermodynamic energies to undergo $2H^+/2e^-$ reductions at electrochemical operating conditions with moderately negative applied potentials. Our results show that if nitrogen concentration of carbonous materials can be well controlled, the reduction potentials for the materials should be tunable for energetically efficient catalysis. Of particular interest are the reduced states of these materials that can form frustrated Lewis pairs that would be applicable for energetically efficient (de)hydrogenation catalysis. Calculating reaction barriers under electrochemical conditions and integrations with experiment will be a focus of future work.

5.0 COMPUTATIONAL INVESTIGATION OF CO_2 ELECTROREDUCTION ON TIN OXIDE AND PREDICTIONS OF DOPANTS FOR IMPROVED CATALYSIS

The content of this chapter is taken from Karthikeyan Saravanan, Yasemin Basdogan, James Dean, and John A. Keith. "Computational investigation of CO_2 electroreduction on tin oxide and predictions of Ti, V, Nb and Zr dopants for improved catalysis." *Journal of Materials Chemistry A*, 2017, 5(23), 11756-11763.

5.1 ABSTRACT

We have used computational quantum chemistry and atomistic thermodynamics to identify reaction intermediates for CO_2 electroreduction on partially reduced tin oxide electrodes. We find that a variety of different surface morphologies are thermodynamically accessible under reducing potentials with adsorbed CO_2, adsorbed H atoms, and O vacancy defects that represent partially reduced states. Our work supports prior conclusions from experimental findings that the active catalyst for this system is a hydroxylated and partially reduced SnO_2 surface that forms under operating conditions for CO_2 reduction. Employing thermodynamic descriptors and the computational hydrogen electrode model, we predict that doping Sn electrodes with Ti, V, Nb, or Zr will result in lower overpotentials for CO_2 reduction compared to undoped tin oxide.

5.2 INTRODUCTION

Sn electrodes have received attention for CO_2 reduction due to their relatively high catalytic activity, low cost and low toxicity.[152, 153, 154, 155] Importantly, Sn electrodes have a high overpotential for the hydrogen evolution reaction that make it suitable for selective CO_2 reduction. As with most non-noble metal electrodes, Sn electrodes exhibit degradation and corrosion. This normally deactivates non-noble metal electrodes,[156] but in the case of Sn, this is an asset since the oxide layer is catalytically active for CO_2 reduction. Kanan et al. have reported how CO_2 reduction efficiency depends on the presence of thin films of tin oxide, and removing naturally formed oxide layers decreases the catalytic efficiency.[153] Those authors suggested that formation of CO_2^- is a key electrochemical step and that SnO_x plays a key role stabilizing this intermediate.

Experiments on CO_2 reduction using tin oxide catalysts have shown that maintaining the oxidation state of Sn is difficult at highly cathodic operating conditions, and the reduction of tin oxide to Sn resulted in a decreased rate of formate production.[154, 155] Experiments by Bocarsly and coworkers presented spectroscopic evidence of a thinning of the native oxide layer at -1.4 V vs. Ag/AgCl.[152] They also showed that the thinning was reversible, and the thickness of the oxide layer can be controlled by applying an external potential. Under CO_2 reduction conditions, vibrational frequencies of 1100 cm^{-1}, 1385 cm^{-1} and 1500 cm^{-1} were observed, and these were attributed to a layer of carbonate (CO_3^{2-}) forming during the reaction rather than CO_2^- intermediates.

In contrast to recent experimental work, very few computational studies have investigated electrochemical CO_2 reduction mechanisms on tin oxide and provided predictions for new and improved catalysts. Ge and coworkers recently reported a computational study of reaction energetics and barrier heights for CO_2 reduction pathways on a Sn(211) surface with a single monolayer of Sn oxide as a model system.[156] Those authors discussed how hydroxyl groups can facilitate CO_2 reduction by forming bicarbonate species that eventually form CO. While this conclusion may in fact be true, previously mentioned XPS studies by Bocarsly have indicated that much more oxide is present in these reactions than a single monolayer.[152] Furthermore, the dominant product of CO_2 reduction on SnO_2 is formate and not CO.

The present study uses computational quantum chemistry modeling to better understand 1) what is the surface morphology of tin oxide under CO_2 reduction conditions, 2) what are the key reaction intermediates, and 3) how are the energetics of these intermediates influenced by modifying the electronic structure of the catalyst. To answer these questions we used atomistic thermodynamics and Kohn-Sham density functional theory (DFT) to predict the stability of various Sn oxide morphologies under different electrochemical operating conditions. As with previous studies in our group,[157, 158, 159, 160] we use Pourbaix diagrams to identify at what electrochemical conditions the catalyst would participate in proton and electron transfers. Unlike our previous studies, the present work focuses on the nature of the oxide surface under *in operando* conditions with different hydrogen coverages and concentrations of oxygen vacancy defects. After benchmarking our calculated data to available literature values, we predict elemental dopants not yet experimentally tested that should result in lower CO_2 reduction overpotentials.

5.3 COMPUTATIONAL METHODOLOGY

5.3.1 Models

This study makes use of *ab initio* atomistic thermodynamics,[135] the computational hydrogen electrode (CHE) model,[21] and Pourbaix diagrams to better understand the nature of the tin oxide catalyst under electrochemical operating conditions. This modeling study assumes that the approximate free energy of any reaction intermediate on a surface can be related to the energies of a reference slab structure and different adsorbates, the latter of which are treated as chemical potentials that are functions of experimental temperature and pressure. The free energy needed to form a generalized reaction intermediate (ΔG_{rxn}) follows:

$$\Delta G_{\text{rxn}} = G_{\text{int}} - G_{\text{slab}} - \sum N_i \times \mu_i \tag{5.1}$$

where G_{int} is a calculated absolute free energy of the intermediate state, G_{slab} is the calculated absolute free energy of a reference SnO_2 slab, and N_i and μ_i are the numbers and calculated

chemical potentials of molecular species (i.e. O vacancy defects, H atoms, and/or CO_2 molecules) that must be added or subtracted from the reference slab to create the generalized intermediate state.

CO_2 electroreduction on tin oxide electrodes will produce different products depending on pH, applied potential, composition of the electrode and electrolyte. The pH and applied potential were modeled using standard analytic expressions (see below). We note that modeling solvation effects on surfaces is not trivial since 1) continuum solvation models under periodic boundary conditions are not yet established to be quantitatively accurate[161, 162] and 2) water structures on rutile oxides are more complex than those found on fcc metal surfaces,[163] and studies using explicit water structures would likely need reactive dynamics.[164] In this study solvation effects for a few key intermediate states were modeled using the continuum solvation model VASPsol.[165] Our study has not accounted for co-adsorptions with ions from the electrolyte, which cannot yet be ruled out to play key roles in these mechanisms.

Electrochemical conditions that lead to CO_2 reduction can be expected to cause an accumulation of H atoms on an oxide surface which may result in H_2 evolution or the reduction of the surface oxide. The relevant reactions at the cathode are then:

$$SnO_2 + 2H^+ + 2e^- \rightarrow SnO_{2-\delta} + H_2O \tag{5.2}$$

$$2H^+ + 2e^- \rightarrow H_2 \tag{5.3}$$

$$CO_2 + 2H^+ + 2e^- \rightarrow HCOOH \text{ (or } CO + H_2O) \tag{5.4}$$

where 'δ' pertains to O vacancy defects formed in the stoichiometric SnO_2 slab (see below), and the standard redox potential for producing HCOOH via Eq. 6.4 is $E = -0.61$ V vs. the Standard Hydrogen Electrode (SHE) at pH 7. The CHE model approximates the chemical potential of a proton and an electron pair as one half of the chemical potential of a H_2 molecule, with linear corrections for the applied potential versus the SHE (eU_{SHE}) and the pH of the system:

$$\mu_{H^+} + \mu e^- = \frac{1}{2}\mu_{H_2} - eU_{\text{SHE}} - 0.059 \times \text{pH} \tag{5.5}$$

The chemical potentials of O vacancy defects and CO_2 are:

$$\mu_{O_{defect}} = \mu_{H_2O} - \mu_{H_2} + 2 \times eU_{SHE} + 2 \times 0.059 \times pH \tag{5.6}$$

$$\mu_{H_2O} = G_{H_2O} + \Delta\mu_{H_2O} \tag{5.7}$$

$$\mu_{CO_2} = G_{CO_2} + \Delta\mu_{CO_2} \tag{5.8}$$

Our complete reaction free energy expression accounting for pH and potential dependent reaction thermodynamics on a generalized $SnO_{2-\delta}$ surface is then:

$$\begin{aligned} \Delta G_{rxn} = G_{int} - G_{slab} - N_H \times \left(\frac{1}{2}\mu_{H_2} - eU_{SHE} - 0.059 \times pH\right) \\ -N_{CO_2} \times (G_{CO_2} + \Delta\mu_{CO_2}) \\ +N_{defect} \times (G_{H_2O} + \Delta\mu_{H_2O} - \mu_{H_2} + 2 \times eU_{SHE} + 2 \times 0.059 \times pH) \end{aligned} \tag{5.9}$$

Free energy terms in Eq. 5.9 were calculated as a sum of electronic energy calculated by DFT as well as zero-point energies and vibrational entropic contributions from the harmonic oscillator approximation. These vibrational energy contributions were obtained by partial Hessian calculations for only adsorbate atoms. For the energies of gaseous molecules, we use a similar approach but add corrections (i.e. +0.3 eV for CO_2 and +0.1 eV for H_2) that were suggested by Vegge and co-workers to account for free energy corrections as well as systematic errors in DFT calculations.[166] (See more discussion below.)

Table 5.1: Benchmarking comparison of data from CP2K calculations, VASP calculations and literature data.[a]

Quantity	**CP2K**		**VASP**	**Literature**
	Γ-point	k-point		
Bulk α-Sn cohesive energy / eV	3.2	3.2	3.2[167]	3.1[168]
Bulk α-Sn lattice constants (a=b=c) / Å	6.62	6.62	6.66	6.49 [169]
α-Sn (100) surface energy / meV/Å^2	58.69	59.72	55.50	55.50[170]
Bulk SnO_2 cohesive energy / eV	4.5	5.1	5.1	6.0[171]
Bulk SnO_2 lattice constants (a=b, c) / Å	4.81,3.23	4.79,3.22	4.83,3.24	4.74,3.19[172]
SnO_2 (110) surface energy / meV/Å^2	79.42	100.1	74.08	64.9[173]
SnO_2 (110) surface O vacancy formation energy[b] / eV	0.5	2.0	2.2	2.3[174]
Bulk SnO_2 standard reduction potential[c] / V vs SHE at pH 0	0.12	0.01	–0.03	–0.12[154]

[a] See ESI for technical calculation details for each data entry.

[b] Calculated as $SnO_2 \rightarrow SnO_{2-\delta} + \frac{1}{2}O_2$

[c] Calculated as $SnO_2 + 4H^+ + 4e^- \rightarrow \alpha\text{-Sn} + 2H_2O$.

5.3.2 Electronic structure calculations

To obtain phase diagrams, we modeled 58 different surface oxide structures representing different configurations of O vacancy defects and CO_2 and H adsorbates to find the lowest energy state according to Eq. 5.9. We used the computationally efficient CP2K code[175] for calculating electronic energies. We used the default double-ζ valence plus polarization (DZVP) basis set optimized according to the Mol-Opt method.[176] CP2K models electronic structure with a joint Gaussian and plane wave (GPW) formalism,[177] and the interaction of the valence electrons with frozen atomic cores is described by Goedecker−Teter−Hutter norm conserving, dual-space-type pseudopotentials.[178] A planewave expansion for the charge density is employed with an energy cutoff of 400 Ry. This energy cutoff was chosen after the cohesive energy of SnO_2 was converged to within 0.005 eV. The Perdew-Burke-Ernzerhof (PBE) functional[179] was used as the exchange correlation functional, and Grimme's "D3" dispersion corrections have been included.[180] All geometries were relaxed using k-point sampling unless otherwise noted (see below) using the Broyden–Fletcher–Goldfarb–Shanno (BFGS) minimization algorithm until the forces converged to 4.5×10^{-4} $E_h \cdot$ Bohr^{-1}.

Recent versions of CP2K (3.0 and later) are now implemented with k-point sampling for the Brillouin zone. This functionality allows CP2K to use smaller unit cells and be directly compared to other widely used codes that employ k-point sampling such as VASP.[181] Calculated energy data with k-point sampling generally appeared to be more accurate than data without; however, calculations with k-point sampling sometimes did not converge (see below). Specifically, geometry optimizations of 10 out of our 58 calculated slab geometries did not fully converge. In these cases, we used geometries optimized without k-point sampling (i.e. Γ-point calculations) and then carried out single energy calculations with k-point sampling on those geometries. The difference in relative energies of structures optimized with and without k-point sampling was less than 0.1 eV for almost all cases. When k-point sampling was used in partial Hessian calculations, many structures had multiple imaginary frequencies even though geometries were first optimized with k-point sampling. When k-point sampling was not used, only real frequencies were found for structures optimized without k-point sampling.

5.4 RESULTS AND DISCUSSION

5.4.1 CP2K Validation

To confirm that CP2K results would be suitable for predictions of electrocatalysis on SnO_2, we benchmarked data calculated from CP2K and VASP against available experimental data. Our VASP calculations used the same PBE functional but the projector augmented wave (PAW) method[182, 183] that we consider as being more accurate but more computationally expensive than the CP2K calculations. More computational details are found in the ESI. Table 1 shows that CP2K reasonably predicts cohesive energies, lattice constants, surface energies, and bulk standard reduction potentials (calculation details for each value is found in the ESI). We found Γ-point calculations problematic for calculations of standard reduction potentials and O vacancy formation energies. For other quantities Γ-point calculations were found to be reasonably accurate with our surface model. The only case where calculations using k-point sampling were less accurate than Γ-point calculations was surface energies. While CP2K surface energies appear somewhat problematic compared to VASP surface energies, our study uses the same surface model, and errors are expected to largely cancel when comparing relative energies from similar surfaces.

5.4.2 SnO_2 surface calculations

The lowest energy facet of rutile SnO_2 is the (110) surface, and as a first approximation we assume this is the most thermodynamically relevant facet under catalytic reaction conditions.[184] We modeled this surface using a symmetric 2×2 surface unit cell with a thickness of 4 layers (with the bottom two layers fixed to bulk atomic positions, Figure 5.1) to accommodate one and two O vacancy defects at the surface as well as adsorbate coverages as low as 1/4 ML. This surface contains four bridging oxygen atoms (O_{br}), four in-plane oxygen atoms (O_{ip}), and four under-coordinated Sn atoms (Sn_{5c}).

Our calculations of adsorbate binding energies and defect formation energies showed that the O_{br} sites were the preferred sites for binding CO_2 and H adsorbates as well as forming O vacancy defects. We modeled slabs with 0%, 25% and 50% surface O vacancy defect concen-

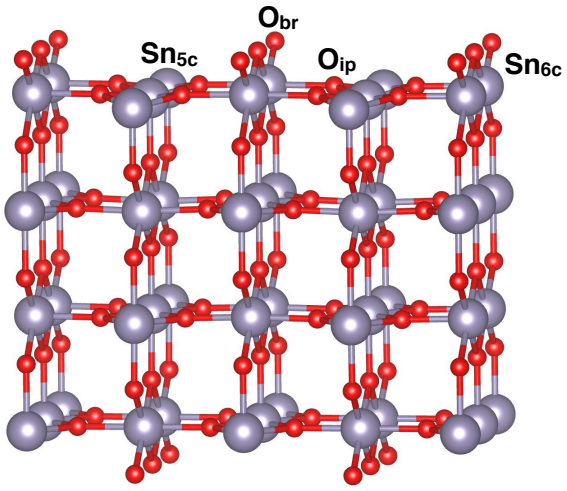

Figure 5.1: The (110) surface of rutile tin oxide with tin atoms marked in purple and oxygen atoms marked in red. Labels denote the catalytically active sites that were considered in this study. H and CO_2 adsorbates prefer binding to the O_{br} site.

trations to determine the sensitivity of energetics for an oxide that might become reduced under in operando conditions. By removing neutral O atoms from the cell and maintaining overall charge of zero, slabs containing O vacancy defects have Sn atoms in lower oxidation states. O_{br} atoms were removed from the top layer of the surface since these were found to be thermodynamically preferred. Our calculated vacancy formation energy to form 25% and 50% defects is 2.0 and 2.1 eV, respectively and agrees well with previous studies.[185, 174]

As stated above, we found that H atoms and CO_2 molecules preferentially bind to the O_{br} site (BE_H=1.5 eV, BE_{CO_2} = 0.4 eV). The next most energetically favorable site for H and CO_2 is the O_{ip} site (BE_H=-0.1 eV, BE_{CO_2} = 0.3 eV). In general, adsorbates were found to not bind to the Sn_{5c} sites on slabs with O atom vacancy defects. As expected, surfaces with O vacancy defects at the surface accommodated fewer H and CO_2 adsorbates.

All electronic energies for the slabs with and without O vacancy defects were calculated using Eq. 5.9. We selected configurations where intermediates had the strongest binding energy since these reflect the most stable intermediates present on a surface. From these

lowest energy states, we generated an electrochemical phase diagram (Figure 5.2a) that depicts the stability of different intermediate structures as a function of the chemical potential of water and the applied electrochemical potential. A change in μ_{H_2O} reflects a change in the thermodynamic potential required to create O vacancy defects from a SnO_2 surface and form water. Experimentally, this would be done by varying the partial pressure or the concentration/activity of water in the electrolyte.

We found that all surfaces irrespective of the O vacancy defect concentrations are OH-terminated across the range of applied potentials relevant for CO_2 reduction. This is in agreement with previous computational[156] and experimental studies.[152] Furthermore, partially reduced SnO_2 slabs with 25% O vacancy defects and OH-terminations are the most thermodynamically relevant structures at ambient operational conditions ($\mu_{H_2O} = 0$ and at negative potentials). Forming structures with two O vacancy defects (50% surface defects) requires reduction of a hydroxylated 25% defect slab into a hydroxylated 50% defect slab, and this was calculated to require a very negative potential (-2.3 V vs SHE at pH 0). This indicates that the actual tin oxide surface is partially reduced at these potentials despite the bulk standard redox potential being -0.53 V vs. SHE at pH 7. This is in agreement with previous experimental observations.[152, 155]

We then generated an electrochemical phase diagram (Figure 5.2b) showing the stability of different intermediates on a partially reduced SnO_2 structure as a function of $\Delta\mu_{CO_2}$ and potential. As mentioned in the Computational Details section, Vegge and co-workers reported systematic errors in catalytic reaction steps for CO_2 reduction, and they recommend corrections to the absolute free energy of CO_2.[166] After using these corrections, CO_2 was unbound by 0.33 eV, and it was unbound by even more when accounting for solvation energies using the VASPsol continuum solvation model (see Table S3). This contrasts to computational work by Liu and coworkers, whose calculations using continuum solvation strengthened CO_2 binding energies on rutile TiO_2 (110) by as much as 0.4 eV.[186] Ge and co-workers also reported that CO_2 binds only very weakly to their tin oxide model.[156]

Our reported phase diagrams account for interactions of H adsorbates, O vacancies, and CO_2 adsorbates (including the correction for CO_2 from Vegge et al).[166] Figure 5.2a is the phase diagram at a fixed $\mu_{CO_2} = 0$, while Figure 5.2b is the phase diagram at a fixed $\mu_{H_2O} =$

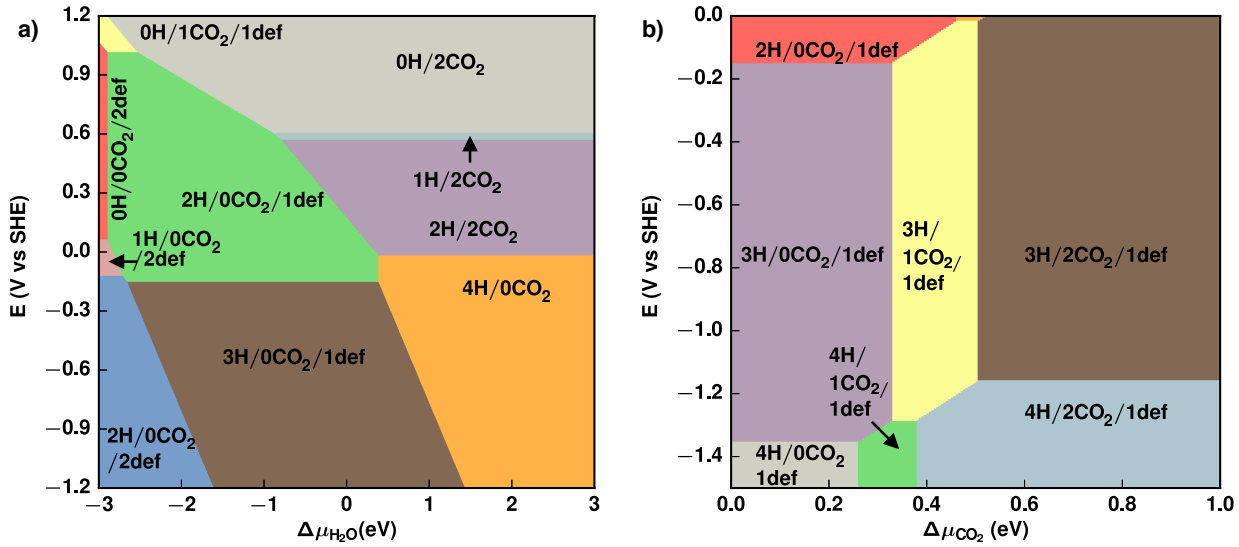

Figure 5.2: Electrochemical phase diagram representing the stability of different states as a function of chemical potential of a) water, μ_{H_2O} and b) CO_2, μ_{CO_2}, and applied potential at pH 10. $\Delta\mu_{H_2O}$ represents thermodynamic driving force needed to reduce a SnO_2 surface and $\Delta\mu_{CO_2}$ denotes the thermodynamic driving force needed to get CO_2 to bind to the surface within our model.

0. These figures provide a qualitative map for what surface structures are stable on the tin oxide surface under different electrochemical conditions. The most relevant surface structure at CO_2 reduction conditions (i.e. at $\Delta\mu_{H_2O} = 0$, $E \leq -0.3$ V and $\Delta\mu_{CO_2} = +0.33$ eV so that CO_2 is bound to the surface) has one O vacancy defect (at 25% surface concentration), one CO_2, and either three or four H adsorbates bound to the surface depending on the applied potential.

We then used Pourbaix diagrams to identify relevant surface compositions under electrochemical reaction conditions.[187, 188] Note that Pourbaix diagrams are thermodynamic constructs, and they do not account for kinetic barriers that regulate product formation. Nonetheless, our group has found that Pourbaix diagrams can be useful for identifying conditions where two or more reaction intermediates have the same chemical potential,[19] since this would identify a low overpotential process in terms of the Sabatier Principle. By super-

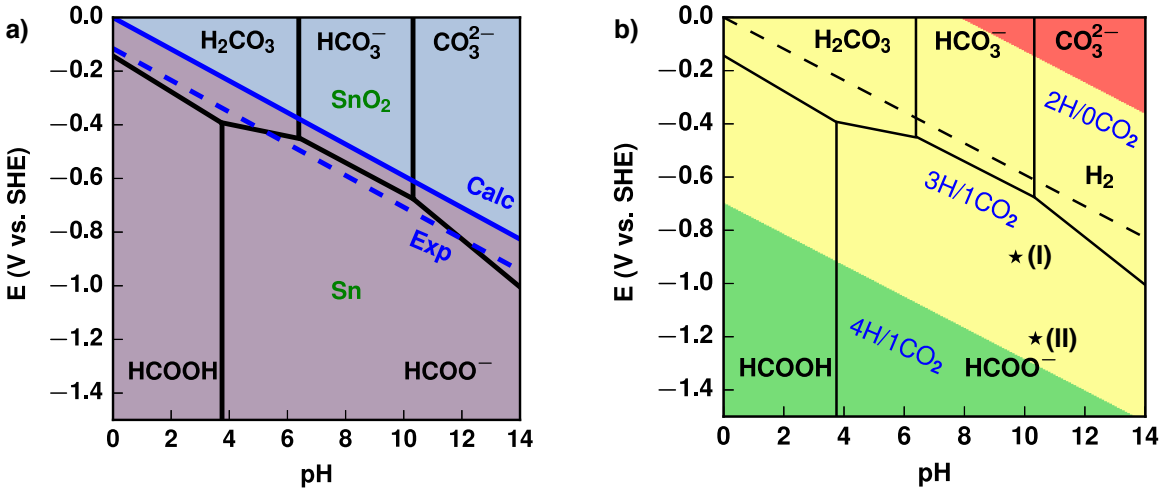

Figure 5.3: a) Experimental Pourbaix diagram of the Sn/SnO_2 redox couple (blue dotted line) overlaid on the Pourbaix diagram of CO_2 in solution (black solid lines). Our calculated bulk reduction potential (blue solid line separating colored regions) agrees well with the experimental bulk redox potential. b) Calculated Pourbaix diagram (colored regions) of a partially reduced SnO_2 slab with 25% defects overlaid on the Pourbaix diagram of CO_2 in solution (black solid lines). A value of $\Delta\mu_{CO_2} = +0.35$ eV was chosen so that CO_2 would be bound to the surface. The calculated redox potential between the $[\mathbf{3H/1CO_2}]$ and $[\mathbf{4H/1CO_2}]$ states is close to experimental potentials (denoted by solid stars) at which the maximum faradaic efficiency of CO_2 reduction to formate was experimentally observed. (I) -0.90 V vs. SHE at pH 9.7,[155] (II) -1.2 V vs. SHE at pH 10.2.[154]

imposing the Pourbaix diagrams of aqueous phase CO_2 reduction (involving bicarbonate and carbonate species) and a molecular or extended material catalyst, we have shown that the proximity of the boundaries between different Pourbaix diagrams identify electrochemical conditions that would be appropriate for electrocatalysis with low overpotentials.

Interestingly, Lee et al. have identified potential/pH conditions at which formate is produced with a high faradaic efficiency while maintaining the phase stability of SnO_2 nanocatalysts as given by the Pourbaix diagram for the bulk SnO_2.[154] Figure 5.3a shows our

calculated Pourbaix diagrams overlaid with the experimental Pourbaix diagram for CO_2 intermediates in aqueous phase. The calculated Pourbaix diagram for bulk SnO_2 is in reasonable agreement with experiment, but electrocatalysis will occur on surfaces rather than the bulk material. Figure 5.3b shows our calculated Pourbaix diagrams for our partially reduced SnO_2 surface model overlaid with the experimental Pourbaix diagrams for CO_2 reduction. Linear sweep voltammograms reported by Lee and co-workers[154] show the maximum faradaic currents for formate production occur at about -1.2 V vs. SHE at about pH 10. Broekmann et al. make a similar measurement in the same electrolyte and see maximum faradaic currents at -0.9 V vs. SHE.[155] At pH 10, the boundary of our calculated Pourbaix separating the partially reduced $[\mathbf{3H/1CO_2}]$ and $[\mathbf{4H/1CO_2}]$ states (i.e. intermediate states resulting in an H atom binding to CO_2 is at $E = -1.3$ V, which is in reasonable agreement with experiments by Lee, but less good agreement with data by Broekmann. At present we cannot state if this result is coincidental or not since we are presently not considering barrier heights, and it is unclear what the actual pH at these interfaces would be. Our key point is that our Pourbaix diagram analysis (Fig 5.3b) predicts that $[\mathbf{3H/1CO_2}]$ and $[\mathbf{4H/1CO_2}]$ would be key states for energetically efficient CO_2 reduction.

As stated in the introduction, experiments by Bocarsly et al. reported in situ spectroscopic evidence of species attributed as surface bound tin carbonates with peaks centered at 1100 cm^{-1}, 1385 cm^{-1} and 1500 cm^{-1}. These frequencies are not present in different $[\mathbf{3H/1CO_2}]$ states, but calculated frequencies on the $[\mathbf{4H/1CO_2}]$ states are in better agreement with experiment. Figure 5.4 shows the two lowest energy configurations calculated for the $[\mathbf{4H/1CO_2}]$ state, which would be a transiently formed intermediate during CO_2 reduction. Figure 5.4a shows a protonated carbonate species **1** that is bound via the O_{br} site, and Figure 5.4b shows a protonated CO_2^- species **2** that bridges between an O vacancy defect and an undercoordinated Sn site. **1** was lower in energy than **2** by 0.1 eV, and this energy difference remained the same when solvation was accounted for (Table S3). However, the calculated vibrational frequencies of **1** were 1032 cm^{-1}, 1224 cm^{-1} and 1375 cm^{-1}, while the calculated frequencies of **2** were 1128 cm^{-1}, 1280 cm^{-1} and 1566 cm^{-1}, where the last frequency corresponds to a C=O stretch parallel to the surface of the oxide. Although **2** was found to be higher in energy, the vibrational frequencies for this state agree somewhat

more with observed experiments. Note that our Pourbaix diagram analysis used **1** as the [**4H/1CO$_2$**] structure since this was the lowest energy structure (data that also agreed more with the experimentally observed potentials for CO_2 reduction).

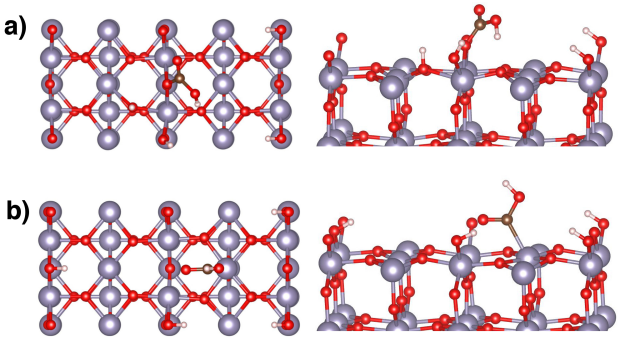

Figure 5.4: Top and side views of possible surface bound tin carbonate [**4H/1CO2**] states observed under reducing conditions (white atoms denote H, red atoms denote O, the brown atom denotes C, and purple atoms denote Sn). a) shows a CO2H species bound on an O_{br} site, b) shows a CO2H species bridging between an O vacancy defect and an undercoordinated tin atom.

5.5 DOPANTS

Our calculated data reported thus far provide a better conceptual understanding of relevant reaction intermediates. Having identified significant reaction intermediates that reasonably represent overpotentials for CO_2 reduction, we then considered how elemental doping would influence the relative energetics of these intermediates to predict dopants that would result in lower overpotentials. Following previous work by Carter et al.,[189] we inserted dopant atoms in place of Sn atoms nearest to adsorbate binding sites and then determined how that would affect the relative binding energies of the [**3H/1CO$_2$**] and [**4H/1CO$_2$**] structures on the 25% O vacancy defect surface. A volcano plot showing the calculated overpotential

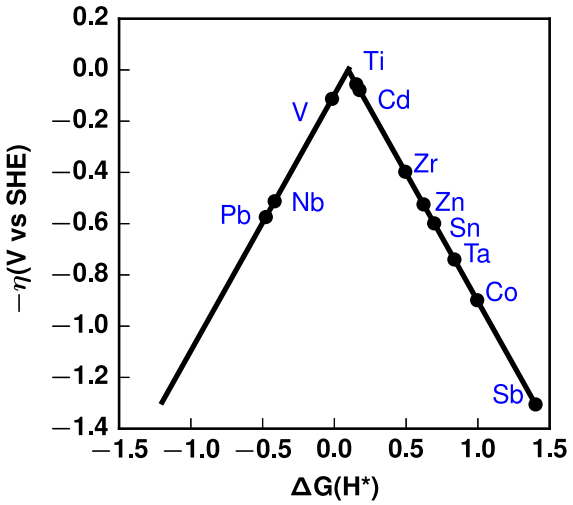

Figure 5.5: Volcano plot showing calculated overpotential of dopants at the experimental equilibrium potential (-0.79 V vs SHE) at pH 10.

of CO_2 versus the relative binding energy of the two states is shown in Figure 5.5. Our calculation procedure was as follows. We first identified the most stable site for a dopant atom to substitute with either a six-coordinate Sn atom at the surface or Sn atom next to an O vacancy defect. These sites were chosen because they are nearest to the adsorbates and thus would have the greatest effect on adsorbate binding energy. The dopant concentration was 3% with respect to the entire surface structure and 12.5% concentration with respect to the surface layer. We assume that dopant atoms remain bound at the surface layer and will not segregate. All doped slabs were geometrically relaxed to obtain binding energies.

Ti, V, Nb, Ta and Zr dopants were found to be most stable when in a six-coordinate site, and thus these dopants were identified as being in the 4+ oxidation state. Cd, Co, Pb, Sb and Zn were most stable next to an O vacancy defect and thus were nominally identified as being in a lower oxidation state (either 2+ or some form of mixed oxidation state). The effect of doping Ti, V, Zr, Nb, Cd, and Zn all resulted in an upward shift in the Pourbaix diagram boundary separating the [$\mathbf{3H/1CO_2}$] and [$\mathbf{4H/1CO_2}$] states. This

would mean these dopants should result in a lower overpotential than undoped tin oxide for CO_2 reduction. Indeed, alloys of Sn with Zn and Cd are already known to result in lower overpotentials for CO_2 reduction.[190, 191] Pb alloys are also known to experimentally result in lower overpotentials,[192] but our calculated results using Pb dopants show these would not significantly affect overpotentials for CO_2 reduction compared to Sn. Interestingly, we find that Ti, V and Zr have predicted overpotentials that are substantially less negative than overpotentials than for pure SnO_2. For this reason we propose that these dopants would be strong candidates for future experimental investigations on energetically efficient CO_2 reduction. We also find that Ta, Co, and Sb should be poorer dopants for CO_2 reduction. These computational predictions can also be experimentally verified.

5.6 CONCLUSIONS

We have carried out a first principles quantum chemistry investigation of CO_2 reduction on tin oxide electrodes. Using atomistic thermodynamics and the computational hydrogen electrode model, we find that the most likely surface composition is a partially reduced SnO_2 surface, which is in agreement with experimental observations. We also show a Pourbaix diagram model that appears to reasonably predict the experimentally observed potentials for maximum faradaic efficiencies for CO_2 reduction, and we discuss likely surface-bound intermediates that would account for the experimentally observed vibrational frequencies. With this model, we have also investigated dopants that would result in lower overpotentials for CO_2 reduction. Of the six dopants we predict to be improve electrocatalysis, two (Cd and Zn) have already been experimentally demonstrated as being effective, and four (Ti, V, Nb, and Zr) have yet to be experimentally confirmed. This study reports a computational model approach that can aid in the design of improved oxide electrocatalysts for CO_2 and other energetically efficient electrochemical processes for renewable energy.

6.0 ALCHEMICAL PREDICTIONS FOR COMPUTATIONAL CATALYSIS: POTENTIAL AND LIMITATIONS

The content of this chapter is taken from Karthikeyan Saravanan, John R. Kitchin, O. Anatole von Lilienfeld, and John A. Keith. "Alchemical Predictions for Computational Catalysis: Potential and Limitations." *The Journal of Physical Chemistry Letters*, 2017, 8(20), 5002-5007.

6.1 ABSTRACT

Kohn-Sham density functional theory (DFT) is the workhorse method for calculating adsorbate binding energies relevant for catalysis. Unfortunately, this method is too computationally expensive to methodically and broadly search through catalyst candidate space. Here, we assess the promise of computational alchemy, a perturbation theory approach that allows for predictions of binding energies thousands of times faster than DFT. We first benchmark the binding energy predictions of oxygen reduction reaction intermediates on alloys of Pt, Pd and Ni using alchemy against predictions from DFT. Far faster alchemical estimates yield binding energies within 0.1 eV of DFT values in many cases. We also identify distinct cases where alchemy performs significantly worse, indicating areas where modeling improvements are needed. Our results suggest that computational alchemy is a very promising tool that warrants further consideration for high throughput screening of heterogeneous catalysts.

6.2 INTRODUCTION

Advances in computational modeling and the need for better and less expensive catalysts has created the rapidly growing field of computational catalysis.[193, 194, 195]. Despite steady improvements in hardware and software, reliable quantum mechanics methods such as Kohn-Sham Density Functional Theory (DFT) remain too computationally expensive to efficiently divide and conquer through the massively large materials space of hypothetical alloys and their salient binding sites. The present study tests the promise of computational alchemy based on perturbation theory,[65, 66, 196] a method that, if sufficiently accurate, could be used to drive the computational screening of millions of hypothetical catalysts which would be prohibitive with DFT alone. We briefly summarize the computational alchemy method and then evaluate its accuracy in an *in silico* case study of adsorbate binding energies relevant to the oxygen reduction reaction (ORR).

Computational alchemy itself is not a new method. Its early applications have been used for biomolecular simulations,[58, 59] but variants based on electrostatic perturbations have more recently been used to predict properties of materials[71, 70, 197]. Such alchemy methods have been used to predict binding energies of molecular adsorbates on small nanoparticles and graphene,[72, 198] but it remains an open question if this approach would be useful for efficiently predicting binding energies of adsorbates on periodic metal surfaces that would serve as descriptors for identifying better (electro-)catalysts.[199, 200]

6.3 COMPUTATIONAL ALCHEMY METHODOLGY

A typical binding energy (BE) calculation scheme using DFT involves a self-consistent energy calculation on three different geometrically relaxed systems: a) the adsorbate at a particular coverage and binding site of a substrate (ads), b) the substrate without the adsorbate (slab), and c) the molecular absorbate alone (mol). The BE of the adsorbed state is calculated as,

$$\mathrm{BE} = E_{\mathrm{slab}} + n_{\mathrm{mol}} \times E_{\mathrm{mol}} - E_{\mathrm{ads}} \tag{6.1}$$

where n_{mol} is the number of adsorbed species on the surface that provides the adsorbate coverage. Note that BEs are a 0 K analogue to the negative of the heat of adsorption and thus always a positive value for a bound state.

Computational alchemy provides an efficient way to approximate the BE of an adsorbate on any hypothetical alloy surface as an energy difference to a reference BE. At best, alchemy will reproduce the same BE as the QM reference, the latter which may or may not adequately reflect an experimental result. These differences can be expressed in terms of electrostatic potential differences upon transmuting atoms from the reference slab into a hypothetical alloy. Mathematically, the transmutation can be carried out using a thermodynamic integration ($0 \leq \lambda \leq 1$) between the reference and other alloy candidate materials, and a Taylor expansion for the integration from the initial to the final states is [68, 201]

$$\Delta E|_{\lambda=1} = \Delta E|_{\lambda=0} + \partial_\lambda \Delta E^0 + \frac{1}{2}\partial_\lambda^2 \Delta E^0 + \dots \tag{6.2}$$

A practical way to use computational alchemy in computational catalysis screening applications is to set $\Delta E|_{\lambda=0}$ as the BE for a reference system (e.g. the BE for an adsorbate on a metal surface) and then solve for $\Delta E|_{\lambda=1}$ (i.e. the BE for the same adsorbate on an alloy slab) using only first order derivatives $\partial_\lambda \Delta E^0$. One can simplify this further when 1) the geometry of a hypothetical alloy slab is minimally changed from the reference slab (i.e. when atoms in the alloy slab have the same coordinates as the reference slab) and 2) the alloy can be obtained by net isoelectronic transmutations of atoms (see below). In this case the first order partial derivative is simply the alchemical derivative, often considered a reasonable starting approximation,[198, 71] and the derivative of the energy with respect to a variation in the nuclear charge distribution in the system, Eq. 6.3.

$$\partial_\lambda \Delta E^0 = \sum_I \Delta\mu_{nI} \partial_\lambda N_I \tag{6.3}$$

In the alchemical derivative expressed in Eq. 6.3, $\partial_\lambda N_I$ is the difference in nuclear charge with respect to λ, while $\Delta\mu_{nI}$ is the alchemical potential difference evaluated for each atom I at two different structures. Generally, this is R_I^a and R_I^b, but in BE approximations, it one can use $\mathrm{R}_I^{\text{ads}}$ and $\mathrm{R}_I^{\text{slab}}$ (Eq. 6.4).

$$\Delta\mu_{nI} = \mu_n^b(\mathrm{R}_I^b) - \mu_n^a(\mathrm{R}_I^a) = \mu_n^{\text{ads}}(\mathrm{R}_I^{\text{ads}}) - \mu_n^{\text{slab}}(\mathrm{R}_I^{\text{slab}}) \tag{6.4}$$

The alchemical potentials used in Eq. 6.4 correspond to the electrostatic potentials printed out at the end of a geometry optimization run in the widely used VASP program with default settings.[136] Finally, the alchemical potential difference, $\Delta\mu_{nI}$, is an array of the differences between the electrostatic potentials of the reference systems in the E_{slab} and E_{ads} calculations. Combining the approximations above, we can then rewrite Eq. 6.2 as Eq. 7.1 to express approximate binding energies using alchemy. A concise summary of how BEs from alchemy are calculated using VASP is shown in Scheme 1.

$$\text{BE}_{\text{alloy}} - \text{BE}_{\text{ref}} \approx \partial_\lambda \Delta E^0 = \Delta\text{BE}_{\text{alc}} \tag{6.5}$$

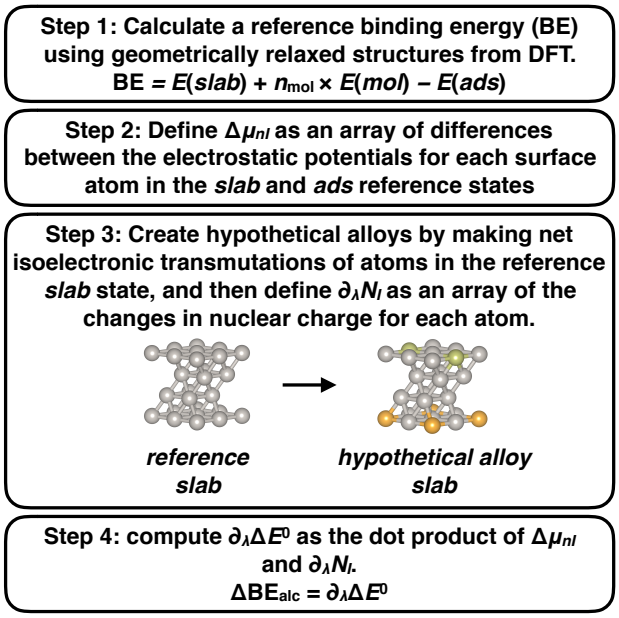

Figure 6.1: Steps involved in calculating BEs from Alchemy.

Eq. 7.1 defines the central assumption of our electrostatics-based alchemy in our study: a linear change in the electrostatic potentials between a reference state and any hypothetical alloy (having the same geometric coordinates as the reference slab) will be approximated as the difference in adsorbate BEs between the reference and the hypothetical alloy (see below). Note that the BEs approximated here are for chemisorbed species, but in principle alchemy can be used to approximate different forms of non-covalent binding[67, 201] by

virtue of the Hellman-Feynman theorem.[202] Since the density enters the first order perturbation estimate, and since van der Waals energies are relative, these results are not too surprising. Furthermore, we stress that this work defines errors with respect to BEs that would be obtained from a specific QM reference (here, data using the PBE exchange correlation functional,[138] and not experiment). While this may not always reflect actual BEs observed from experiment, we note that it has been shown that alchemy predictions using a higher-level reference such as hybrid-DFT can agree more with experimental data.[197]

Before discussing more details of the alchemy calculations, we briefly compare and contrast alchemy to two other models used to quickly estimate an adsorbate's BE relative to a chemically similar adsorbate's BE (e.g. O* vs. OH* or CH* vs. CH_2*) at the same binding site: scaling relationship methods[203] and the d-band model[97]. Establishing scaling relationships requires calculating a large enough number of DFT data points to give a linear relationship between the two different adsorbates across a variety of different materials. In contrast, computational alchemy can predict the BE of any adsorbate on any hypothetical alloy with only three DFT calculations for E_{slab}, E_{ads}, and E_{mol}, all needed to determine BE_{ref}. Post-processing the electrostatic output from these calculations with basic arithmetic can be scripted to rapidly determine $\partial_\lambda \Delta E^0$ and therefore a hypothetical BE_{alloy}.

Likewise, the d-band model correlates BEs to the energy levels of projected d-states of the complete electronic structure, and when shifts in d-band centers between a reference and hypothetical alloys are known, binding energies can be approximated. In contrast, we use alchemy to correlate BEs to changes in electrostatic potentials that reflect each system's complete electronic structure. In this way, we do not require knowing energy level shifts at all since we take advantage of a straightforward and easy approximation for how electrostatic potentials are affected within different isoelectronic transmutations (see below). Alchemy and the d-band model are relatable, but a direct and formal comparison of alchemy with the d-band model would be possible if one used alchemical derivatives to predict the projected states from electronic structures, and that is out of the scope of the present work.

The isoelectronic transmutations used here by definition result in a zero net change in the atomic number of a slab ($\sum_{n=1}^{\text{no. of atoms}} \Delta Z = 0$). For example, an isoelectronic transmutation of a reference slab containing 16 Pt atoms could be chosen to result in a new alloy slab with

14 Pt atoms, one Ir atom ($\Delta Z = -1$), and one Au atom ($\Delta Z = +1$). This would reflect one pair of Pt atoms being isoelectronically transmuted by $|\Delta Z| = 1$, but in general atoms could be transmuted with $|\Delta Z| = > 1$ and/or more pairs of atoms could be transmuted to estimate BEs on more hypothetical alloys.

6.4 COMPUTATIONAL METHODS

All electronic structure calculations in this study were performed with DFT using PBE[138] as the exchange-correlation functional and projector augmented wave pseudopotentials as implemented in VASP.[136] All systems except for the Pt_3Ni skin alloy and hypothetical alloys based on that structure were modeled using non spin polarized DFT calculations. An energy cutoff of 350 eV and $8 \times 8 \times 1$ k points were universally used for all the calculations. E_{slab}, E_{ads}, and E_{mol} structures for BE_{ref} were relaxed using conjugate gradient iterative minimization until the difference in energies between consecutive geometry steps was less than 1 meV. E_{slab}, E_{ads}, and E_{mol} structures for BE_{alloy} were calculated using single point DFT calculations.

6.5 RESULTS AND DISCUSSION

Our BE calculations use an fcc (111) surface model consisting of four layers. Transmutations are considered in two different classes of hypothetical alloys. The first class is a surface alloy, where atoms on the top layer of a metal (Pt, Pd, or Ni) surface are transmuted by $\Delta Z = \pm 1$. Transmutations at the bottom layer of the slab were found to be screened by the second and third layers of the slab and do not contribute significantly to the alchemical derivatives that perturb BEs. Thus, isoelectronicity in the surface alloy models is maintained by transmuting an atom in the top layer by $\Delta Z = \pm 1$ and transmuting an atom in the bottom layer by $\Delta Z = \mp 1$. The second class is a M_3Ni skin alloy (with M = Pt or Pd, and 50% of the atoms in the second layer are Ni). Isoelectronicity in surface alloys is maintained by transmuting

these Ni atoms by $\Delta Z = -6, -5, -4, -3, -2, -1, +1, \text{or} +2$ and transmuting corresponding atoms in the bottom layer by different amounts. These alloys correspond to M_3X skin alloys where X are atoms spanning the first row of the d-block.

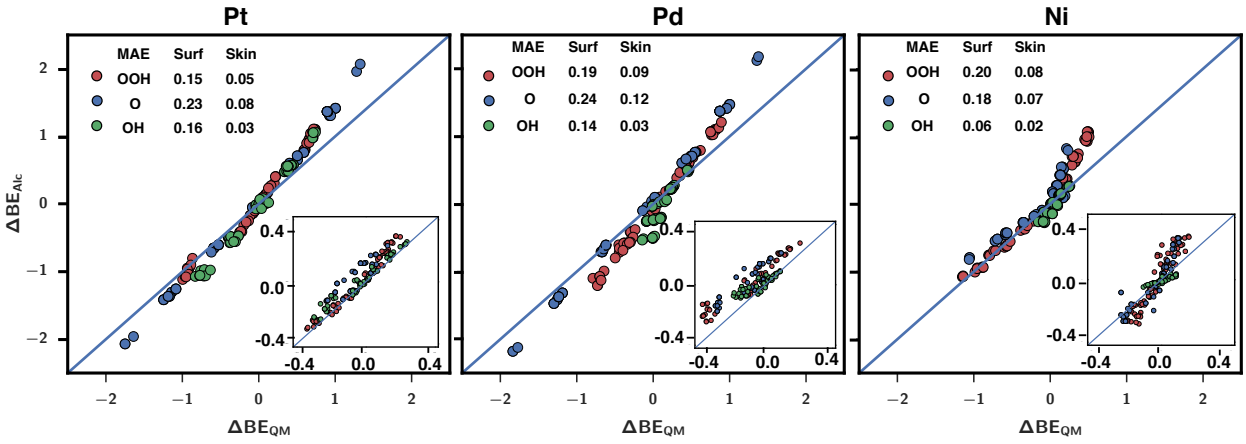

Figure 6.2: Parity plots (in eV) comparing the accuracy of OOH*, O*, and OH* BEs from alchemy on hypothetical alloys based on three different reference slabs: Pt(111) (left), Pd(111) (middle), and Ni(111) (right). $\Delta\text{BE}_{\text{alc}}$ is the alchemical change between the reference and hypothetical alloy and is equal to $\partial_\lambda \Delta E^0$ in Eq. 6.3 and $\Delta\text{BE}_{\text{QM}}$ is equal to $\text{BE}_{\text{alloy}} - \text{BE}_{\text{ref}}$ and calculated directly using DFT. Figures depict data for surface alloys (surf), and insets depict data for skin alloys. The alloys were obtained by changing different number of surface and skin atoms $|\Delta Z| = 1$. Mean absolute errors (MAE) are given in eV.

We stress again that all alchemical predictions of BEs for a given adsorbate and reference slab require merely three QM optimizations for the ads, slab, and mol states. The computational overhead for any number of alchemy predictions on any hypothetical alloy (based on the same adsorbate bound to an alloy based on the same reference slab) is negligible. Using our scheme employed for benchmarking, up to 28 different hypothetical alloys can be formed using a 2×2 surface unit cell with up to three transmutations of $|\Delta Z| = 1$ at the top layer. Using alchemy, BEs for these 28 hypothetical alloys would be obtained with the computational cost of one single BE from QM. Combinatorially and theoretically speaking, one could use computational alchemy to generate BEs for *more than 2.6 million hypothetical*

alloys using a 3×3 surface unit cell with up to 18 transmutations to different *d*-block elements from the same row as the host metal atoms in two top layers of the slab. Determining all BEs for these alloys would only cost three QM geometry optimizations, but the accuracy of alchemy needs first to be assessed.

To determine the accuracy of alchemy, we benchmarked the BEs for O*, OH*, and OOH* intermediates on randomly selected hypothetical surface alloys relative to DFT single-point binding energies, see Figure 7.3). Note that there are 360 data points in Figure 7.3. These data points were obtained by carrying out 15 full geometry optimizations with QM (for three different molecules, three different slabs, and $3 \times 3 = 9$ adsorbate-slab structures). To obtain QM data shown on the x-axes of Figure 7.3, an additional 705 single point QM calculations were required (for the remaining slab and adsorbate-slab structures) while the alchemy data on the y-axis was obtained solving basic arithmetic using Python scripts and was effectively instantaneous.

The lowest energy binding sites for O*, OH*, and OOH* intermediates on the reference metal slabs were the fcc, bridge and fcc sites respectively. The hypothetical alloys considered had different numbers of pairs of transmuting atoms and thus represented different alloy compositions in surface and skin alloys, always with atom transmutations of $|\Delta Z| = 1$. Overall, alchemy quite reasonably predicts BEs for all adsorbates on surface and skin alloys with mean absolute errors of 0.06 – 0.24 eV for surface alloys and 0.02 – 0.12 eV for skin alloys. The errors are significantly smaller on skin alloys because alchemical transmutations at an adsorption site in the top layer of a surface alloy generally results in larger errors than alchemical transmutations in a subsurface layer of a skin alloy. This can also be seen from the electrostatic potential maps that are included in the supporting information, where alchemical derivatives on surface atoms are much larger than for subsurface atoms.

We then focused on the sensitivity of alchemy errors at varying concentration of transmuting atoms (Figure 7.4). Errors in BEs calculated by alchemy systematically increase as the number of transmuted atoms increases. As seen before however, overall errors are much smaller for BEs on skin alloys when compared to surface alloys because alchemy errors are highest when the transmuted atom is directly at an adsorbate binding site.

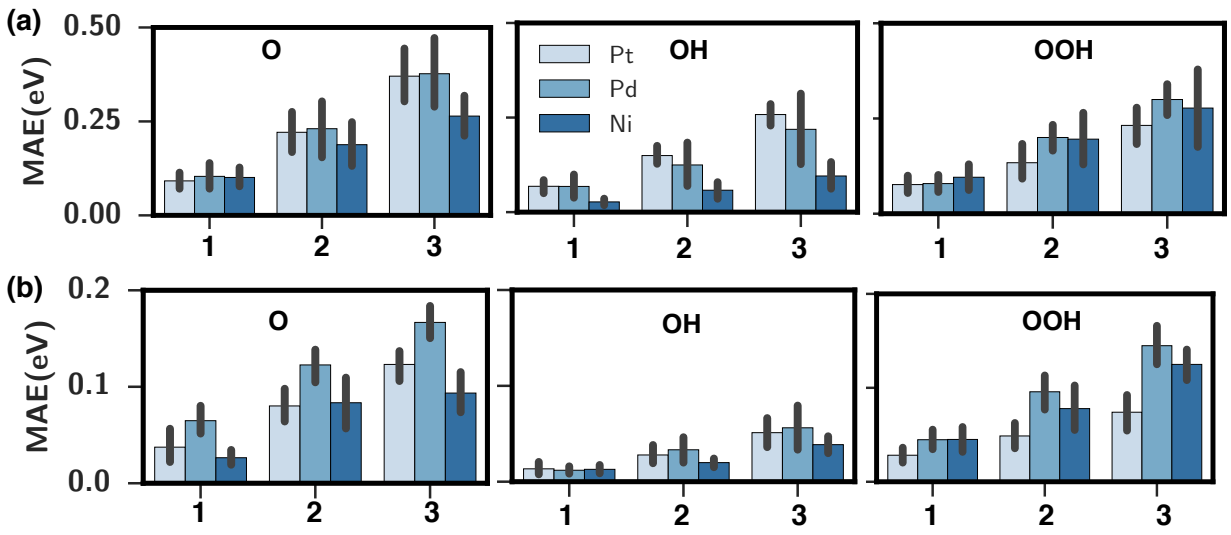

Figure 6.3: Mean absolute errors in BE of the different ORR intermediates on alloys with different number of pairs of transmuting atoms on the top layer in surface alloys (a) and subsurface layer in skin alloys (b). Lines in each bar denote minimum and maximum errors.

Predictions from alchemy also strongly depend on the specific site where atoms are transmuted relative to where the adsorbate is bound. There are significant alchemical gradients seen on atoms at the adsorption site due to the chemical bonding interactions (atoms with red and blue gradients in the electrostatic potential maps shown in Figure S1). Figure 6.4 shows the mean absolute errors for BEs from alchemy based on which atoms are transmuted. Errors are largest (0.1 eV or more) when atoms are transmuted at sites 2, 3 or 4 under the O* intermediate or in skin alloys when site 6 is transmuted. Sites 2, 3 and 4 on a surface alloy correspond to the sites where maximum negative alchemical gradients are observed on a surface alloy, and they comprise the 3-fold fcc site on which O* is adsorbed. Site 6 in skin alloys is especially sensitive because this site is found directly below the 3-fold site. Similarly, when OH* binds to a 2-fold bridge site on Pt, large alchemical gradients are seen on sites 3 and 4 and transmutations on these atoms results in larger errors (0.1 eV) compared to sites 1 and 2 (0.04 eV).

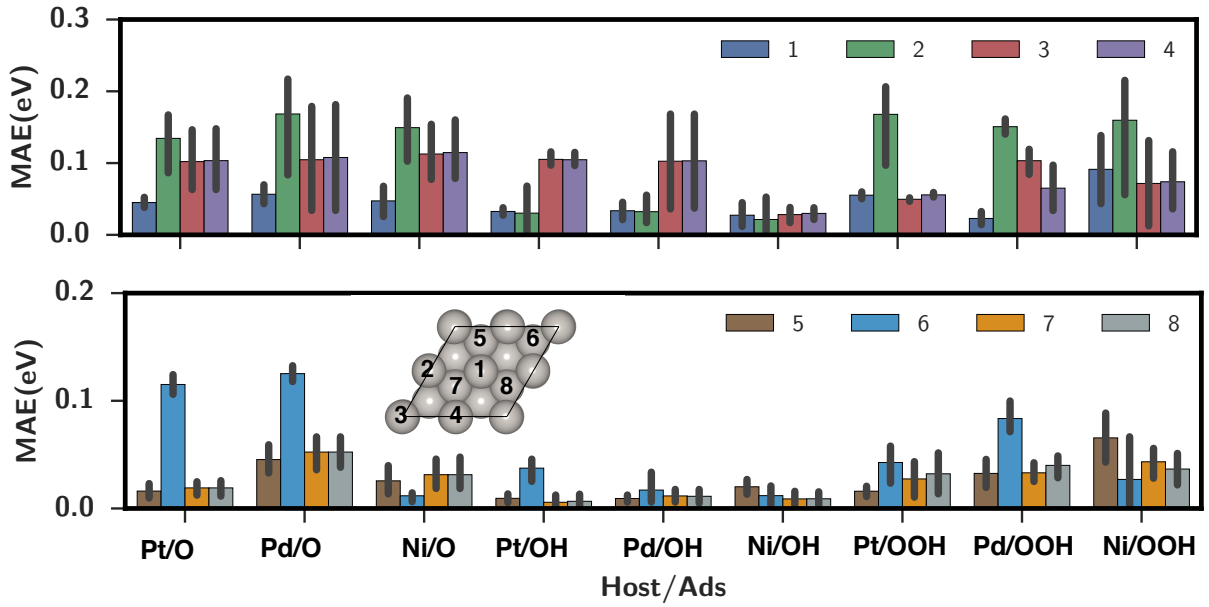

Figure 6.4: Mean absolute errors in BE associated with sites at which host atoms are transmuted. Lines in each bar denote minimum and maximum errors. Lowest binding energy sites for O*, OH* and OOH* to the different host metals are fcc, bridge and fcc sites, respectively.

Finally, we test the accuracy of alchemy when transmutations involve large changes in $|\Delta Z|$ are made on a M_3Ni skin alloy with the second layer containing 50% concentration of Ni atoms. For example, the M_3Ti alloy is obtained when both Ni atoms are transmuted to Ti corresponding to a $\Delta Z = -6$ per atom. To balance nuclear charge, we made various different transmutions to the bottom layer including $\Delta Z = +6$ on two atoms, or $\Delta Z = +4$ on three atoms, or $\Delta Z = +3$ on four atoms. Figure 6.5 shows the superset of alchemy errors for Pt_3X and Pd_3X. Interestingly, alchemy predicts BEs of O* and OH* in quite reasonable agreement with DFT on most M_3X alloys with errors less than 0.2 eV with the exception of transmutations resulting in M_3Mn, M_3Fe and M_3Zn alloys. Errors between alchemy and DFT are generally higher (>0.2 eV) for the BE of OOH across all M_3X alloys.

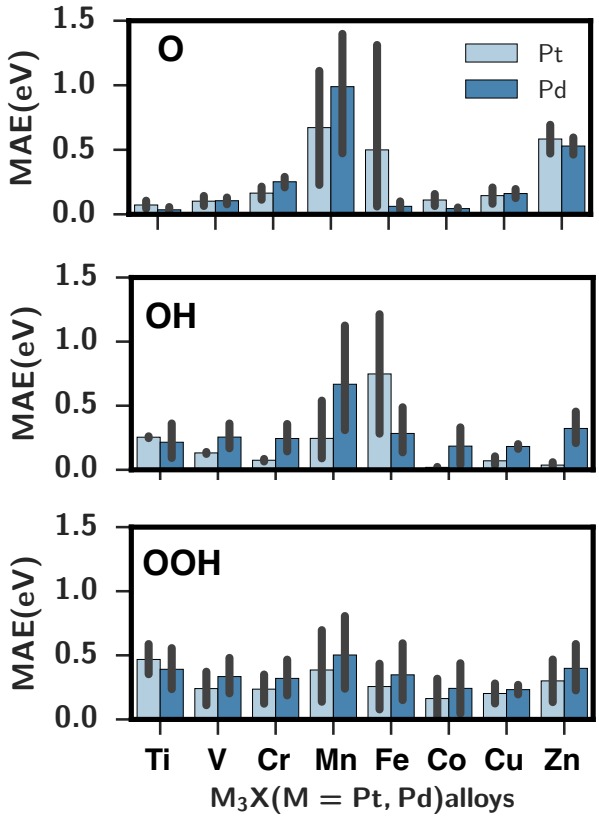

Figure 6.5: Mean absolute errors in BE associated with sites at which host atoms are changed to solute atoms

The largest errors in alloys containing Fe and Mn appear to be related to spin polarization in these slabs while errors in Zn alloys are more likely because Zn is not a transition metal. We note that these shortcomings of alchemy may be related to known shortcomings of the d-band model,[204] but again, a rigorous investigation of how these are related is out of the scope of the present work. At present, it indicates that high throughput screening with alchemy may need to address searches across different spin manifolds.

6.6 CONCLUSION

In conclusion, we have investigated the promise of first order alchemical estimates as a means to rapidly screen material catalysts. With minimal DFT calculations (i.e. those needed for a single binding energy of an adsorbate), alchemy can often predict BEs on hypothetical alloys within 0.1 eV of DFT energies with a few notable exceptions. For surface alloys involving transmutations of $|\Delta Z| = 1$, errors are largest when atoms are transmuted at the adsorbate site because this is where alchemical gradients are highest. For skin alloys when $|\Delta Z| > 1$, alchemy has significant problems predicting BEs when the alloying component is Mn, Fe and Zn. In future work we will give more details about different adsorbates, surface facets, and practical ways to overcome alchemy errors to the QM reference to make this method more reliable for computational screening of catalysts thousands of times more efficiently than with DFT calculations.

7.0 IMPROVING BE PREDICTIONS OF ALCHEMY USING MACHINE LEARNING

7.1 INTRODUCTION

In the previous chapter, we introduced Alchemy as a rapid means to calculating binding energies of adsorbates on hypothetical alloy catalysts. We first benchmarked the performance of Alchemy in calculating the binding energies of OH_x intermediates on the most thermodynamically stable facet of Pt, (111). We considered alloys that were obtained by changing atoms on both the surface and sub surface to Ir or Au. We found that Alchemy can be used to calculate BEs of most surface alloys within 0.1 eV except BE with the largest errors were predicted for alloys where atoms were changed close to the binding site. Interestingly, Alchemy predicted the BE of subsurface alloys with the least errors.

This chapter addresses the following questions. What are the limits of Alchemy performance? What regions of chemical catalyst space does Alchemy work well? What are the weaknesses of Alchemy and when can Alchemy not reliably used? What to do when Alchemy fails? In order to answer these questions, performance of Alchemy is validated for BE predictions of a wide range of intermediates relevant on hypothetical alloys of Platinum in different surface terminations. We considered alloys of varying concentrations of dopant beyond Ir/Au ($|\Delta Z|$=1) elements. We then identified cases where Alchemy failed in predicting BEs and proposed methods to address the errors between Alchemy and DFT.

7.2 EXTENSIVE VALIDATION OF ALCHEMY

In Section 6.3, BE of an alloy was approximated as the sum of BE of the reference state calculated by DFT and a first-order correction calculated by Alchemy.

$$\mathrm{BE}_{\mathrm{alloy}} = \mathrm{BE}_{\mathrm{ref}} + \Delta\mathrm{BE}_{\mathrm{alc}} \tag{7.1}$$

$$\mathrm{BE}_{\mathrm{alc}} = \partial_{\lambda}\Delta E^{0} \tag{7.2}$$

In order to extensively benchmark the performance of Alchemy, we considered several reference calculations. We chose a Pt host metal in (111), (100), (211) surface terminations for the slab calculations and nine different adsorbates, OH_x (O, OH, OH_2, OOH), NH_x (N, NH, NH_2, NH_3) and CH_x (C, CH, CH_2, CH_3) on each of those slabs for adsorbate calculations. Additional slab and adsorbate geometry relaxations were run with various surface unit cell sizes for each of the slabs and adsorbates to account for adsorbate coverage effects. All of these reference calculations let us access a larger chemical space of alloy catalysts. We enumerated a wide range of alloys by changing the number of atoms pairs that were transmuted (N_T = 1-4) and varying the dopant elements corresponding to $|\Delta Z|$ = 1(Pt→ Ir/Au) or $|\Delta Z|$ = 2(Pt→ Os/Hg) or $|\Delta Z|$ = 3(Pt→ Re/Tl).

7.2.1 Surface facets

In our prior chapter, we studied how Alchemy compares to DFT in predicting BEs of all coverages of OH_x intermediates on just a single facet (111) of different host metals Pt, Pd and Ni. In this chapter, we calculate BEs of all the intermediates on various surface terminations of just Pt. Different surface facets contain sites with varying catalytic activities due to their different coordination numbers and local environment. We first report parity plots comparing OH_x BE predictions by Alchemy on alloys of Pt: (111), (100) and (211) facets in Figure 7.1. Overall, BEs predicted by Alchemy are comparable to BE calculated by DFT for alloys in all surface terminations. Interestingly, MAE is lower for BE on alloys with a 211 termination(0.1 eV) and (100) termination (0.2 eV) when compared to (111) alloys(0.4 eV). This can be attributed to smaller alchemical gradients in (211) and (100) surfaces when compared to larger gradients on (111) surfaces.

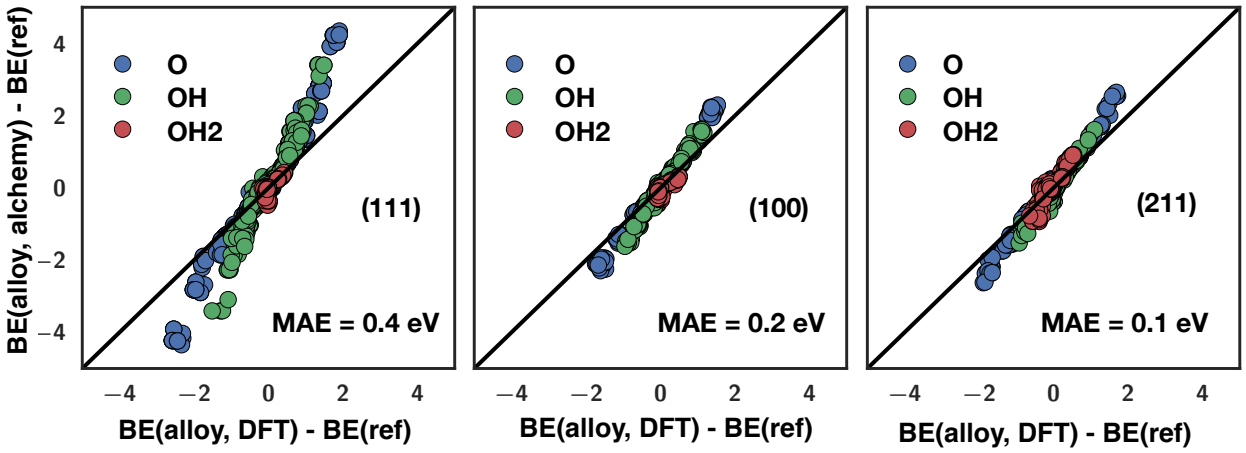

Figure 7.1: Parity plots comparing BE of all coverages of OH_x on Pt alloys (111), (100) and (211) calculated using Alchemy and DFT. Each data point is an alloy obtained by changing N_T = 1, 2, 3 and 4 number of Pt atoms to either Ir/Au($|\Delta Z|$=+/-1) or Os/Hg($|\Delta Z|$=+/-2) or Re/Tl($|\Delta Z|$=+/-3) on the top layer of the reference slab.

7.2.2 Adsorbate Coverage

A traditional approach in computational catalysis to account for varying concentrations of reactant species is to model a surface with different number of adsorbate molecules. In the context of DFT calculations, adsorbate coverage is expressed as a monolayer and is expressed as the ration of the number of adsorbate molecules to the number of atoms on the surface layer. In our previous study, we looked at a 1/4 ML of OH_x intermediates on a Pt surface. We extended our analysis to 1/3 ML, 1/4 ML and 1/9 ML coverages of OH_x intermediates on Pt surface (Figure 7.2). We find that errors from Alchemy increases as coverage increases due to large alchemical gradients set up by a higher concentration of adsorbates. When the adsorbate coverage increases, the number of molecules per surface atom increases resulting in large alchemical derivatives on sites close to the adsorbate. When these sites are transmuted, Alchemy predicts BEs that deviate with larger errors when compared to DFT.

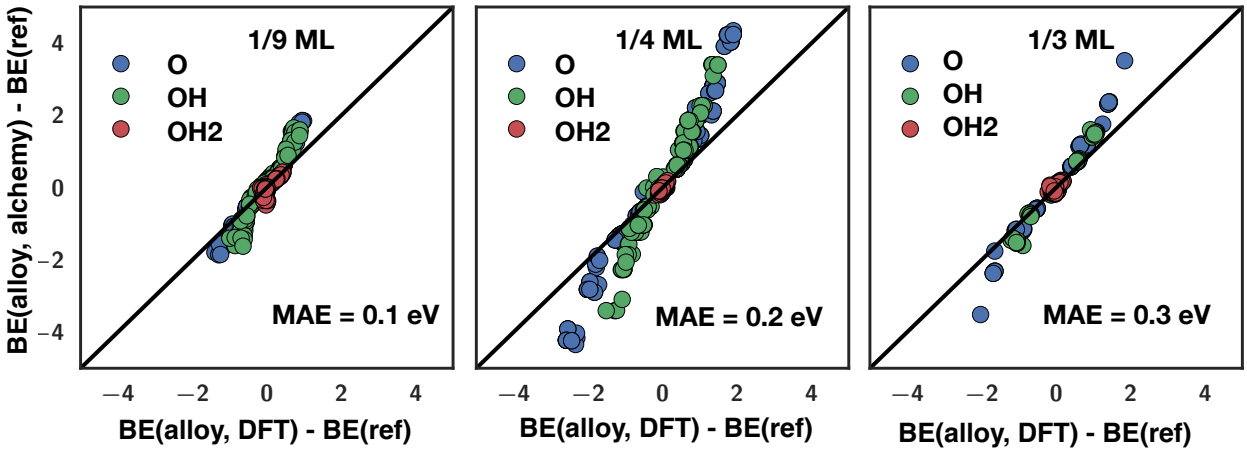

Figure 7.2: Parity plots comparing BE of adsorbates of OH_x on Pt alloys (111) calculated using Alchemy and DFT. Each data point is an alloy obtained by changing $N_T = 1$, 2, 3 and 4 number of Pt atoms to either Ir/Au($|\Delta Z|$=+/-1) or Os/Hg($|\Delta Z|$=+/-2) or Re/Tl($|\Delta Z|$=+/-3) on the top layer of the reference slab.

7.2.3 Adsorbates

Finally, we tested performance of Alchemy on the BE of all NH_x, CH_x, OH_x (x=0-4) adsorbates on an exhaustive set of alloys of Pt (111) surface. As mentioned above, these alloys were obtained by enumeration based on the number of atoms that were transmuted(N_T) and varying magnitude of atomic number change($|\Delta Z|$). In total, BE predictions for nearly 5500 such alloys are included. Figure 7.3 shows the parity plots grouped according to the central atom. We find that character of binding energy errors between Alchemy and DFT change based on the central atom in the adsorbates. The errors appear linear for OH_x BEs, non linear for CH_x and NH_x BEs. However, the character of binding energy error does not change for different levels of hydrogenations. These trends are attributed to the binding nature of the central atom of these adsorbates to the surface.

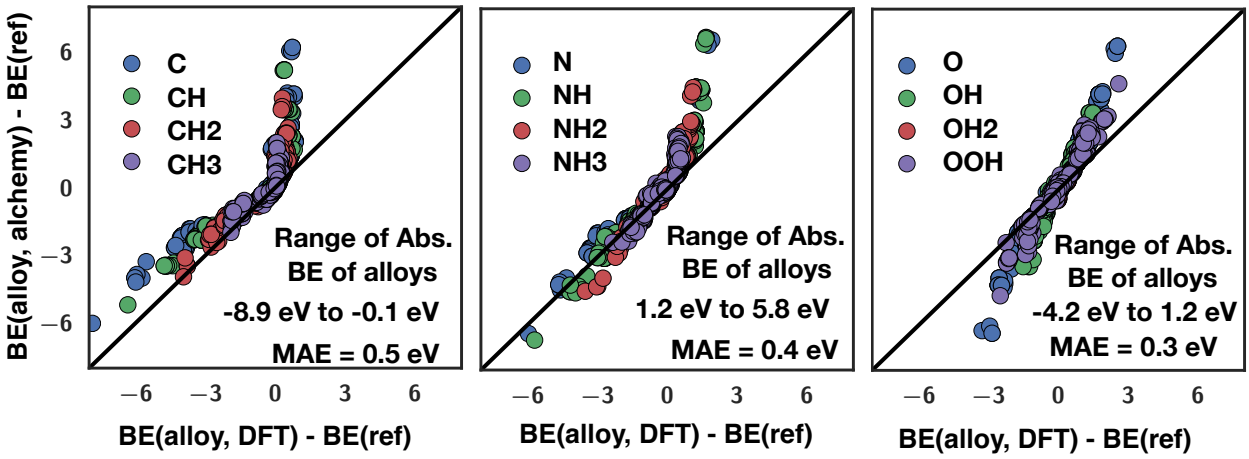

Figure 7.3: Parity plots comparing BE of adsorbates (NH_x, CH_x, OH_x) on Pt alloys (111) calculated using Alchemy and DFT. Each data point is an alloy obtained by changing N_T = 1, 2, 3 and 4 number of Pt atoms to Ir/Au($|\Delta Z|$=+/-1) or Os/Hg($|\Delta Z|$=+/-2) or Re/Tl($|\Delta Z|$=+/-3) on the top layer of the reference slab.

7.3 BREAKING DOWN THE SOURCE OF ERRORS

We further analyzed the errors from the above parity plot in order to identify cases where Alchemy breaks. The errors in BE of all adsorbates were bucketed into a group of categories based on N_T, $|\Delta Z|$ and adsorbate coverage. At very low coverages (1/9 ML), the MAE of predictions is always less than 0.1 eV for $|\Delta Z| = 1$ alloys regardless of the type of adsorbate. Interestingly, the errors are still lower than 0.1 eV even when all surface atoms are transmuted to $|\Delta Z| = 1$ dopants. At moderate coverages (1/4 and 1/3 ML), Alchemy predicts BE of alloys with small N_T and $|\Delta Z|$ with less errors when compared to alloys with large N_T and $|\Delta Z|$. The largest errors are seen for alloys when all surface atoms are changed to a maximum $|\Delta Z|$ (=3). The trends in BE errors can be explained as follows, the alchemical correction to the reference BE is based on a linear change in the electrostatic potential.

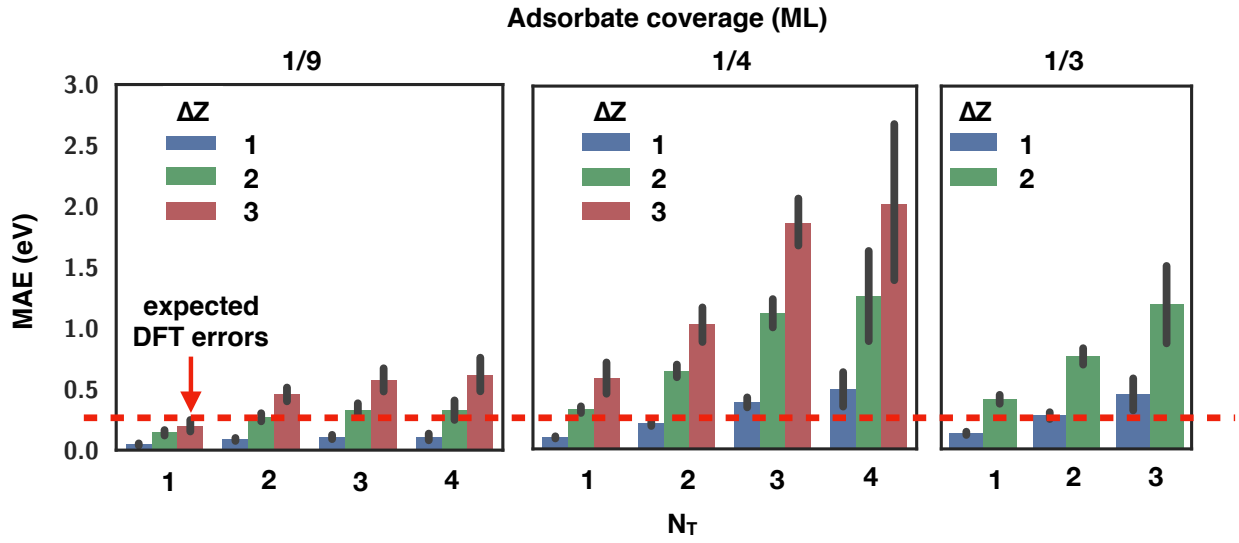

Figure 7.4: Error analysis plots

Changing N_T and $|\Delta Z|$ implies a large linear shift of the alchemical derivatives while the DFT BE shows that BE does not change much when compared to the reference BE. As explained in the previous section, we here see that MAE increases with adsorbate coverage where the errors are the least for 1/9 ML of adsorbate coverage and the largest for 1/3 ML coverage. Note that errors need to be compared by looking at similar $|\Delta Z|$ and N_T values.

7.4 IMPROVED ALCHEMICAL PREDICTIONS USING MACHINE LEARNING

In Figure 7.3, we see that BE predicted by Alchemy for some alloys deviate from the parity line. We also observed systematic trends in BE errors for different adsorbates and identified where these errors come from in our detailed error analysis plot. We hypothesize that errors will be systematic, and therefore straightforwardly addressed by machine learning to predict the errors and improve the BE predictions from Alchemy. Machine learning uses statistical

techniques to learn from the data provided and make useful predictions on unseen data. Here, we use a dataset of all alloy surfaces to build machine learning models that predict the errors. Our high-level workflow in calculating improvised BEs using Machine learning and Alchemy is shown in Figure 7.5.

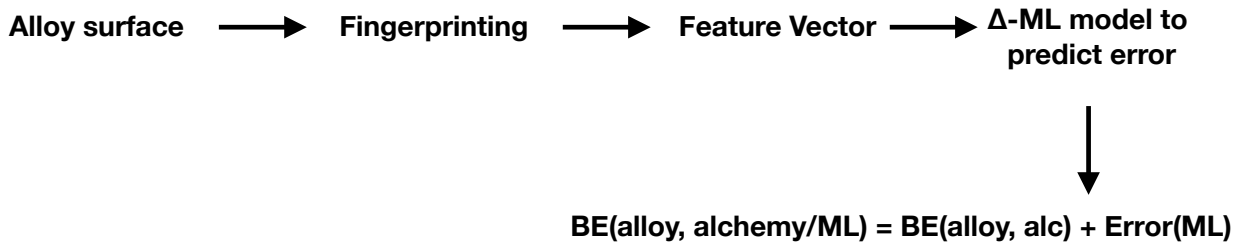

Figure 7.5: Machine learning workflow to obtain BE corrections to Alchemy

7.4.1 Machine learning in Catalysis

Before discussing more about how we use Machine learning for improving BE predictions, we list prior research in this area. Applications of ML in chemistry range from small molecule chemistry to materials science to protein behavior.[205, 206, 207, 208, 209, 210, 211] A few relevant examples in materials informatics include formation energies predictions [212, 207], accelerated screenings within individual bimetallics, accelerated nudged elastic band studies of reaction kinetic using neural networks and study of disorder on intermetallic configurations. Along these lines, ML models have also been developed to predict properties of catalysts.[213, 214, 215]. A combined machine learning and descriptor-based kinetic analysis framework can rapidly screen bimetallic catalysts for CO_2 reduction.[213] The input features for this model included the size of an atom, electronegativity and density among a few others.[214] A fully automated screening method based on ML and optimization techniques helped screen through larger chemical space of intermetallic catalysts. [215] Using this workflow, alloys of 31 different elements were screened and 131 candidate surfaces across 54 alloys were identified for CO_2 reduction and 258 surfaces were screened across 102 alloys for H_2 evolution.

7.4.2 Feature representation

Identifying relevant features are important for Machine learning models to correctly learn the underlying patterns in data. Features are variables that provide more information about the population in our dataset. To build models in our study, we choose the variables that we have identified in our prior error analysis since they strongly correlate with the BE errors. N_T, $|\Delta Z|$, adsorbate coverage, type of adsorbate, active dopant (atom that was changed on top layer) were included in the model building process. However, none of these features describe the alloy structures. We needed a better feature representation to encode how the atoms are configured in different alloys.

To address this, we developed a fingerprint representation that captures the chemical structure of alloy surfaces. First, we consider a vector whose length is the number of atoms per surface layer and elements of the vector representing sites on the surface layer of the alloy. Each element in the vector is binary indicating if atom at that site was changed or not. However, the length of the vector varies because different surface unit cells are included in our dataset to account for varying coverage effects. In order to normalize the feature vector, we set the length of the vector to the number of atoms on per surface layer of the largest surface unit cell (9 atoms in the case of Pt(111) 3 x 3 unit cell) and encode the elements accordingly. This is explained in Figure 7.6 where two atoms changed on the 2x2 surface unit cell are indicated by 1 on the vector while 3 atoms changed on 3 x 3 surface unit cells are changed to 1 at their respective sites. This fingerprint vector along with the active dopant feature describes alloy composition of the surface.

7.4.3 Model training and evaluation

Our dataset comprises all surface alloys that were enumerated for our prior benchmarking studies along with the DFT and Alchemy calculated binding energies of all intermediates on each of those alloys. For each BE on a surface alloy, the feature vector was obtained using the fingerprinting method described above and the error between the BEs was calculated. There were two types of variables in the feature vector: continous and categorical. Values of continuous variables are in a range of values while categorical variables have distinct values.

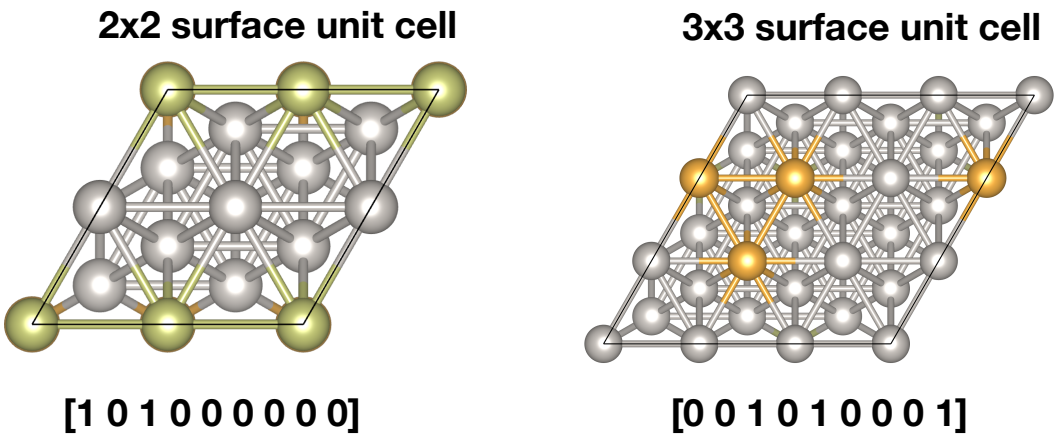

Figure 7.6: Fingerprinting

We then trained machine learning models to learn the data and then predicted the BE errors(target variable) for each surface alloy.

When building a model, it would not be meaningful to train and make predictions on the same data. The model would always perform pretty well when predictions are made on the data on which it was already trained upon. Our overall goal is to choose models with the least prediction errors on unseen data. In order to achieve this, we split the dataset into 80% training data and 20% test dataset. We first train our models on the training data and then make predictions on the test data. Mean absolute error was chosen as the performance metric to score each model.

$$\mathrm{MAE}_{\mathrm{test}} = \frac{1}{n}\sum_{i=1}^{n}(y_i - f(x_i)) \tag{7.3}$$

A common problem in machine learning is underfitting and overfitting. Underfitting is when the model performs poorly on both the training and test data. To avoid underfitting, the modeling procedure need to be changed or other fingerprinting methods need to be developed. A model is said to be overfit when the learning algorithm fits too close to the training data that it impacts the performance of the model on new data. One of the ways to avoid overfitting is to use a resampling technique like k-fold cross validation(CV). In k-fold

CV, the training set is split into k smaller datasets. Each of these smaller datasets serves as a test set once, while the remaining splits are used for training. For each of the k-folds, a model is trained using $k-1$ folds of training data and the resulting model is validated on the remaining part of the data using MAE. The performance of the model as measured by k-fold CV is the average of the all MAE values from the method.

7.4.4 Model Selection

We considered few different machine learning regression algorithms to predict an error correction to BE from Alchemy. We chose linear regression (with L1/L2 regularization), tree based models (random forests, gradient boosted trees) and support vector machines as candidate models. We identified promising models by measuring the performance from a 10-fold CV on the training data. We then optimized the hyperparameters for promising models using a 10-fold CV on the training data. The set of parameters that resulted in the best performance of the model were selected. Once the hyperparameters are selected, the model is trained on all data in the training set. This model is then applied to the test data to make predictions. The predicted error corrections are added to Alchemy calculated BE (last step in Figure 7.5), and then MAE between BE from DFT and BE from ML-corrected Alchemy are reported below. Note that the test data are not used in model selection and training.

7.4.5 Results

Using the methods described in previous sections, the best learning algorithms were trained and identified to predict BE corrections of intermediates on the alloy catalysts. We trained models individually on CH_x, NH_x and OH_x datasets and benchmarked BE predictions from ML-corrected Alchemy with BE calculated from DFT. Support vector machine with default hyperparameters was found to be the model with the least prediction errors on the test dataset. Figure 7.7 shows the parity plot comparing BE from ML-corrected Alchemy on just the alloys in the test dataset and their respective DFT calculated BEs. We see that predicted BEs are comparable to DFT calculated BE of all intermediates. The MAE of BE predictions of CH_x intermediates was 0.5 eV, with ML-corrections the MAE has dropped to 0.07 eV.

Similary, the MAE of BE predictions of NH_x on alloys reduced from 0.4 eV to 0.08 eV and OH_x went down from 0.3 eV to 0.1 eV. The machine learning model learns the non-linear relationships in the data and predicts the corrections to BE calculated by Alchemy.

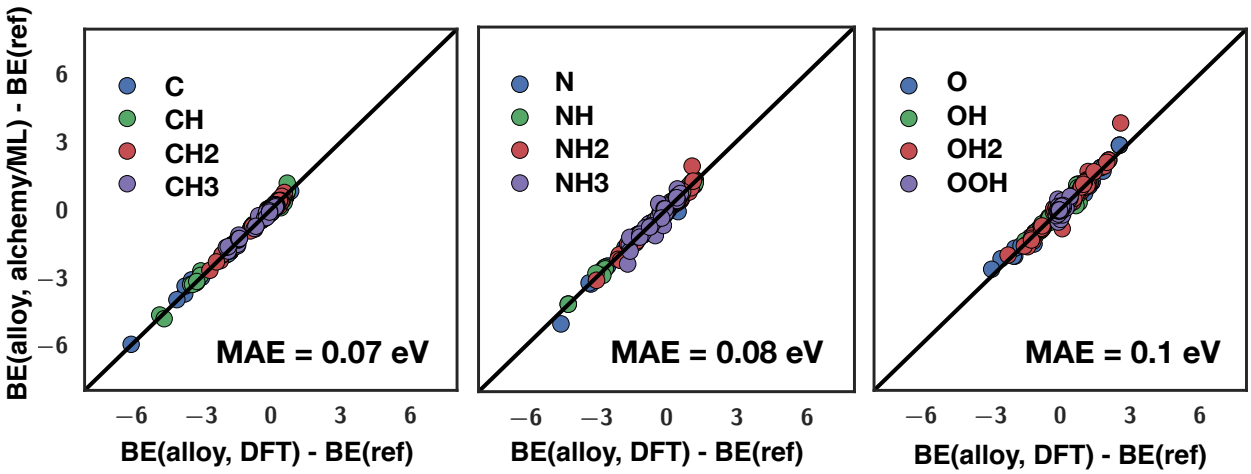

Figure 7.7: Parity plots comparing BE of adsorbates (CH_x, NH_x, OH_x) on Pt alloys (111) calculated using ML corrected Alchemy and DFT-SP. Each data point is an alloy obtained by changing NT number of Pt atoms to Ir/Au(Z=+/-1), Os/Hg(Z=+/-2), Re/Tl(Z=+/-3) on the top layer of the reference slab.

Finally, we used a statistic scoring method to identify the importance of the different variables in predicting the BE corrections and plotted a feature importance plot (Figure 7.8. Errors in BE mainly depend on magnitude of $|\Delta Z|$ followed by the number of atom pairs that were transmuted N_T as it was expected. Both of these terms are indicative of how big an alchemical change is performed to obtain a new alloy. When $|\Delta Z|$ and N_T are large, a large linear change in alchemical derivatives results in large errors. The other variables that are predictive of BE errors are adsorbate coverage, the type of binding site and the type of adsorbate.

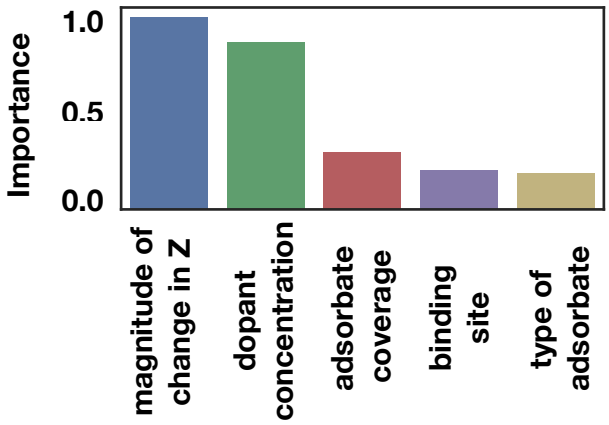

Figure 7.8: Feature importance plot

7.5 CONCLUSION

We have validated the performance of Alchemy on an extensive set of alloys that were enumerated by changing the number of transmuted atom pairs, the magnitude $|\Delta Z|$ of dopant atoms and the concentration of the adsorbate. Overall, Alchemy predicts BE comparable to DFT for a range of adsorbates on alloys of different surface terminations. Errors in BE prediction increases with increasing concentration of dopant atoms and large $|\Delta Z|$ values. The largest errors in BE (3 eV) from Alchemy were found for alloys obtained by changing 4 atoms on the surface to Re/Tl dopants. Error analysis plots help explain trends in BE errors from the parity plots and suggest that BE corrections can help reduce the errors from Alchemy. We then use machine learning models to predict corrections to BE calculated by Alchemy. The new parity plots show that BE from ML-corrected Alchemy agree with BE from DFT with the errors less than 0.1 eV.

8.0 SUMMARY AND FUTURE WORK

8.1 THERMODYNAMIC POURBAIX DIAGRAMS FOR CO_2 REDUCTION

In summary, design principles from our prior works led us to investigating pyridine based inorganic complexes and N-doped carbon materials for CO_2 reduction. We used atomistic thermodynamics and Pourbaix diagrams to develop a thermodynamic understanding of how different materials catalyze the process. Chapter 3 showed that $Ru(phen)_2(ppy)_2^{2+}$ is a potential candidate for participating in CO_2 reduction mechanisms as it was shown in experiments. Proton and hydride shuttling pathways in these complexes were thermodynamically feasible and should be considered for energetically efficient CO_2 reduction processes. Chapter 4 highlighted that reduction potentials for the materials should be tunable for energetically efficient catalysis using nitrogen concentration of carbonous materials. Reduced states of these materials can form frustrated Lewis pairs that would be applicable for energetically efficient (de)hydrogenation catalysis. In Chapter 5, combined Pourbaix diagrams and atomistic phase diagrams showed a partially reduced SnO_2 surface to take part in energetically efficient CO_2 reduction. With this model, we also identified dopants that would result in lower overpotentials for CO_2 reduction. Future work will focus on combining Pourbaix diagrams with kinetic studies to calculate electrochemical reaction barriers. This will likely involve modeling the reactions in an explicit solvation environment.

8.2 COMPUTATIONAL HIGH THROUGHPUT SCREENING USING ALCHEMY

Chapter 6 showed the promise of using Computational Alchemy as a means to rapidly calculate binding energies of OHx intermediates on hypothetical alloys. With minimal DFT calculations, alchemy was able predict BEs on hypothetical alloys within 0.1 eV of DFT energies. In Chapter 7, Alchemy was then able to predict BEs of OHx, CHx and NHx on an exhaustive set of alloys but with larger errors. In order to correct those errors, Machine learning was combined with Alchemy to learn error corrections. The resulting BEs from ML-corrected Alchemy resulted in very low errors (less than 0.1 eV) when compared with BE from DFT.

Our work so far in this thesis has just focused on calculating thermodynamic activity descriptors (BE) of alloy catalysts using ML/Alchemy. As explained in 2, stability of catalysts are important to identify promising catalysts. In order to develop a robust high throughput screening tool for catalysts, future work will focus on developing Alchemy based schemes to calculate stability descriptors. This will involve calculating free energies of processes (segregation, islanding and metal dissolution) that are likely to destabilize an alloy catalyst. We also need to develop composition dependent phase diagrams using Alchemy in order to identify the lowest energy configuration for any given composition of dopant atoms in the alloy.

In order to calculate reliable stabilization energies and phase diagrams from DFT, geometries of alloy slabs with and without an adsorbate need to be relaxed. However, Alchemy restricts us to calculating energetics of alloy slabs only when they are fixed to the lattice of reference slabs. This could be addressed by building machine learning models to predict the relaxation energies of the alloy catalysts. The models can be built using similar strategies described above. New fingerprinting methods need to be developed and more electronic structure theory based feature need to be identified to account for the relaxation effects.

All of our discussion has so far been based on just thermodynamic descriptors. However, accounting for kinetics is equally important in order to identify the rate limiting steps associated with each process. We hypothesize that if Alchemy was able to calculate binding

energies, it will also be able to predict energy of a transition state and hence the activation energy of a process on an alloy catalyst. Traditionally, transition state searches have involved nudged elastic band calculations between the reactant and product states which are slab and an adsorbate on slab calculations respectively. Transition state searches are computationally too expensive that just sites with the lowest energy of binding an adsorbate to the slab is chosen as the product state. However, in the case of alloy catalysts this would not be applicable as the lowest energy binding site would be different on different alloys and therefore the transition states would likely be different as well. In order to account for this, we need to consider reference calculations with adsorbates on all possible sites of a slab, use Alchemy to predict BE of adsorbate on all sites of an alloy and choose the lowest energy binding site for each site. The respective transition state and the activation energy can be then later be used in microkinetic models to predict the activity of alloy catalysts. Finally using a workflow including alchemical schemes for thermodynamic, kinetic and stability descriptors will let us reliably screen through the chemical space and help find promising catalysts.

APPENDIX A

SUPPORTING INFORMATION FOR INORGANIC COMPLEXES

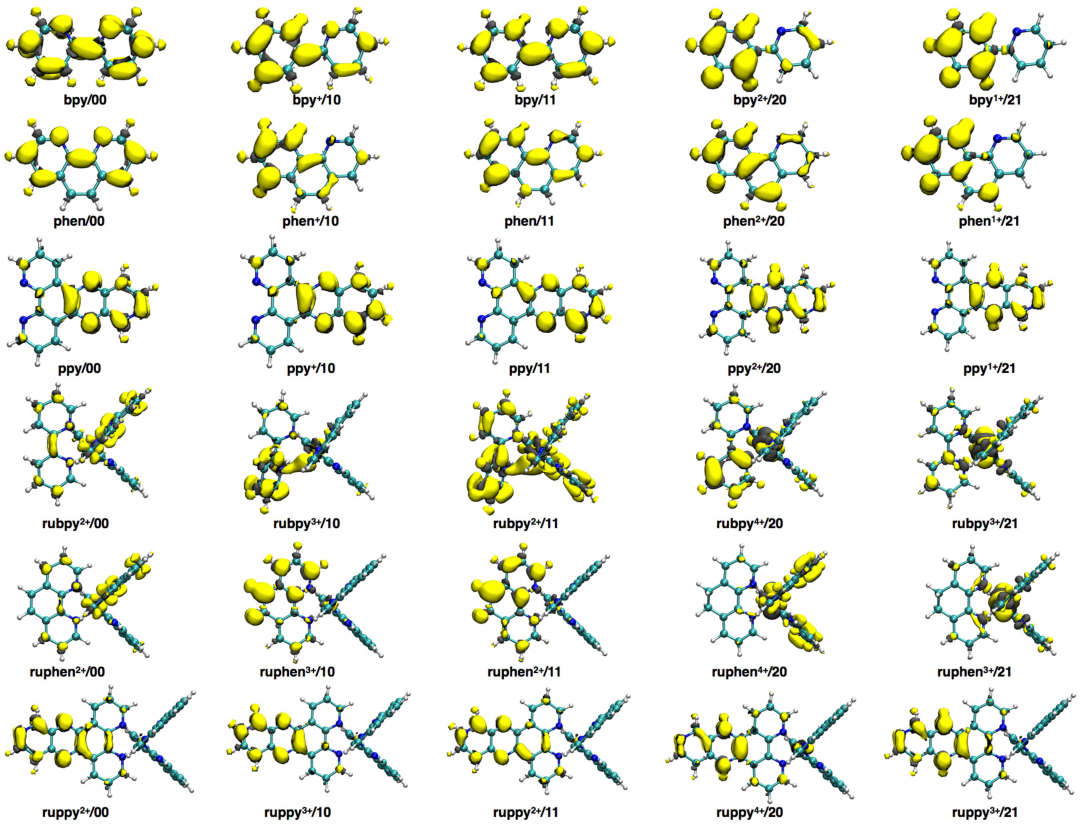

Figure A1: Electron density difference plots of all the molecules considered in our study. Isosurfaces in yellow indicate an increase in electron density and isosurfaces in blue indicate decrease in electron density upon the subtraction of an electron. These plots show the location of the LUMO orbital for each lowest energy structure.

APPENDIX B

SUPPORTING INFORMATION FOR NANOCARBONS

B.1 DATA TABLES FOR PHASE DIAGRAMS AND POURBAIX DIAGRAMS IN THE MANUSCRIPT

Table B1: Coefficients for boundary lines observed in the phase diagrams(Figure 4.4 a. and 4.4 b.) are listed here. m and c are the slope and y-intercept of the line equation, $y = mx+c$, and range indicates the domain of values in which the line equation is valid. The coefficients shown here were obtained by solving the free energy equation (Equation 4.11 for GBP and 4.12 for GR) at pH = 0.

Figure	Species	Slope (m)	Intercept (c)	Range
4 a	GBP/P4N+2H	2	-0.20	-0.19 $<\Delta\mu_N<0$
	GBP/GBP+2H	0	-0.68	-0.3 $<\Delta\mu_N<$-0.19
	P4N+2H/P4N+4H	0	-0.90	-0.19 $<\Delta\mu_N<0$
	GBP+2H/P4N+4H	2	-0.51	-0.29 $<\Delta\mu_N<$-0.19
	GBP+2H/P4N+2H	1	0	$\Delta\mu_N$ = -0.19 -0.9 <E <-0.68
4 b.	GR+1H/GR+2H	0	-0.59	-1.0 $<\Delta\mu_N<$-0.66
	GR+1N/GR+1N+2H	0	-0.09	-0.16 $<\Delta\mu_N<0$
	GR+1H/GR+1N	-1	-0.25	-0.34 $<\Delta\mu_N<$-0.16
	GR+1H/GR+1N+2H	1	0.07	-0.66 $<\Delta\mu_N<$-0.16
	GR+2H/GR+1N+2H	1	0	$\Delta\mu_N$ = -0.66 -1.0 <E <-0.59

Table B2: y intercept values for boundary lines observed in the Pourbaix diagrams(Figure 4.5 a-f.) are listed here. Slope, m, in Pourbaix diagrams is equal to the Nernstian constant 0.059 since every reduction is assumed to involve one H^+ and electron. m and c are the slope and y-intercept of the line equation, $y = mx + c$, and range of pH considered is between 0 and 14. Again, the y-intercept shown here were obtained by solving the free energy equation (Equation 4.11 for GBP and 4.12 for GR) at $\Delta\mu_N = 0$

Figure	Species	Intercept (c)
5 a.	GBP/GBP+2H	-0.68
5 b.	P3N+1H/P3N+2H	-0.26
	P3N+2H/P3N+3H	-1.28
5 c.	P4N+2H/P4N+4H	-0.90
5 d.	GR/GR+1H	0.36
	GR+1H/GR+2H	-0.59
5 e.	GR1N/GR1N+2H	-0.08
5 f.	GR2N-1H/GR2N+1H	-0.19

BIBLIOGRAPHY

[1] R. Zhang, W. Lv, and L. Lei, "Role of the oxide layer on sn electrode in electrochemical reduction of {CO2} to formate," *Applied Surface Science*, vol. 356, pp. 24 – 29, 2015.

[2] A. M. Appel, J. E. Bercaw, A. B. Bocarsly, H. Dobbek, D. L. DuBois, M. Dupuis, J. G. Ferry, E. Fujita, R. Hille, P. J. A. Kenis, C. A. Kerfeld, R. H. Morris, C. H. F. Peden, A. R. Portis, S. W. Ragsdale, T. B. Rauchfuss, J. N. H. Reek, L. C. Seefeldt, R. K. Thauer, and G. L. Waldrop, "Frontiers, opportunities, and challenges in biochemical and chemical catalysis of CO2fixation," *Chemical Reviews*, vol. 113, pp. 6621–6658, aug 2013.

[3] N. M. Rezayee, C. A. Huff, and M. S. Sanford, "Tandem Amine and Ruthenium-Catalyzed Hydrogenation of CO_2 to Methanol," *Journal of the American Chemical Society*, vol. 137, pp. 1028–1031, Jan. 2015.

[4] J. Kim, T. A. Johnson, J. E. Miller, E. B. Stechel, and C. T. Maravelias, "Fuel production from CO_2 using solar-thermal energy: system level analysis," *Energy & Environmental Science*, vol. 5, pp. 8417–8429, Sept. 2012.

[5] J. Qiao, Y. Liu, F. Hong, and J. Zhang, "A review of catalysts for the electroreduction of carbon dioxide to produce low-carbon fuels," *Chemical Society Reviews*, vol. 43, pp. 631–675, Dec. 2013.

[6] D. T. Whipple and P. J. A. Kenis, "Prospects of CO_2 Utilization via Direct Heterogeneous Electrochemical Reduction," *Journal of Physical Chemistry Letters*, vol. 1, pp. 3451–3458, Dec. 2010.

[7] J. Rosenthal, "Progress Toward the Electrocatalytic Production of Liquid Fuels from Carbon Dioxide," *Progress in Inorganic Chemistry, Vol 59*, vol. 59, pp. 299–338, 2014.

[8] S. C. Ma, M. Sadakiyo, R. Luo, M. Heima, M. Yamauchi, and P. J. A. Kenis, "One-step electrosynthesis of ethylene and ethanol from CO_2 in an alkaline electrolyzer," *Journal of Power Sources*, vol. 301, pp. 219–228, Jan. 2016.

[9] B. Kumar, M. Llorente, J. Froehlich, T. Dang, A. Sathrum, and C. P. Kubiak, "Photochemical and Photoelectrochemical Reduction of CO_2," *Annual Review of Physical Chemistry, Vol 63*, vol. 63, pp. 541–+, 2012.

[10] W. B. Hou, W. H. Hung, P. Pavaskar, A. Goeppert, M. Aykol, and S. B. Cronin, "Photocatalytic Conversion of CO_2 to Hydrocarbon Fuels via Plasmon-Enhanced Absorption and Metallic Interband Transitions," *Acs Catalysis*, vol. 1, pp. 929–936, Aug. 2011.

[11] S. Licht, "STEP (Solar Thermal Electrochemical Photo) Generation of Energetic Molecules: A Solar Chemical Process to End Anthropogenic Global Warming," *Journal of Physical Chemistry C*, vol. 113, pp. 16283–16292, Sept. 2009.

[12] S. Licht, O. Chitayat, H. Bergmann, A. Dick, H. Ayub, and S. Ghosh, "Efficient STEP (solar thermal electrochemical photo) production of hydrogen - an economic assessment," *International Journal of Hydrogen Energy*, vol. 35, pp. 10867–10882, Oct. 2010.

[13] Y. J. Zhu, B. H. Wang, X. L. Liu, H. Y. Wang, H. J. Wu, and S. Licht, "STEP organic synthesis: an efficient solar, electrochemical process for the synthesis of benzoic acid," *Green Chemistry*, vol. 16, no. 11, pp. 4758–4766, 2014.

[14] S. Lee and J. Lee, "Electrode build-up of reducible metal composites toward achievable electrochemical conversion of carbon dioxide," *ChemSusChem*, vol. 9, pp. 333–344, nov 2015.

[15] M. Azuma, "Electrochemical reduction of carbon dioxide on various metal electrodes in low-temperature aqueous KHCO[sub 3] media," *Journal of The Electrochemical Society*, vol. 137, no. 6, p. 1772, 1990.

[16] D. R. Weinberg, C. J. Gagliardi, J. F. Hull, C. F. Murphy, C. A. Kent, B. C. Westlake, A. Paul, D. H. Ess, D. G. McCafferty, and T. J. Meyer, "Proton-Coupled Electron Transfer," *Chemical Reviews*, vol. 112, pp. 4016–4093, July 2012.

[17] J. L. Dempsey and T. T. Eisenhart, "New approaches to probe proton-coupled electron transfer reaction pathways," *Abstracts of Papers of the American Chemical Society*, vol. 247, Mar. 2014.

[18] S. Hammes-Schiffer, "Theory of Proton-Coupled Electron Transfer in Energy Conversion Processes," *Accounts of Chemical Research*, vol. 42, pp. 1881–1889, Dec. 2009.

[19] A. Marjolin and J. A. Keith, "Thermodynamic Descriptors for Molecules That Catalyze Efficient CO_2 Electroreductions," *Acs Catalysis*, vol. 5, pp. 1123–1130, Feb. 2015.

[20] J. A. Keith and E. A. Carter, "Electrochemical reactivities of pyridinium in solution: consequences for CO_2 reduction mechanisms," *Chemical Science*, vol. 4, pp. 1490–1496, Mar. 2013.

[21] J. K. Nørskov, J. Rossmeisl, A. Logadottir, L. Lindqvist, J. R. Kitchin, T. Bligaard, and H. Jónsson, "Origin of the overpotential for oxygen reduction at a fuel-cell cathode," *The Journal of Physical Chemistry B*, vol. 108, pp. 17886–17892, nov 2004.

[22] M. C. Groenenboom, K. Saravanan, Y. Zhu, J. M. Carr, A. Marjolin, G. G. Faura, E. C. Yu, R. N. Dominey, and J. A. Keith, "Structural and substituent group effects on multielectron standard reduction potentials of aromatic n-heterocycles," *The Journal of Physical Chemistry A*, vol. 120, no. 34, pp. 6888–6894, 2016.

[23] P. Strasser, Q. Fan, M. Devenney, W. H. Weinberg, P. Liu, and J. K. Nørskov, "High throughput experimental and theoretical predictive screening of materials- a comparative study of search strategies for new fuel cell anode catalysts," *The Journal of Physical Chemistry B*, vol. 107, no. 40, pp. 11013–11021, 2003.

[24] S. M. Senkan, "High-throughput screening of solid-state catalyst libraries," *Nature*, vol. 394, no. 6691, pp. 350–353, 1998.

[25] O. Trapp, S. K. Weber, S. Bauch, and W. Hofstadt, "High-throughput screening of catalysts by combining reaction and analysis," *Angewandte Chemie International Edition*, vol. 46, no. 38, pp. 7307–7310, 2007.

[26] D. W. Robbins and J. F. Hartwig, "A simple, multidimensional approach to high-throughput discovery of catalytic reactions," *Science*, vol. 333, no. 6048, pp. 1423–1427, 2011.

[27] P. Cong, R. D. Doolen, Q. Fan, D. M. Giaquinta, S. Guan, E. W. McFarland, D. M. Poojary, K. Self, H. W. Turner, and W. H. Weinberg, "High-throughput synthesis and screening of combinatorial heterogeneous catalyst libraries," *Angewandte Chemie International Edition*, vol. 38, no. 4, pp. 483–488, 1999.

[28] M. Mavrikakis, "Computational methods: A search engine for catalysts," *Nature materials*, vol. 5, no. 11, pp. 847–848, 2006.

[29] J. Greeley, I. Stephens, A. Bondarenko, T. P. Johansson, H. A. Hansen, T. Jaramillo, J. Rossmeisl, I. Chorkendorff, and J. K. Nørskov, "Alloys of platinum and early transition metals as oxygen reduction electrocatalysts," *Nature chemistry*, vol. 1, no. 7, pp. 552–556, 2009.

[30] J. Greeley, T. F. Jaramillo, J. Bonde, I. Chorkendorff, and J. K. Nørskov, "Computational high-throughput screening of electrocatalytic materials for hydrogen evolution," *Nature materials*, vol. 5, no. 11, pp. 909–913, 2006.

[31] H. S. Taylor, "A theory of the catalytic surface," *Proceedings of the Royal Society of London. Series A, Containing Papers of a Mathematical and Physical Character*, vol. 108, no. 745, pp. 105–111, 1925.

[32] T. Zambelli, J. Wintterlin, J. Trost, and G. Ertl, "Identification of the" active sites" of a surface-catalyzed reaction," *Science*, vol. 273, no. 5282, p. 1688, 1996.

[33] B. Hammer and J. K. Nørskov, "Theoretical surface science and catalysiscalculations and concepts," *Advances in catalysis*, vol. 45, pp. 71–129, 2000.

[34] L. D. Burke and A. P. O'Mullane, "Generation of active surface states of gold and the role of such states in electrocatalysis," *Journal of Solid State Electrochemistry*, vol. 4, no. 5, pp. 285–297, 2000.

[35] J. K. Nørskov, F. Abild-Pedersen, F. Studt, and T. Bligaard, "Density functional theory in surface chemistry and catalysis," *Proceedings of the National Academy of Sciences*, vol. 108, no. 3, pp. 937–943, 2011.

[36] T. Bligaard, J. K. Nørskov, S. Dahl, J. Matthiesen, C. H. Christensen, and J. Sehested, "The brønsted–evans–polanyi relation and the volcano curve in heterogeneous catalysis," *Journal of Catalysis*, vol. 224, no. 1, pp. 206–217, 2004.

[37] K. Jens, F. Studt, F. Abild-Pedersen, and T. Bligaard, *Fundamental concepts in heterogeneous catalysis*. John Wiley & Sons, 2014.

[38] F. Abild-Pedersen, J. Greeley, F. Studt, J. Rossmeisl, T. Munter, P. G. Moses, E. Skulason, T. Bligaard, and J. K. Nørskov, "Scaling properties of adsorption energies for hydrogen-containing molecules on transition-metal surfaces," *Physical review letters*, vol. 99, no. 1, p. 016105, 2007.

[39] B. Hammer and J. Nørskov, "Electronic factors determining the reactivity of metal surfaces," *Surface Science*, vol. 343, no. 3, pp. 211–220, 1995.

[40] A. J. Medford, C. Shi, M. J. Hoffmann, A. C. Lausche, S. R. Fitzgibbon, T. Bligaard, and J. K. Nørskov, "Catmap: a software package for descriptor-based microkinetic mapping of catalytic trends," *Catalysis Letters*, vol. 145, no. 3, pp. 794–807, 2015.

[41] A. J. Medford, A. Vojvodic, J. S. Hummelshøj, J. Voss, F. Abild-Pedersen, F. Studt, T. Bligaard, A. Nilsson, and J. K. Nørskov, "From the sabatier principle to a predictive theory of transition-metal heterogeneous catalysis," *Journal of Catalysis*, vol. 328, pp. 36–42, 2015.

[42] H. A. Hansen, J. B. Varley, A. A. Peterson, and J. K. Nørskov, "Understanding trends in the electrocatalytic activity of metals and enzymes for co2 reduction to co," *The journal of physical chemistry letters*, vol. 4, no. 3, pp. 388–392, 2013.

[43] V. Viswanathan, H. A. Hansen, J. Rossmeisl, and J. K. Nørskov, "Universality in oxygen reduction electrocatalysis on metal surfaces," *ACS Catalysis*, vol. 2, no. 8, pp. 1654–1660, 2012.

[44] F. Besenbacher, I. Chorkendorff, B. Clausen, B. Hammer, A. Molenbroek, J. K. Nørskov, and I. Stensgaard, "Design of a surface alloy catalyst for steam reforming," *Science*, vol. 279, no. 5358, pp. 1913–1915, 1998.

[45] J. Greeley and M. Mavrikakis, "Alloy catalysts designed from first principles," *Nature materials*, vol. 3, no. 11, pp. 810–815, 2004.

[46] F. Studt, F. Abild-Pedersen, T. Bligaard, R. Z. Sørensen, C. H. Christensen, and J. K. Nørskov, "Identification of non-precious metal alloy catalysts for selective hydrogenation of acetylene," *Science*, vol. 320, no. 5881, pp. 1320–1322, 2008.

[47] B. Gurau, R. Viswanathan, R. Liu, T. J. Lafrenz, K. L. Ley, E. Smotkin, E. Reddington, A. Sapienza, B. C. Chan, T. E. Mallouk, *et al.*, "Structural and electrochemical characterization of binary, ternary, and quaternary platinum alloy catalysts for methanol electro-oxidation," *The Journal of Physical Chemistry B*, vol. 102, no. 49, pp. 9997–10003, 1998.

[48] M.-k. Min, J. Cho, K. Cho, and H. Kim, "Particle size and alloying effects of pt-based alloy catalysts for fuel cell applications," *Electrochimica Acta*, vol. 45, no. 25, pp. 4211–4217, 2000.

[49] A. U. Nilekar, Y. Xu, J. Zhang, M. B. Vukmirovic, K. Sasaki, R. R. Adzic, and M. Mavrikakis, "Bimetallic and ternary alloys for improved oxygen reduction catalysis," *Topics in Catalysis*, vol. 46, no. 3-4, pp. 276–284, 2007.

[50] V. Tripkovic, H. A. Hansen, J. Rossmeisl, and T. Vegge, "First principles investigation of the activity of thin film pt, pd and au surface alloys for oxygen reduction," *Physical Chemistry Chemical Physics*, vol. 17, no. 17, pp. 11647–11657, 2015.

[51] S. Lankiang, M. Chiwata, S. Baranton, H. Uchida, and C. Coutanceau, "Oxygen reduction reaction at binary and ternary nanocatalysts based on pt, pd and au," *Electrochimica Acta*, vol. 182, pp. 131–142, 2015.

[52] D. A. Hansgen, D. G. Vlachos, and J. G. Chen, "Using first principles to predict bimetallic catalysts for the ammonia decomposition reaction," *Nature chemistry*, vol. 2, no. 6, pp. 484–489, 2010.

[53] Z. P. Jovanov, H. A. Hansen, A. S. Varela, P. Malacrida, A. A. Peterson, J. K. Nørskov, I. E. Stephens, and I. Chorkendorff, "Opportunities and challenges in the electrocatalysis of CO 2 and CO reduction using bifunctional surfaces: A theoretical and experimental study of au–cd alloys," *Journal of Catalysis*, vol. 343, pp. 215–231, nov 2016.

[54] M. P. Andersson, T. Bligaard, A. Kustov, K. E. Larsen, J. Greeley, T. Johannessen, C. H. Christensen, and J. K. Nørskov, "Toward computational screening in heterogeneous catalysis: Pareto-optimal methanation catalysts," *Journal of Catalysis*, vol. 239, no. 2, pp. 501–506, 2006.

[55] J. Greeley and J. K. Nørskov, "Large-scale, density functional theory-based screening of alloys for hydrogen evolution," *Surface Science*, vol. 601, no. 6, pp. 1590–1598, 2007.

[56] J. Greeley and J. K. Nørskov, "Combinatorial density functional theory-based screening of surface alloys for the oxygen reduction reaction," *The Journal of Physical Chemistry C*, vol. 113, no. 12, pp. 4932–4939, 2009.

[57] J. Greeley and J. K. Nørskov, "Electrochemical dissolution of surface alloys in acids: Thermodynamic trends from first-principles calculations," *Electrochimica Acta*, vol. 52, no. 19, pp. 5829–5836, 2007.

[58] T. P. Straatsma and J. A. McCammon, "Computational alchemy," *Annu. Rev. Phys. Chem.*, vol. 43, pp. 407–435, oct 1992.

[59] V. Helms and R. C. Wade, "Computational alchemy to calculate absolute protein-ligand binding free energy," *J. Am. Chem. Soc.*, vol. 120, pp. 2710–2713, apr 1998.

[60] D. Cappel, M. L. Hall, E. B. Lenselink, T. Beuming, J. Qi, J. Bradner, and W. Sherman, "Relative binding free energy calculations applied to protein homology models," *Journal of chemical information and modeling*, vol. 56, no. 12, pp. 2388–2400, 2016.

[61] M. Wang, X. Hu, D. N. Beratan, and W. Yang, "Designing molecules by optimizing potentials," *Journal of the American Chemical Society*, vol. 128, no. 10, pp. 3228–3232, 2006.

[62] D. Xiao, W. Yang, and D. N. Beratan, "Inverse molecular design in a tight-binding framework," *The Journal of chemical physics*, vol. 129, no. 4, p. 044106, 2008.

[63] X. Hu, D. N. Beratan, and W. Yang, "A gradient-directed monte carlo approach to molecular design," *The Journal of chemical physics*, vol. 129, no. 6, p. 064102, 2008.

[64] D. Balamurugan, W. Yang, and D. N. Beratan, "Exploring chemical space with discrete, gradient, and hybrid optimization methods," *The Journal of chemical physics*, vol. 129, no. 17, p. 174105, 2008.

[65] O. A. von Lilienfeld, R. D. Lins, and U. Rothlisberger, "Variational particle number approach for rational compound design," *Phys. Rev. Lett.*, vol. 95, p. 153002, oct 2005.

[66] O. A. von Lilienfeld and M. E. Tuckerman, "Molecular grand-canonical ensemble density functional theory and exploration of chemical space," *J. Chem. Phys.*, vol. 125, p. 154104, oct 2006.

[67] O. A. von Lilienfeld and M. E. Tuckerman, "Alchemical variations of intermolecular energies according to molecular grand-canonical ensemble density functional theory," *J. Chem. Theory Comput.*, vol. 3, no. 3, pp. 1083–1090, 2007. PMID: 26627427.

[68] O. A. von Lilienfeld, "Accurate ab initio energy gradients in chemical compound space," *J. Chem. Phys.*, vol. 131, p. 164102, oct 2009.

[69] R. Balawender, M. A. Welearegay, M. Lesiuk, F. De Proft, and P. Geerlings, "Exploring chemical space with the alchemical derivatives," *Journal of chemical theory and computation*, vol. 9, no. 12, pp. 5327–5340, 2013.

[70] A. Solovyeva and O. A. von Lilienfeld, "Alchemical screening of ionic crystals," *Phys. Chem. Chem. Phys.*, vol. 18, no. 45, pp. 31078–31091, 2016.

[71] M. to Baben, J. O. Achenbach, and O. A. von Lilienfeld, "Guiding ab initio calculations by alchemical derivatives," *J. Chem. Phys.*, vol. 144, p. 104103, mar 2016.

[72] D. Sheppard, G. Henkelman, and O. A. von Lilienfeld, "Alchemical derivatives of reaction energetics," *J. Chem. Phys.*, vol. 133, p. 084104, aug 2010.

[73] Y. S. Al-Hamdani, A. Michaelides, and O. A. von Lilienfeld, "Exploring dissociative water adsorption on isoelectronically bn doped graphene using alchemical derivatives," *The Journal of chemical physics*, vol. 147, no. 16, p. 164113, 2017.

[74] E. Kimura, X. Bu, M. Shionoya, S. Wada, and S. Maruyama, "A new nickel(II) cyclam (cyclam = 1,4,8,11-tetraazacyclotetradecane) complex covalently attached to tris(1,10-phenanthroline)ruthenium(2+). A new candidate for the catalytic photoreduction of carbon dioxide," *Inorganic Chemistry*, vol. 31, pp. 4542–4546, Oct. 1992.

[75] D. J. Boston, C. Xu, D. W. Armstrong, and F. M. MacDonnell, "Photochemical Reduction of Carbon Dioxide to Methanol and Formate in a Homogeneous System with Pyridinium Catalysts," *Journal of the American Chemical Society*, vol. 135, pp. 16252–16255, Nov. 2013.

[76] D. J. Boston, Y. M. F. Pachn, R. O. Lezna, N. R. de Tacconi, and F. M. MacDonnell, "Electrocatalytic and Photocatalytic Conversion of CO_2 to Methanol using Ruthenium Complexes with Internal Pyridyl Cocatalysts," *Inorganic Chemistry*, vol. 53, pp. 6544–6553, July 2014.

[77] K. Kobayashi, H. Ohtsu, K. Nozaki, S. Kitagawa, and K. Tanaka, "Photochemical Properties and Reactivity of a Ru Compound Containing an NAD/NADH-Functionalized 1,10-Phenanthroline Ligand," *Inorganic Chemistry*, Feb. 2016.

[78] E. E. Barton, D. M. Rampulla, and A. B. Bocarsly, "Selective solar-driven reduction of CO 2 to methanol using a catalyzed p-GaP based photoelectrochemical cell," *J. Am. Chem. Soc.*, vol. 130, pp. 6342–6344, may 2008.

[79] E. B. Cole, P. S. Lakkaraju, D. M. Rampulla, A. J. Morris, E. Abelev, and A. B. Bocarsly, "Using a One-Electron Shuttle for the Multielectron Reduction of CO_2 to Methanol: Kinetic, Mechanistic, and Structural Insights," *Journal of the American Chemical Society*, vol. 132, pp. 11539–11551, Aug. 2010.

[80] G. Seshadri, C. Lin, and A. B. Bocarsly, "A new homogeneous electrocatalyst for the reduction of carbon dioxide to methanol at low overpotential," *Journal of Electroanalytical Chemistry*, vol. 372, pp. 145–150, July 1994.

[81] M. Von Arnim and R. Ahlrichs, "Performance of parallel TURBOMOLE for density functional calculations," *Journal of Computational Chemistry*, vol. 19, no. 15, pp. 1746–1757, 1998.

[82] K. Eichkorn, O. Treutler, H. hm, M. Hser, and R. Ahlrichs, "Auxiliary basis sets to approximate Coulomb potentials," *Chemical Physics Letters*, vol. 240, pp. 283–290, June 1995.

[83] K. Eichkorn, F. Weigend, O. Treutler, and R. Ahlrichs, "Auxiliary basis sets for main row atoms and transition metals and their use to approximate Coulomb potentials," *Theoretical Chemistry Accounts*, vol. 97, no. 1, pp. 119–124, 1997.

[84] R. Ahlrichs, M. Br, M. Hser, H. Horn, and C. Klmel, "Electronic structure calculations on workstation computers: The program system turbomole," *Chemical Physics Letters*, vol. 162, pp. 165–169, Oct. 1989.

[85] A. D. Becke, "Densityfunctional thermochemistry. III. The role of exact exchange," *The Journal of Chemical Physics*, vol. 98, no. 7, pp. 5648–5652, 1993.

[86] C. Lee, W. Yang, and R. G. Parr, "Development of the Colle-Salvetti correlation-energy formula into a functional of the electron density," *Physical Review B*, vol. 37, no. 2, pp. 785–789, 1988.

[87] A. Schfer, H. Horn, and R. Ahlrichs, "Fully optimized contracted Gaussian basis sets for atoms Li to Kr," *The Journal of Chemical Physics*, vol. 97, no. 4, pp. 2571–2577, 1992.

[88] A. Schfer, C. Huber, and R. Ahlrichs, "Fully optimized contracted Gaussian basis sets of triple zeta valence quality for atoms Li to Kr," *The Journal of Chemical Physics*, vol. 100, no. 8, pp. 5829–5835, 1994.

[89] A. Schafer, A. Klamt, D. Sattel, J. C. W. Lohrenz, and F. Eckert, "COSMO Implementation in TURBOMOLE: Extension of an efficient quantum chemical code towards liquid systems," *Physical Chemistry Chemical Physics*, vol. 2, no. 10, pp. 2187–2193, 2000.

[90] C. V. Krishnan, C. Creutz, H. A. Schwarz, and N. Sutin, "Reduction potentials for 2,2'-bipyridine and 1,10-phenanthroline couples in aqueous solutions," *Journal of the American Chemical Society*, vol. 105, pp. 5617–5623, Aug. 1983.

[91] D.-Y. Liu, Y.-Y. Xin, X.-W. He, and X.-B. Yin, "A sensitive, non-damaging electrochemiluminescent aptasensor via a low potential approach at DNA-modified gold electrodes," *Analyst*, vol. 136, pp. 479–485, Jan. 2011.

[92] C. Creutz and M. H. Chou, "Hydricities of d(6) Metal Hydride Complexes in Water," *Journal of the American Chemical Society*, vol. 131, p. 2794, Mar. 2009.

[93] R. Leuschner, H. Krohn, and J. K. Dohrmann, "Termination Rates by Time-Resolved ESR. The N-Hydropyridinyl Radical in Solution and the Influence of Non-Uniform Radical Concentration on the Apparent Rate Constant," *Berichte der Bunsengesellschaft fr physikalische Chemie*, vol. 88, no. 5, pp. 462–466, 1984.

[94] F. Riboni, E. Selli, M. R. Hoffmann, and A. J. Colussi, "Homogeneous Reduction of CO_2 by Photogenerated Pyridinyl Radicals," *Journal of Physical Chemistry A*, vol. 119, pp. 4433–4438, May 2015.

[95] C. H. Lim, A. M. Holder, J. T. Hynes, and C. B. Musgrave, "Reduction of CO_2 to Methanol Catalyzed by a Biomimetic Organo-Hydride Produced from Pyridine," *Journal of the American Chemical Society*, vol. 136, pp. 16081–16095, Nov. 2014.

[96] C. H. Lim, A. M. Holder, J. T. Hynes, and C. B. Musgrave, "Catalytic Reduction of CO_2 by Renewable Organohydrides," *Journal of Physical Chemistry Letters*, vol. 6, pp. 5078–5092, Dec. 2015.

[97] B. Hammer and J. K. Norskov, "Why gold is the noblest of all the metals," *Nature*, vol. 376, pp. 238–240, jul 1995.

[98] E. Nakamura and K. Sato, "Managing the scarcity of chemical elements," *Nature materials*, vol. 10, no. 3, pp. 158–161, 2011.

[99] C. Jaffray and G. Hards, *Precious metal supply requirements*. John Wiley and Sons, Ltd, 2010.

[100] R. J. Farrauto, Y. Liu, W. Ruettinger, O. Ilinich, L. Shore, and T. Giroux, "Precious metal catalysts supported on ceramic and metal monolithic structures for the hydrogen economy," *Catalysis Reviews*, vol. 49, no. 2, pp. 141–196, 2007.

[101] R. Bashyam and P. Zelenay, "A class of non-precious metal composite catalysts for fuel cells," *Nature*, vol. 443, pp. 63–66, sep 2006.

[102] D. S. Su, J. Zhang, B. Frank, A. Thomas, X. Wang, J. Paraknowitsch, and R. Schlögl, "Metal-free heterogeneous catalysis for sustainable chemistry.," *ChemSusChem*, vol. 3, pp. 169–80, feb 2010.

[103] E. Auer, A. Freund, J. Pietsch, and T. Tacke, "Carbons as supports for industrial precious metal catalysts," *Applied Catalysis A: General*, vol. 173, no. 2, pp. 259–271, 1998.

[104] J. Duan, S. Chen, M. Jaroniec, and S. Z. Qiao, "Heteroatom-Doped Graphene-Based Materials for Energy-Relevant Electrocatalytic Processes," *ACS Catalysis*, vol. 5, pp. 5207–5234, sep 2015.

[105] X.-L. Wu, T. Wen, H.-L. Guo, S. Liu, X. Wang, A.-W. Xu, and M. Mezger, "Self-templated synthesis of novel carbon nanoarchitectures for efficient electrocatalysis," *Scientific Reports*, vol. 6, p. 28049, jun 2016.

[106] J. Wei, D. Zhou, Z. Sun, Y. Deng, Y. Xia, and D. Zhao, "A Controllable Synthesis of Rich Nitrogen-Doped Ordered Mesoporous Carbon for CO 2 Capture and Supercapacitors," *Advanced Functional Materials*, vol. 23, pp. 2322–2328, may 2013.

[107] M. Zhong, S. Jiang, Y. Tang, E. Gottlieb, E. K. Kim, A. Star, K. Matyjaszewski, and T. Kowalewski, "Block copolymer-templated nitrogen-enriched nanocarbons with morphology-dependent electrocatalytic activity for oxygen reduction," *Chemical Science*, vol. 5, no. 8, p. 3315, 2014.

[108] Y. Zheng, J. Liu, J. Liang, M. Jaroniec, and S. Z. Qiao, "Graphitic carbon nitride materials: controllable synthesis and applications in fuel cells and photocatalysis," *Energy Environ. Sci.*, vol. 5, no. 5, pp. 6717–6731, 2012.

[109] E. Gottlieb, M. Kopec, M. Banerjee, J. W. Mohin, D. Yaron, K. Matyjaszewski, and T. Kowalewski, "In-situ Platinum Deposition on Nitrogen-doped Carbon Films as a Source of Catalytic Activity in a Hydrogen Evolution Reaction," *ACS Applied Materials & Interfaces*, no. Just Accepted, 2016.

[110] W. Ding, Z. Wei, S. Chen, X. Qi, T. Yang, J. Hu, D. Wang, L.-J. Wan, S. F. Alvi, and L. Li, "Space-Confinement-Induced Synthesis of Pyridinic- and Pyrrolic-Nitrogen-Doped Graphene for the Catalysis of Oxygen Reduction," *Angewandte Chemie*, vol. 125, pp. 11971–11975, nov 2013.

[111] M. Seredych and T. J. Bandosz, "Confined space reduced graphite oxide doped with sulfur as metal-free oxygen reduction catalyst," *Carbon*, vol. 66, pp. 227–233, jan 2014.

[112] J. E. Trancik, S. C. Barton, and J. Hone, "Transparent and Catalytic Carbon Nanotube Films," *Nano Letters*, vol. 8, no. 4, pp. 982–987, 2008.

[113] J.-P. Tessonnier, A. Villa, O. Majoulet, D. S. Su, and R. Schlögl, "Defect-mediated functionalization of carbon nanotubes as a route to design single-site basic heterogeneous catalysts for biomass conversion.," *Angewandte Chemie (International ed. in English)*, vol. 48, pp. 6543–6, jan 2009.

[114] L. Wang, A. Ambrosi, and M. Pumera, "Metal-free catalytic oxygen reduction reaction on heteroatom- doped graphene is caused by trace metal impurities.," *Angewandte Chemie (International ed. in English)*, vol. 52, pp. 13818–21, dec 2013.

[115] G. Dong, M. Fang, H. Wang, S. Yip, H.-Y. Cheung, F. Wang, C.-Y. Wong, S. T. Chu, and J. C. Ho, "Insight into the electrochemical activation of carbon-based cathodes for hydrogen evolution reaction," *J. Mater. Chem. A*, vol. 3, no. 24, pp. 13080–13086, 2015.

[116] H. Kim, K. Lee, S. I. Woo, and Y. Jung, "On the mechanism of enhanced oxygen reduction reaction in nitrogen-doped graphene nanoribbons.," *Physical chemistry chemical physics : PCCP*, vol. 13, pp. 17505–10, oct 2011.

[117] W. Yuan, Y. Zhou, Y. Li, C. Li, H. Peng, J. Zhang, Z. Liu, L. Dai, and G. Shi, "The edge- and basal-plane-specific electrochemistry of a single-layer graphene sheet.," *Scientific reports*, vol. 3, p. 2248, jan 2013.

[118] A. Shen, Y. Zou, Q. Wang, R. A. W. Dryfe, X. Huang, S. Dou, L. Dai, and S. Wang, "Oxygen Reduction Reaction in a Droplet on Graphite: Direct Evidence that the Edge is More Active than the Basal Plane.," *Angewandte Chemie (International ed. in English)*, vol. 53, pp. 10804–8, aug 2014.

[119] L. Zhang and Z. Xia, "Mechanisms of Oxygen Reduction Reaction on Nitrogen-Doped Graphene for Fuel Cells," *The Journal of Physical Chemistry C*, vol. 115, pp. 11170–11176, jun 2011.

[120] Y. Zheng, Y. Jiao, Y. Zhu, L. H. Li, Y. Han, Y. Chen, A. Du, M. Jaroniec, and S. Z. Qiao, "Hydrogen evolution by a metal-free electrocatalyst.," *Nature communications*, vol. 5, p. 3783, jan 2014.

[121] Y. Zheng, Y. Jiao, L. H. Li, T. Xing, Y. Chen, M. Jaroniec, and S. Z. Qiao, "Toward Design of Synergistically Active Carbon-Based Catalysts for Electrocatalytic Hydrogen Evolution," *ACS Nano*, vol. 8, no. 5, pp. 5290–5296, 2014.

[122] W. A. Saidi, "Oxygen reduction electrocatalysis using n-doped graphene quantum-dots," *J. Phys. Chem. Lett.*, vol. 4, pp. 4160–4165, dec 2013.

[123] B. Kumar, M. Asadi, D. Pisasale, S. Sinha-Ray, B. A. Rosen, R. Haasch, J. Abiade, A. L. Yarin, and A. Salehi-Khojin, "Renewable and metal-free carbon nanofibre catalysts for carbon dioxide reduction," *Nature Communications*, vol. 4, dec 2013.

[124] H. Wang, Y. Chen, X. Hou, C. Ma, and T. Tan, "Nitrogen-doped graphenes as efficient electrocatalysts for the selective reduction of carbon dioxide to formate in aqueous solution," *Green Chem.*, vol. 18, no. 11, pp. 3250–3256, 2016.

[125] J. Wu, M. Liu, P. P. Sharma, R. M. Yadav, L. Ma, Y. Yang, X. Zou, X. D. Zhou, R. Vajtai, B. I. Yakobson, J. Lou, and P. M. Ajayan, "Incorporation of Nitrogen Defects for Efficient Reduction of CO2 via Two-Electron Pathway on Three-Dimensional Graphene Foam," *Nano Letters*, vol. 16, no. 1, pp. 466–470, 2016.

[126] S. Zhang, P. Kang, S. Ubnoske, M. K. Brennaman, N. Song, R. L. House, J. T. Glass, and T. J. Meyer, "Polyethylenimine-Enhanced Electrocatalytic Reduction of CO 2 to Formate at Nitrogen-Doped Carbon Nanomaterials," *Journal of the American Chemical Society*, vol. 136, no. 22, pp. 7845–7848, 2014.

[127] J. Wu, R. M. Yadav, M. Liu, P. P. Sharma, C. S. Tiwary, L. Ma, X. Zou, X.-D. Zhou, B. I. Yakobson, J. Lou, and P. M. Ajayan, "Achieving Highly Efficient, Selective, and Stable CO2 Reduction on Nitrogen-Doped Carbon Nanotubes," *ACS Nano*, vol. 9, no. 5, p. 150423123413002, 2015.

[128] G.-L. Chai and Z.-X. Guo, "Highly effective sites and selectivity of nitrogen-doped graphene/CNT catalysts for CO2 electrochemical reduction," *Chem. Sci.*, vol. 7, no. 2, pp. 1268–1275, 2016.

[129] Y. Liu, J. Zhao, and Q. Cai, "Pyrrolic-nitrogen doped graphene: a metal-free electrocatalyst with high efficiency and selectivity for the reduction of carbon dioxide to formic acid: a computational study," *Phys. Chem. Chem. Phys.*, vol. 18, no. 7, pp. 5491–5498, 2016.

[130] J. A. Keith and E. A. Carter, "Electrochemical reactivities of pyridinium in solution: consequences for co 2 reduction mechanisms," *Chemical Science*, vol. 4, no. 4, pp. 1490–1496, 2013.

[131] A. Marjolin and J. A. Keith, "Thermodynamic Descriptors for Molecules the Catalyze Efficient CO 2 Electroreductions," *ACS Catalysis*, vol. 5, p. 150106113904007, jan 2015.

[132] C. H. Lim, A. M. Holder, J. T. Hynes, and C. B. Musgrave, "Roles of the Lewis acid and base in the chemical reduction of CO2 catalyzed by frustrated Lewis pairs," *Inorg Chem*, vol. 52, no. 17, pp. 10062–10066, 2013.

[133] E. B. Cole, P. S. Lakkaraju, D. M. Rampulla, A. J. Morris, E. Abelev, and A. B. Bocarsly, "Using a one-electron shuttle for the multielectron reduction of CO 2 to methanol: Kinetic, mechanistic, and structural insights," *J. Am. Chem. Soc.*, vol. 132, pp. 11539–11551, aug 2010.

[134] J. K. Nørskov, J. Rossmeisl, A. Logadottir, L. Lindqvist, J. R. Kitchin, T. Bligaard, and H. Jónsson, "Origin of the overpotential for oxygen reduction at a fuel-cell cathode," *The Journal of Physical Chemistry B*, vol. 108, pp. 17886–17892, nov 2004.

[135] K. Reuter and M. Scheffler, "First-principles atomistic thermodynamics for oxidation catalysis: Surface phase diagrams and catalytically interesting regions," *Phys. Rev. Lett.*, vol. 90, jan 2003.

[136] G. Kresse and J. Furthmüller, "Efficiency of ab-initio total energy calculations for metals and semiconductors using a plane-wave basis set," *Computational Materials Science*, vol. 6, pp. 15–50, jul 1996.

[137] G. Kresse and J. Furthmüller, "Efficient iterative schemes for ab initio total-energy calculations using a plane-wave basis set," *Physical Review B*, vol. 54, pp. 11169–11186, oct 1996.

[138] J. P. Perdew, K. Burke, and M. Ernzerhof, "Generalized Gradient Approximation Made Simple," *Physical Review Letters*, vol. 77, pp. 3865–3868, oct 1996.

[139] J. P. Perdew, J. A. Chevary, S. H. Vosko, K. A. Jackson, M. R. Pederson, D. J. Singh, and C. Fiolhais, "Atoms, molecules, solids, and surfaces: Applications of the generalized gradient approximation for exchange and correlation," *Physical Review B*, vol. 46, pp. 6671–6687, sep 1992.

[140] P. E. Blöchl, "Projector augmented-wave method," *Phys. Rev. B*, vol. 50, pp. 17953–17979, dec 1994.

[141] G. Kresse and D. Joubert, "From ultrasoft pseudopotentials to the projector augmented-wave method," *Physical Review B*, vol. 59, pp. 1758–1775, jan 1999.

[142] D. W. Boukhvalov, M. I. Katsnelson, and A. I. Lichtenstein, "Hydrogen on graphene: Electronic structure, total energy, structural distortions and magnetism from first-principles calculations," *Phys. Rev. B*, vol. 77, p. 35427, jan 2008.

[143] S. Zhang, S. Tsuzuki, K. Ueno, K. Dokko, and M. Watanabe, "Upper Limit of Nitrogen Content in Carbon Materials," *Angewandte Chemie International Edition*, vol. 54, pp. 1302–1306, jan 2015.

[144] J. Ye and J. K. Johnson, "Design of Lewis Pair-Functionalized Metal Organic Frameworks for CO 2 Hydrogenation," *ACS Catalysis*, vol. 5, no. 5, pp. 2921–2928, 2015.

[145] D. Wei, Y. Liu, Y. Wang, H. Zhang, L. Huang, and G. Yu, "Synthesis of N-Doped Graphene by Chemical Vapor Deposition and Its Electrical Properties," *Nano Letters*, vol. 9, pp. 1752–1758, may 2009.

[146] Z. Hou, X. Wang, T. Ikeda, K. Terakura, M. Oshima, M.-a. Kakimoto, and S. Miyata, "Interplay between nitrogen dopants and native point defects in graphene," *Physical Review B*, vol. 85, p. 165439, apr 2012.

[147] Y. Fujimoto and S. Saito, "Formation, stabilities, and electronic properties of nitrogen defects in graphene," *Physical Review B*, vol. 84, p. 245446, dec 2011.

[148] Y. Fujimoto and S. Saito, "Hydrogen adsorption and anomalous electronic properties of nitrogen-doped graphene," *Journal of Applied Physics*, vol. 115, p. 153701, apr 2014.

[149] H. Terrones, R. Lv, M. Terrones, and M. S. Dresselhaus, "The role of defects and doping in 2D graphene sheets and 1D nanoribbons," *Reports on Progress in Physics*, vol. 75, no. 6, p. 62501, 2012.

[150] T. Wassmann, A. P. Seitsonen, A. M. Saitta, M. Lazzeri, and F. Mauri, "Structure, Stability, Edge States, and Aromaticity of Graphene Ribbons," *Physical Review Letters*, vol. 101, p. 096402, aug 2008.

[151] M. Li, L. Zhang, Q. Xu, J. Niu, and Z. Xia, "N-doped graphene as catalysts for oxygen reduction and oxygen evolution reactions: Theoretical considerations," *Journal of Catalysis*, vol. 314, pp. 66–72, 2014.

[152] M. F. Baruch, I. James E. Pander, J. L. White, and A. B. Bocarsly, "Mechanistic insights into the reduction of co2 on tin electrodes using in situ atr-ir spectroscopy," *ACS Catalysis*, vol. 5, no. 5, pp. 3148–3156, 2015.

[153] Y. Chen and M. W. Kanan, "Tin oxide dependence of the co2 reduction efficiency on tin electrodes and enhanced activity for tin/tin oxide thin-film catalysts," *Journal of the American Chemical Society*, vol. 134, no. 4, pp. 1986–1989, 2012. PMID: 22239243.

[154] S. Lee, J. D. Ocon, Y. il Son, and J. Lee, "Alkaline co_2 electrolysis toward selective and continuous hcoo production over sno_2 nanocatalysts," *The Journal of Physical Chemistry C*, vol. 119, no. 9, pp. 4884–4890, 2015.

[155] A. Dutta, A. Kuzume, M. Rahaman, S. Vesztergom, and P. Broekmann, "Monitoring the chemical state of catalysts for CO2electroreduction: An in operando study," *ACS Catalysis*, vol. 5, pp. 7498–7502, dec 2015.

[156] C. Cui, J. Han, X. Zhu, X. Liu, H. Wang, D. Mei, and Q. Ge, "Promotional effect of surface hydroxyls on electrochemical reduction of co_2 over SnOx/sn electrode," *Journal of Catalysis*, vol. 343, pp. 257–265, nov 2016.

[157] A. Marjolin and J. A. Keith, "Thermodynamic Descriptors for Molecules the Catalyze Efficient CO 2 Electroreductions," *ACS Catalysis*, vol. 5, pp. 1123–1130, jan 2015.

[158] K. Saravanan, E. Gottlieb, and J. A. Keith, "Nitrogen-doped nanocarbon materials under electroreduction operating conditions and implications for electrocatalysis of CO2," *Carbon*, vol. 111, pp. 859–866, jan 2017.

[159] K. Saravanan and J. A. Keith, "Standard redox potentials, pKas, and hydricities of inorganic complexes under electrochemical conditions and implications for CO_2reduction," *Dalton Trans.*, vol. 45, no. 39, pp. 15336–15341, 2016.

[160] M. C. Groenenboom, K. Saravanan, Y. Zhu, J. M. Carr, A. Marjolin, G. G. Faura, E. C. Yu, R. N. Dominey, and J. A. Keith, "Structural and substituent group effects on multielectron standard reduction potentials of aromatic n-heterocycles," *The Journal of Physical Chemistry A*, vol. 120, pp. 6888–6894, sep 2016.

[161] O. Andreussi, I. Dabo, and N. Marzari, "Revised self-consistent continuum solvation in electronic-structure calculations," *The Journal of Chemical Physics*, vol. 136, p. 064102, feb 2012.

[162] C. M. Gray, K. Saravanan, G. Wang, and J. A. Keith, "Quantifying solvation energies at solid/liquid interfaces using continuum solvation methods," *Molecular Simulation*, vol. 43, no. 5-6, pp. 420–427, 2017.

[163] J. Rossmeisl, E. Skúlason, M. E. Bjorketun, V. Tripkovic, and J. K. Nørskov, "Modeling the electrified solid–liquid interface," *Chemical Physics Letters*, vol. 466, pp. 68–71, nov 2008.

[164] M. Raju, S.-Y. Kim, A. C. T. van Duin, and K. A. Fichthorn, "ReaxFF reactive force field study of the dissociation of water on titania surfaces," *The Journal of Physical Chemistry C*, vol. 117, pp. 10558–10572, may 2013.

[165] K. Mathew, R. Sundararaman, K. Letchworth-Weaver, T. A. Arias, and R. G. Hennig, "Implicit solvation model for density-functional study of nanocrystal surfaces and reaction pathways," *The Journal of Chemical Physics*, vol. 140, p. 084106, feb 2014.

[166] R. Christensen, H. A. Hansen, and T. Vegge, "Identifying systematic DFT errors in catalytic reactions," *Catalysis Science and Technology*, vol. 5, no. 11, pp. 4946–4949, 2015.

[167] F. Legrain and S. Manzhos, "Understanding the difference in cohesive energies between alpha and beta tin in dft calculations," *AIP Advances*, vol. 6, no. 4, p. 045116, 2016.

[168] C. Kittel, *Introduction to Solid State Physics*. Wiley, 8th ed., 2005.

[169] J. Ihm and M. L. Cohen, "Equilibrium properties and the phase transition of grey and white tin," *Physical Review B*, vol. 23, pp. 1576–1579, feb 1981.

[170] N. G. Hörmann, A. Gross, and P. Kaghazchi, "Semiconductor–metal transition induced by nanoscale stabilization," *Physical Chemistry Chemical Physics*, vol. 17, no. 8, pp. 5569–5573, 2015.

[171] C. Kittel, *CRC Handbook of Chemistry and Physics*. CRC Press, 90th ed., 2009.

[172] R. Wyckoff, *Crystal structures*, vol. 1. John Wiley Interscience Publishers, second ed., 1961.

[173] M. Batzill and U. Diebold, "The surface and materials science of tin oxide," *Progress in Surface Science*, vol. 79, no. 24, pp. 47 – 154, 2005.

[174] J. Oviedo and M. Gillan, "The energetics and structure of oxygen vacancies on the SnO2(110) surface," *Surface Science*, vol. 467, pp. 35–48, nov 2000.

[175] J. VandeVondele, M. Krack, F. Mohamed, M. Parrinello, T. Chassaing, and J. Hutter, "Quickstep: Fast and accurate density functional calculations using a mixed gaussian and plane waves approach," *Computer Physics Communications*, vol. 167, no. 2, pp. 103–128, 2005.

[176] J. VandeVondele and J. Hutter, "Gaussian basis sets for accurate calculations on molecular systems in gas and condensed phases," *The Journal of Chemical Physics*, vol. 127, no. 11, p. 114105, 2007.

[177] G. Lippert, J. Hutter, and M. Parrinello, "The gaussian and augmented-plane-wave density functional method for ab initio molecular dynamics simulations," *Theoretical Chemistry Accounts*, vol. 103, no. 2, pp. 124–140, 1999.

[178] S. Goedecker, M. Teter, and J. Hutter, "Separable dual-space gaussian pseudopotentials," *Physical Review B*, vol. 54, no. 3, p. 1703, 1996.

[179] J. P. Perdew, K. Burke, and M. Ernzerhof, "Generalized gradient approximation made simple," *Physical Review Letters*, vol. 77, no. 18, p. 3865, 1996.

[180] S. Grimme, J. Antony, S. Ehrlich, and H. Krieg, "A consistent and accurate ab initio parametrization of density functional dispersion correction (dft-d) for the 94 elements h-pu," *The Journal of Chemical Physics*, vol. 132, no. 15, p. 154104, 2010.

[181] G. Kresse and J. Furthmüller, "Efficient iterative schemes for ab initio total-energy calculations using a plane-wave basis set," *Physical review B*, vol. 54, no. 16, p. 11169, 1996.

[182] P. E. Blöchl, "Projector augmented-wave method," *Physical Review B*, vol. 50, no. 24, p. 17953, 1994.

[183] G. Kresse and D. Joubert, "From ultrasoft pseudopotentials to the projector augmented-wave method," *Physical Review B*, vol. 59, no. 3, p. 1758, 1999.

[184] J. Oviedo and M. Gillan, "Energetics and structure of stoichiometric SnO2 surfaces studied by first-principles calculations," *Surface Science*, vol. 463, pp. 93–101, sep 2000.

[185] M. A. Maki-Jaskari and T. T. Rantala, "Theoretical study of oxygen-deficientSnO2(110)surfaces," *Physical Review B*, vol. 65, p. 245428, jun 2002.

[186] W.-J. Yin, M. Krack, B. Wen, S.-Y. Ma, and L.-M. Liu, "CO2capture and conversion on rutile TiO2(110) in the water environment: Insight by first-principles calculations," *The Journal of Physical Chemistry Letters*, vol. 6, pp. 2538–2545, jul 2015.

[187] H. A. Hansen, I. C. Man, F. Studt, F. Abild-Pedersen, T. Bligaard, and J. Rossmeisl, "Electrochemical chlorine evolution at rutile oxide (110) surfaces," *Physical Chemistry Chemical Physics*, vol. 12, no. 1, pp. 283–290, 2010.

[188] K. S. Exner, J. Anton, T. Jacob, and H. Over, "Chlorine evolution reaction on ruo 2 (110): Ab initio atomistic thermodynamics study-pourbaix diagrams," *Electrochimica Acta*, vol. 120, pp. 460–466, 2014.

[189] P. Liao, J. A. Keith, and E. A. Carter, "Water oxidation on pure and doped hematite (0001) surfaces: Prediction of co and ni as effective dopants for electrocatalysis," *Journal of the American Chemical Society*, vol. 134, pp. 13296–13309, aug 2012.

[190] A. Cherashev and A. Khrushch, "The electrochemical reduction of carbon dioxide at the tin-cadmium and tin-zinc alloys," *Russian Journal of Electrochemistry*, vol. 33, no. 2, pp. 181–185, 1997.

[191] A. Cherashev and A. Khrushch, "Electrochemical reduction of carbon dioxide on tin, zinc, and their alloys," *Russian Journal of Electrochemistry*, vol. 34, no. 5, pp. 410–417, 1998.

[192] S. Y. Choi, S. K. Jeong, H. J. Kim, I.-H. Baek, and K. T. Park, "Electrochemical reduction of carbon dioxide to formate on tin–lead alloys," *ACS Sustainable Chemistry & Engineering*, vol. 4, pp. 1311–1318, mar 2016.

[193] Z. W. Seh, J. Kibsgaard, C. F. Dickens, I. Chorkendorff, J. K. Nørskov, and T. F. Jaramillo, "Combining theory and experiment in electrocatalysis: Insights into materials design," *Science*, vol. 355, jan 2017.

[194] J. Greeley, I. E. L. Stephens, A. S. Bondarenko, T. P. Johansson, H. A. Hansen, T. F. Jaramillo, J. Rossmeisl, I. Chorkendorff, and J. K. Nørskov, "Alloys of platinum and early transition metals as oxygen reduction electrocatalysts," *Nat. Chem.*, vol. 1, pp. 552–556, sep 2009.

[195] V. Stamenkovic, B. S. Mun, K. J. Mayrhofer, P. N. Ross, N. M. Markovic, J. Rossmeisl, J. Greeley, and J. K. Nørskov, "Changing the activity of electrocatalysts for oxygen reduction by tuning the surface electronic structure," *Angew. Chem., Int. Ed.*, vol. 118, pp. 2963–2967, apr 2006.

[196] M. Muñoz and C. Cárdenas, "How predictive could alchemical derivatives be?," *Phys. Chem. Chem. Phys.*, vol. 19, no. 24, pp. 16003–16012, 2017.

[197] K. Y. S. Chang, S. Fias, R. Ramakrishnan, and O. A. von Lilienfeld, "Fast and accurate predictions of covalent bonds in chemical space," *J. Chem. Phys.*, vol. 144, p. 174110, may 2016.

[198] Y. S. Al-Hamdani, D. Alfè, O. A. von Lilienfeld, and A. Michaelides, "Tuning dissociation using isoelectronically doped graphene and hexagonal boron nitride: Water and other small molecules," *J. Chem. Phys.*, vol. 144, p. 154706, apr 2016.

[199] J. K. Nørskov, J. Rossmeisl, A. Logadottir, L. Lindqvist, J. R. Kitchin, T. Bligaard, and H. Jónsson, "Origin of the overpotential for oxygen reduction at a fuel-cell cathode," *J. Phys. Chem. B*, vol. 108, pp. 17886–17892, nov 2004.

[200] J. Greeley, T. F. Jaramillo, J. Bonde, I. Chorkendorff, and J. K. Nørskov, "Computational high-throughput screening of electrocatalytic materials for hydrogen evolution," *Nat. Mater.*, vol. 5, pp. 909–913, oct 2006.

[201] O. A. von Lilienfeld, "First principles view on chemical compound space: Gaining rigorous atomistic control of molecular properties," *Int. J. Quantum Chem.*, vol. 113, pp. 1676–1689, feb 2013.

[202] R. P. Feynman, "Forces in molecules," *Phys. Rev.*, vol. 56, pp. 340–343, Aug 1939.

[203] F. Abild-Pedersen, J. Greeley, F. Studt, J. Rossmeisl, T. R. Munter, P. G. Moses, E. Skúlason, T. Bligaard, and J. K. Nørskov, "Scaling properties of adsorption energies for hydrogen-containing molecules on transition-metal surfaces," *Phys. Rev. Lett.*, vol. 99, p. 016105, jul 2007.

[204] S. Bhattacharjee, U. V. Waghmare, and S.-C. Lee, "An improved d-band model of the catalytic activity of magnetic transition metal surfaces," *Sci. Rep.*, vol. 6, p. 35916, nov 2016.

[205] M. Rupp, R. Ramakrishnan, and O. A. von Lilienfeld, "Machine learning for quantum mechanical properties of atoms in molecules," *The Journal of Physical Chemistry Letters*, vol. 6, no. 16, pp. 3309–3313, 2015.

[206] G. Montavon, M. Rupp, V. Gobre, A. Vazquez-Mayagoitia, K. Hansen, A. Tkatchenko, K.-R. Müller, and O. A. Von Lilienfeld, "Machine learning of molecular electronic properties in chemical compound space," *New Journal of Physics*, vol. 15, no. 9, p. 095003, 2013.

[207] F. A. Faber, A. Lindmaa, O. A. Von Lilienfeld, and R. Armiento, "Machine learning energies of 2 million elpasolite (a b c 2 d 6) crystals," *Physical review letters*, vol. 117, no. 13, p. 135502, 2016.

[208] S. Hashemifar, B. Neyshabur, A. A. Khan, and J. Xu, "Predicting protein–protein interactions through sequence-based deep learning," *Bioinformatics*, vol. 34, no. 17, pp. i802–i810, 2018.

[209] O. A. von Lilienfeld, "Quantum machine learning in chemical compound space," *Angewandte Chemie International Edition*, vol. 57, no. 16, pp. 4164–4169, 2018.

[210] G. Yang, J. Wu, S. Chen, W. Zhou, J. Sun, and G. Chen, "Size-independent neural networks based first-principles method for accurate prediction of heat of formation of fuels," *The Journal of Chemical Physics*, vol. 148, no. 24, p. 241738, 2018.

[211] C. R. Collins, G. J. Gordon, O. A. von Lilienfeld, and D. J. Yaron, "Constant size descriptors for accurate machine learning models of molecular properties," *The Journal of Chemical Physics*, vol. 148, no. 24, p. 241718, 2018.

[212] B. Meredig, A. Agrawal, S. Kirklin, J. E. Saal, J. Doak, A. Thompson, K. Zhang, A. Choudhary, and C. Wolverton, "Combinatorial screening for new materials in unconstrained composition space with machine learning," *Physical Review B*, vol. 89, no. 9, p. 094104, 2014.

[213] Z. Li, S. Wang, W. S. Chin, L. E. Achenie, and H. Xin, "High-throughput screening of bimetallic catalysts enabled by machine learning," *Journal of Materials Chemistry A*, vol. 5, no. 46, pp. 24131–24138, 2017.

[214] Z. Li, X. Ma, and H. Xin, "Feature engineering of machine-learning chemisorption models for catalyst design," *Catalysis today*, vol. 280, pp. 232–238, 2017.

[215] K. Tran and Z. W. Ulissi, "Active learning across intermetallics to guide discovery of electrocatalysts for co_2 reduction and h_2 evolution," *Nature Catalysis*, vol. 1, no. 9, p. 696, 2018.